Print ISSN 3079-8493
Online ISSN 3079-8507

National Oil Corporation
Petroleum Research Center

PETROLEUM RESEARCH JOURNAL

34 عاما من العطاء العلمي والتميز البحثي في قطاع النفط والطاقة

34 Years of academic excellence and research distinction in the oil and energy sector



Volume.26 (2026)

Petroleum Research Journal
P.O. Box 6431, Tripoli
Libya

journal.prclibya.com
journal@prclibya.com

PETROLEUM RESEARCH JOURNAL

Tripoli, Libya

National Oil Corporation
Petroleum Research Center

Acting Chairman

Khaled Khalifa

Khaled Khalifa

Editor-in-Chief

Bin Nayil Alsanousi

Bin Nayil Alsanousi

Deputy Editor-in-Chief

Fawzi Elfghi

Fawzi Elfghi

Table of Content

Title	Page
Comparison of Seismic Attribute Techniques for Fault Detection with Machine Learning Workflows: a case study from The Sirte Basin, Libya ……	7
Geological, Geomorphological and Structural Mapping Updates of Jabal Al Uwaynat in Southeastern Libya, Usening Remote Sensing Techniques ……	16
Impact of Confining Pressure on Reservoir Permeability …….	26
Corrosion Rate Prediction for Underground Gas Pipelines Using Artificial Neural Network (ANN) ……..	37
Desulfurization of Libyan Fuel Oil by Solvent Extraction ……..	47
Comparative Radiological Assessment of a Former Thorium Mine and Oilfield Produced Water Lakes …….	57
AI-Driven Cybersecurity Framework for Energy Research Infrastructure and Geoscience Data Systems …….	73
Integrating AI and Metaverse Technologies for Big Data Optimization in Renewable Energy ……..	83

COPYRIGHT AND PUBLICATION INFORMATION

Copyright © 2026/2027 by the Petroleum Research Center Journal (PRC)
Petroleum Research Center, Tripoli, Libya

All rights reserved.

The *Petroleum Research Center Journal* is published by the Petroleum Research Center (PRC), Tripoli, Libya, as a peer-reviewed scientific publication dedicated to advancing research and disseminating knowledge in petroleum, energy, and related scientific and engineering disciplines.

The Management Committee and Editorial Team extend their **sincere appreciation and profound thanks** to all authors, reviewers, editorial members, researchers, and contributors whose dedication, expertise, and valuable efforts support the continued development and advancement of the Journal.

No part of this publication may be reproduced, distributed, transmitted, or stored in any form or by any means, whether electronic or mechanical, including photocopying, recording, or any information storage and retrieval system, without prior written permission from the copyright holders, except where permitted by applicable copyright law.

Published with appreciation for the continued support of the scientific and research community.

Petroleum Research Center (PRC)
Tripoli – Libya

Message from the acting-chairman

FOREWORD

On behalf of the Editorial Board and Management Committee, I warmly welcome all authors, researchers, academics, and industry professionals to contribute to the Petroleum Research Center Journal. We encourage you to share your valuable research, knowledge, and experience with our scientific community. Your contributions will help strengthen scientific dialogue, support innovation, and advance research addressing current and future challenges in the energy sector. We look forward to welcoming your valuable contributions to the Journal.

The Petroleum Research Center Journal is a peer-reviewed scientific journal dedicated to publishing original and innovative research in petroleum, energy, and related scientific and engineering disciplines, with relevance to Libya's oil, gas and energy sector. The Journal covers a broad range of fields, including petroleum and chemical engineering, materials and corrosion engineering, geology, geochemistry, geophysics, environmental studies, and renewable energy as well as AI disciplines. The Journal seeks to promote scientific knowledge, research innovation, collaboration, and the exchange of expertise at the local, regional, and international levels.

Acting Chairman of the Management Committee

Mr. Khaled Khalifa

Khaled Khalifa

Message of the Editorial-Board

As the ***Petroleum research Centre Journal*** *is committed to promoting scientific excellence, advancing knowledge, and encouraging meaningful collaboration among the local, regional, and international research communities, the Editorial Board are pleased to welcome researchers, academics, engineers, and industry professionals to fostering a professional and constructive environment for the exchange of scientific knowledge, research findings, and practical experience.*

The Editorial-Board *members encourage authors to submit original and impactful contributions that advance understanding, address emerging challenges, and support innovation in oil, gas, energy, and related fields. Also, we greatly value the contribution of researchers from Libya and around the world and welcome diverse perspectives and multidisciplinary research. The Editorial Board look forward to working with our authors and reviewers to ensure a rigorous, fair, and transparent publication process and to further strengthen the Journal as a platform for meaningful scientific communication.*

Editorial-Board members

Comparison of Seismic Attribute Techniques for Fault Detection with Machine Learning Workflows: a case study from The Sirte Basin, Libya

Abdurahmaan Khalid Ajaj

Petroleum Research Center
ORCID No. (Author): 0009-0005-8763-7470
Email : a.ajaj@prclibya.com

Abstract

Accurate fault interpretation is a fundamental component of seismic structural analysis and is essential for reservoir characterization, structural mapping, and hydrocarbon exploration. This study presents a comparative analysis of conventional seismic attribute-based fault detection and modern machine learning (ML)-assisted interpretation using 3D seismic data from the Sirte Basin, Libya. The study area is characterized by complex structural deformation and predominantly NW–SE-oriented extensional faulting. The conventional workflow applies seismic conditioning, structural smoothing, variance attributes, and Ant Tracking to enhance and automatically extract fault-related discontinuities. In contrast, the ML workflow utilizes deep-learning techniques to identify fault patterns directly from seismic data. The comparison focuses on fault continuity, spatial resolution, noise suppression, detection of subtle faults, and interpretation efficiency. The results demonstrate that conventional attributes provide effective and interpretable fault-enhancement products, while ML-assisted methods can improve fault continuity and reduce noise, particularly for complex and subtle structures. The study highlights the potential of integrating conventional seismic attributes with machine learning to enhance fault interpretation and improve structural understanding of the Sirte Basin.

Keywords: Seismic Attributes, Machine Learning, Fault Detection, Ant Tracking, Structural Interpretation

مقارنة بين تقنيات السمات الزلزالية للكشف عن الصدوع وسير عمل التعلم الآلي: دراسة حالة من حوض سرت، ليبيا

عبدالرحمن خالد عجاج
مركز البحوث النفط ، طرابلس-ليبيا

ملخص

يُعدّ التفسير الدقيق للفوالق أحد العناصر الأساسية للتحليل البنيوي للبيانات الزلزالية، كما يُعتبر مهمًا لتوصيف المكامن، ورسم التراكيب البنيوية، واستكشاف الهيدروكربونات. تقدم هذه الدراسة مقارنة بين أساليب الكشف التقليدية عن الفوالق باستخدام الخصائص الزلزالية وأساليب التفسير الحديثة المعتمدة على التعلم الآلي (ML)، وذلك باستخدام بيانات زلزالية ثلاثية الأبعاد من حوض سرت في ليبيا. تتميز المنطقة بتعقيد بنيوي واضح ووجود فوالق تمددية يغلب عليها الاتجاه شمال غرب–جنوب شرق. يعتمد مسار العمل التقليدي على تهيئة البيانات الزلزالية، والتنعيم البنيوي، وحساب خاصية التباين (Variance)، ثم استخدام تقنية التتبع بالنمل (Ant Tracking) لتعزيز واستخراج الانقطاعات المرتبطة بالفوالق بصورة آلية. في المقابل، يعتمد مسار التعلم الآلي على تقنيات التعلم العميق للتعرف على أنماط الفوالق مباشرةً من البيانات الزلزالية. تركز المقارنة على استمرارية الفوالق، والدقة المكانية، وتقليل الضوضاء، والقدرة على تحديد الفوالق الدقيقة، وكفاءة التفسير. وتوضح النتائج أن الخصائص الزلزالية التقليدية توفر منتجات فعالة وقابلة للتفسير لتعزيز الفوالق، بينما يمكن لأساليب التعلم الآلي تحسين استمرارية الفوالق وتقليل الضوضاء، خاصةً في التراكيب المعقدة والدقيقة. وتبرز الدراسة إمكانية دمج الخصائص الزلزالية التقليدية مع التعلم الآلي لتحسين تفسير الفوالق وتعزيز فهم البنية الجيولوجية لحوض سرت.

الكلمات المفتاحية: خصائص البيانات الزلزالية، التعلم الآلي، الكشف عن الفوالق، خوارزمية تتبع النمل، التفسير البنائي

1. Introduction

Fault interpretation is a key element of seismic structural analysis, with important implications for reservoir characterization, exploration, and development (Chopra & Marfurt, 2007). Faults are zones of discontinuity that can influence reservoir compartmentalization, fluid flow, and well placement. However, their reliable interpretation from seismic data can be difficult because of noise, subtle fault expressions, and complex geometries. Seismic attributes such as variance can highlight discontinuities, while Ant Tracking can help extract fault-like features from attribute volumes (Chopra & Marfurt, 2007; Abdelnabi et al., 2017). Recent deep-learning approaches, including convolutional neural networks, provide another way to identify fault patterns in 3D seismic data (Wu & Famelis, 2019).

1.1 Main Objective

- To compare Machine Learning (ML) workflows with traditional seismic attribute methods, particularly Ant Tracking, for detecting and mapping complex fault networks in the Sirte Basin, Libya.
- To evaluate both workflows in terms of fault detection accuracy, continuity, efficiency, and processing time to identify the most effective approach for seismic fault interpretation.

1.2 Geology of the Sirte Basin

The Sirte Basin is one of the major hydrocarbon provinces in North Africa and is a complex rift system in north-central Libya as shown in Figure 1. Its tectonic evolution includes Late Cretaceous rifting, which formed a network of platforms and troughs. The basin is dominated by NW–SE-oriented normal faults, which influence hydrocarbon migration and trapping. These regional structural characteristics make reliable fault mapping important for exploration and reservoir interpretation (Abadi et al., 2020).

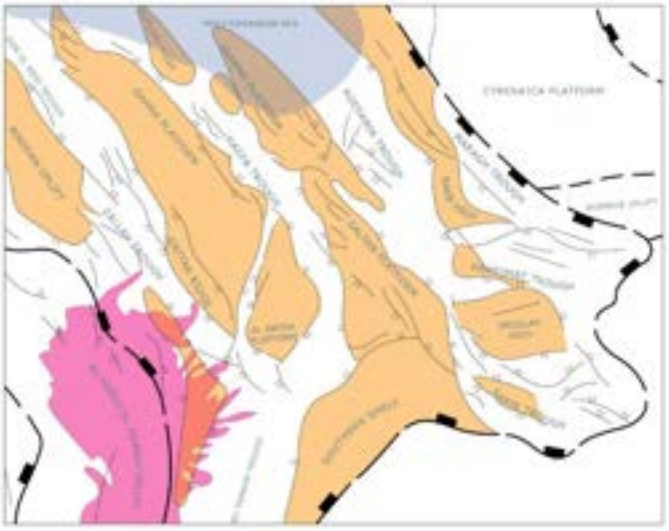


Figure 1: Tectonic elements of The Sirte rift basin & large numbers of significant oil fields

1.3 Challenges in Seismic Fault Interpretation

Traditional manual interpretation can be subjective and time-consuming, while noise and complex fault geometries may obscure discontinuities in seismic amplitude data (Chopra & Marfurt, 2007; Abdelnabi et al., 2017). Key challenges include:

- Seismic Noise: Acquisition and processing artifacts often mask subtle discontinuities.
- Complex Geometries are difficult to resolve using standard amplitude volumes.

- Data Volume: Modern 3D seismic volumes are too large for exhaustive manual interpretation, necessitating high-fidelity automated solutions.

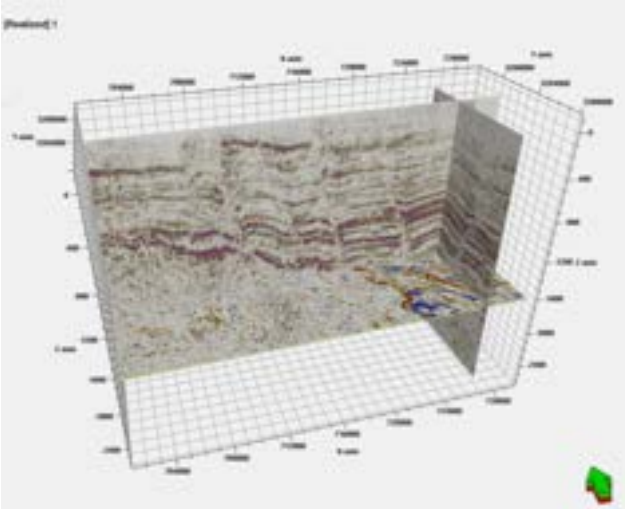


Figure 2 PSTM seismic amplitude volume used in this study.

The amplitude data provides the seismic reflection framework from which structural discontinuities are interpreted; however, faults may not always be clearly visible where signal-to-noise quality is poor. Figure 2 shows the PSTM seismic amplitude volume used in this study.

Machine-learning (ML) techniques have created new opportunities for automating fault detection. Deep-learning models can learn patterns from seismic examples and identify fault-like features that may be difficult to capture with conventional attributes alone (Wu & Famelis, 2019). This paper compares two workflows in the Sirte Basin: a conventional attribute-based workflow using structural smoothing, first derivative and variance attributes followed by Ant Tracking, and a machine-learning workflow that detects fault patterns from seismic data (see Figure 3).

1. The conventional workflow uses structural smoothing, first-derivative and variance (edge-detection) attributes, followed by Ant Tracking for automatic fault extraction. Seismic attributes are commonly used to enhance discontinuities and support fault interpretation (Chopra & Marfurt, 2007; Abdelnabi et al., 2017).

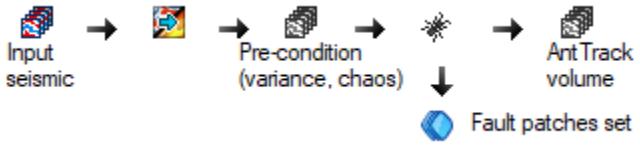


Figure 3: An Ant Tracking for automatic fault extraction workflow.

2. The machine-learning workflow uses a deep-learning model to identify fault patterns from the seismic amplitude volume, as illustrated in Figure 4. CNN-based seismic fault segmentation has been demonstrated in published research (Wu & Famelis, 2019).



Figure 4: A machine learning-based workflow

2. Dataset and Methodology

2.1 Dataset of This Study

The dataset is a standard Pre-Stack Time Migration (PSTM) seismic amplitude volume. For quality control, 64 key faults were manually interpreted and used as a reference set to compare the outputs of the ML and Ant Tracking workflows (Figure 5).

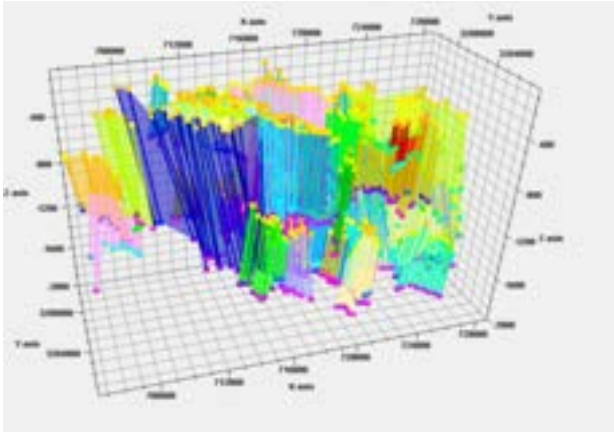


Figure 5: The Manual picked used as a reference to test & QC how well machine learning methods can detect faults.

2.2. Workflow and Methodology

2.2.1 Data Preparation

This study uses 3D seismic volumes from a regional exploration project in the Sirte Basin, Libya. Variable signal-to-noise ratio is a key challenge because it can obscure fault signatures. Two strategies were evaluated: an ML workflow applied to the seismic amplitude data without user-applied filtering or attribute enhancement, and a conventional workflow that uses derived seismic attributes to highlight structural discontinuities. These approaches reflect two different ways of extracting fault-related information from seismic data (Chopra & Marfurt, 2007; Wu & Famelis, 2019).

The fundamental difference between these the methods lies in their approach to data "filtering." The Ant Tracking workflow depends heavily on the interpreter's ability to manually clean and condition the data. While this allows for human oversight, it introduces subjectivity and often leaves gaps in areas where data quality is poor. In contrast, the Machine Learning workflow manages noise and signal enhancement internally through its neural layers. This allows the system to effectively see Figure 6, the seismic artifacts that typically confuse traditional algorithms. Ultimately, by transitioning from a parameter-heavy manual process to a probabilistic AI-driven extraction, the ML approach produces a more efficient and geologically consistent map of the basin's complex fault networks.

2.2.2 Seismic Attribute and Ant Tracking Workflow

The conventional workflow (Figure 6) begins with structural smoothing to reduce random noise while preserving discontinuities. Variance and first-derivative attributes are then calculated to emphasize changes in the seismic signal. The attributes are supplied to Ant Tracking, which enhances connected discontinuities; the resulting volume is thresholded and individual fault surfaces are extracted. Attribute-assisted fault interpretation and Ant Tracking are established approaches for enhancing fault-related features in seismic data (Chopra & Marfurt, 2007; Abdelnabi et al., 2017).

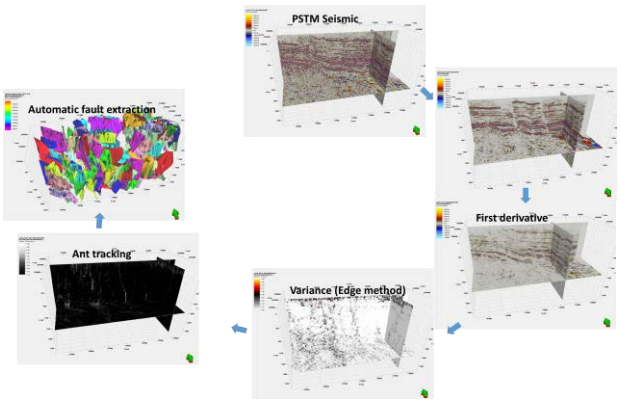


Figure 6: Seismic Attribute and Ant Tracking Workflow

2.2.3 The Machine Learning-Based Workflow

The ML workflow (Figure 7) processes the seismic amplitude volume with a deep-learning model, rather than relying on user-defined seismic attributes as the primary fault indicators. The model generates a fault-probability volume; thresholding and pointset extraction are then used to identify high-probability fault locations and group them into surfaces. CNN-based segmentation of 3D seismic faults has been described by Wu and Famelis (2019). The results in this study are evaluated against the 64 manually interpreted reference faults.

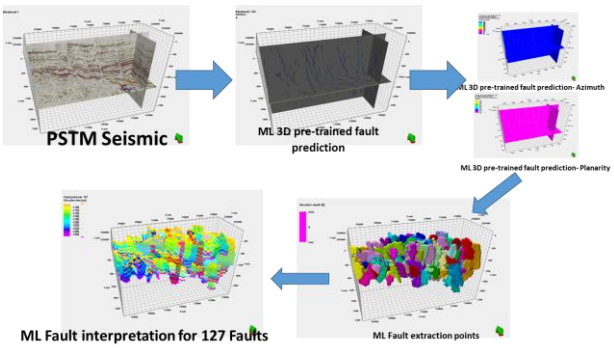


Figure 7: The Machine Learning-Based Workflow

3. Result and Discussion

3.1 Comparison of AI Faults vs. Ant Tracking

The results indicate differences between the two automated workflows. Based on visual comparison with the 64 manually interpreted reference faults, the ML output shows more coherent vertical continuity of the NW–SE fault systems in this dataset. This is a qualitative comparison and should not be interpreted as a quantitative accuracy score because no numerical precision/recall metrics are reported.

In areas with weak or noisy seismic reflections, the Ant Tracking result contains more fragmented or disconnected features. The ML result appears to preserve more connected fault-like surfaces across some of these areas. This observation is consistent with the potential of learned seismic patterns for fault segmentation, although performance remains dependent on the training data and model generalization (Wu & Famelis, 2019).

3.2 Efficiency in Automatic Extraction

From a practical standpoint, the conventional Ant Tracking workflow requires selection and adjustment of attribute and extraction parameters, and the interpreter may need to review and clean the resulting surfaces. This can make the workflow iterative, particularly where noise or complex fault intersections affect the output (Chopra & Marfurt, 2007; Abdelnabi et al., 2017).

The ML workflow can reduce some manual attribute-conditioning and extraction steps, but it still requires appropriate model

training, threshold selection, quality control, and geological review. In this study, the output is visually compared with the reference faults and the Ant Tracking result; processing-time measurements would be needed to quantify any efficiency advantage. As shown in Figure 8, the mixer cube overlays the ML-derived fault interpretation on the raw seismic amplitude data. This view allows the interpreted fault surfaces to be checked against the underlying reflection patterns and helps assess whether the predicted faults follow plausible seismic discontinuities.

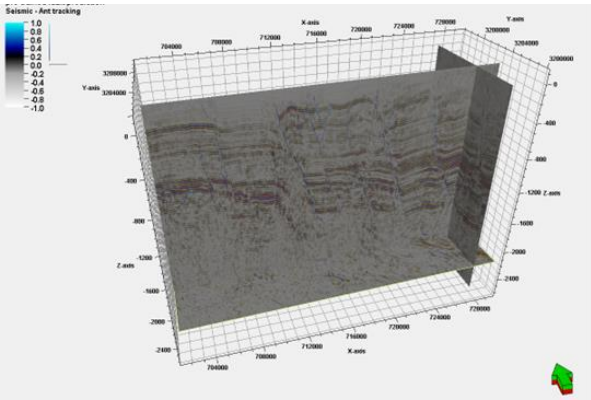


Figure 8: Mixer cube combining the raw seismic amplitude volume and the ML-derived fault cube.

Figure 9 presents the same type of overlay for the Ant Tracking output. Comparing Figures 8 and 9 provides a visual basis for assessing differences in fault continuity, fragmentation, and alignment with the seismic reflections. In this dataset, the ML interpretation appears more connected in some areas, whereas the Ant Tracking result contains more discontinuous features; this is a qualitative visual observation rather than a measured accuracy statistic.

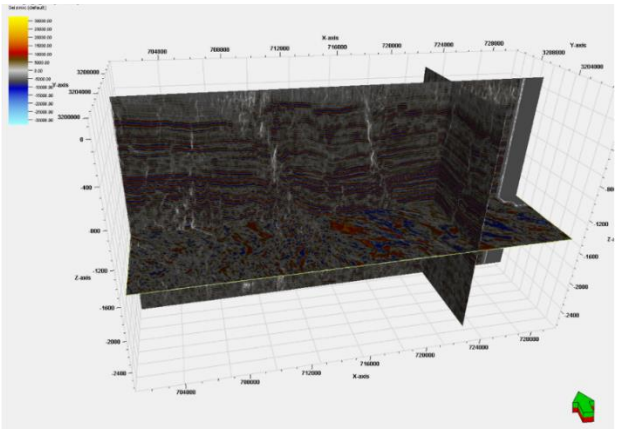


Figure 9: Mixer cube combining the raw seismic amplitude volume and the Ant Tracking fault cube.

3.3 Comparison Criteria

The performance of both workflows was compared using the following criteria:

- **Accuracy**: Evaluated by visual comparison of fault planes with known geological structures and fault markers.
- **Continuity**: Measured by the continuity and length of extracted fault planes, as well as the ability to capture subtle fault traces.
- **Efficiency**: Measured by the processing time required to generate the fault surfaces and the amount of manual intervention needed in each workflow.
- **Time**: The total time taken for each workflow, from data input to final fault surface extraction.

4. Conclusion

This study demonstrates that the evolution of seismic interpretation has reached a pivotal turning point. While traditional seismic

attributes and Ant Tracking have served the industry well—and remain reliable tools for high-quality, "clean" data—they often struggle to meet the demands of geologically complex environments. In a setting as structurally intricate as the **Sirte Basin**, these traditional methods frequently fall short, requiring excessive manual intervention to produce a usable map.

The introduction of Machine Learning **(ML)** represents more than just a new software update; it is a fundamental leap in both efficiency and accuracy. The true power of the ML approach lies in its ability to bridge the gap between human intuition and computational speed. By "learning" from the experience of human interpreters, the model can look at messy or noisy data and see the underlying geological truth that simpler algorithms miss. It doesn't just track lines; it understands the three-dimensional continuity of fault planes.

Ultimately, the ML workflow proves to be the superior choice for modern structural analysis. It handles the "heavy lifting" of data processing at an incredible scale, delivering results that are both highly precise and geologically sound. By reducing the time spent on manual cleanup and repetitive parameter testing, this technology allows geoscientists to focus on the more critical tasks of reservoir characterization and risk assessment, ensuring a more accurate understanding of the subsurface.

5. Recommendation

- Large-Scale Applications: Machine learning should be prioritized for large seismic datasets, where efficiency and automation provide significant advantages in reducing processing time and manual intervention.
- Future Research: Future studies should explore the use of deep learning models, which have shown promise in other domains of seismic interpretation. Additionally, models could be trained on more diverse datasets to enhance the generalization of fault detection in different geological settings.

References

Abadi, M., et al. (2020). Tectonic Evolution and Complex Faulting of the Sirte Basin: Implications for Hydrocarbon Systems. Journal of African Earth Sciences.

Abdelnabi, A., et al. (2017). Seismic Attribute-Aided Fault Detection and Enhancement in the Sirte Basin, Libya. Interpretation, SEG/AAPG.

Alzaruk, A., et al. (2024). Application of Machine Learning for Accelerating the Fault Interpretation in the Structurally Complex Area: A Case Study of the Sirte Basin, Libya. MEOS GEO Technical Programme, SPE-227700.

Chopra, S., & Marfurt, K. J. (2007). Seismic Attributes for Fault/Fracture Characterization. SEG Technical Program Expanded Abstracts.

Wu, X., & Famelis, G. (2019). FaultSeg3D: Using Synthetic Datasets to Train Convolutional Neural Networks for 3D Seismic Fault Segmentation. Geophysics, 84(6), IM13–IM26.

Geological, Geomorphological and Structural Mapping Updates of Jabal Al Uwaynat in Southeastern Libya, Usening Remote Sensing Techniques.

[1*]*Eddawi A. Elhatmi*

[1*]*Petroleum Research Center, Tripoli-Libya, e.elhatmi@prclibya.com*
ORCID No: 0009-0003-7992-300X

Abstract

Ten-color composite images were generated through the integration of three Landsat Enhanced Thematic Mapper (ETM) bands following dynamic image enhancement using the Histogram Equalization Contrast Stretching technique. These enhanced composites proved highly effective in facilitating the interpretation of terrain features within the Jabal Al Uwaynat region. The processed images provided additional geological and geomorphological information beyond that obtainable from the original Landsat ETM (7,4,2) dataset.

A comparison between the ten-color composite images and existing geological maps of the area, including those produced by IRC (2007) at a scale of 1:250,000 and Hunting (1974) at a scale of 1:100,000, revealed a strong correspondence between the spectral variations observed in the imagery and the mapped geological and geomorphological features. In particular, the distribution of Quaternary landforms and ring-complex structures within Jabal Al Uwaynat closely matched the patterns identified on the enhanced Landsat ETM (7,4,2) images.

The observed spectral and spatial variations are primarily associated with geomorphological characteristics such as differences in surface texture and patterns, spectral reflectance properties, lithological composition, moisture content, grain size, sediment thickness, and porosity of Quaternary deposits. Based on the interpretation of these enhanced images, updated geomorphological and geological maps were developed, leading to the identification of several previously unrecognized features that had not been represented in earlier mapping efforts.

To further investigate the terrain characteristics of the study area, a band ratioing technique was applied using the reflective bands of the Landsat ETM imagery. A total of twelve band-ratio images were generated, each emphasizing specific terrain and geological attributes. Moreover, single-color composite images derived from combinations of three band ratios successfully highlighted subtle variations among different terrain units, thereby improving feature discrimination and interpretation.

The study relied primarily on visual image analysis, and the results demonstrated that band ratioing is an effective remote sensing technique for identifying and differentiating terrain features within the Jabal Al Uwaynat region. The integration of enhanced color composites and band-ratio analyses significantly contributed to improving the accuracy of geomorphological and geological mapping and provided valuable insights into the region's surface characteristics.

Keywords: Landsat Enhanced Thematic Mapper Imagery, Jabal Al Uwaynat, Remote Sensing Techniques, Band rationing technique

تحديث الخريطة الجيولوجية والجيومورفولوجية والتركيبية لمنطقة جبل العوينات في جنوب شرق ليبيا باستخدام تقنيات الاستشعار عن بُعد

المؤلف: أ. الضاوي علي الحاتمي- أخصائي أول
مركز بحوث النفط ، طرابلس - ليبيا

الملخص

تم إنتاج صور مركبة ذات عشرة ألوان من خلال دمج ثلاث قنوات من بيانات القمر الصناعي لاندسات (ETM+) بعد تطبيق تقنيات التحسين الديناميكي للصور، والتي شملت معادلة المدرج التكراري (Histogram Equalization) وتمديد التباين (Contrast Stretching).وقد أسهمت هذه الصور المحسنة في تحسين تفسير المعالم التضاريسية لمنطقة جبل العوينات، وكشفت عن معلومات جيولوجية وجيومورفولوجية لم تكن واضحة في الصور الأصلية للقمر الصناعي لاندسات (القنوات 7 و4 و2).

تمت مقارنة المعلومات المستخلصة بالخرائط الجيولوجية المتوفرة للمنطقة، بما في ذلك خريطة IRC (2007) بمقياس رسم 1:250,000 وخريطة Hunting (1974) بمقياس رسم 1:100,000. وأظهرت نتائج التحليل أن العديد من الأشكال الأرضية الرباعية (Quaternary Landforms) ومعالم المجمعات الحلقية (Ring Complexes) تتوافق بشكل وثيق مع التباينات الطيفية التي أظهرتها صور لاندسات المعالجة.

وتُعزى هذه التباينات الطيفية إلى الاختلافات في الخصائص الجيومورفولوجية، وأنماط السطح، وأنواع الصخور، ومحتوى الرطوبة، وحجم الحبيبات، وسمك الرواسب الرباعية ومساميتها. واستناداً إلى تفسير الصور المحسنة، تم إعداد خرائط جيولوجية وجيومورفولوجية محدثة، أسفرت عن الكشف عن عدد من المعالم التي لم تُسجل في الخرائط السابقة.

كما تم تطبيق تقنية نسب الحزم الطيفية (Band Ratioing) بهدف تحسين عملية التعرف على المعالم التضاريسية في منطقة جبل العوينات. وتم إنشاء اثنتي عشرة صورة ناتجة عن نسب مختلفة بين الحزم الطيفية لبيانات الانعكاس الطيفي (Reflectance) الخاصة بصور لاندسات .ETM+ وقد أظهرت كل نسبة طيفية خصائص جيولوجية وجيومورفولوجية محددة، في حين نجحت التراكيب اللونية المختلفة لهذه النسب في إبراز الفروق الدقيقة بين المعالم المختلفة للمنطقة.

اعتمدت الدراسة بصورة رئيسية على التفسير البصري للصور الفضائية، وأثبتت النتائج فعالية تقنية نسب الحزم الطيفية في التعرف على المعالم السطحية وتحسين دقة الخرائط الجيولوجية والجيومورفولوجية في البيئات الصحراوية الجافة، مثل منطقة جبل العوينات في جنوب شرق ليبيا.

الكلمات المفتاحية:
صور لاندسات+ETM ، جبل العوينات، الاستشعار عن بُعد، الخرائط الجيولوجية، الخرائط الجيومورفولوجية، الخرائط التركيبية، تقنية نسب الحزم الطيفية، جنوب شرق ليبيا.

1.Introduction

The Jabal AL Uwaynat area occupies 710.62 square kilometers and is situated between latitudes 21° 45`N and 22° 00`N and longitudes 24° 45`E and 25° 00`E (Figs. 1 and 2). The eastern parts of the area border on the Arab Republic of Egypt and the Democratic Republic of the Sudan. The main road from kufrah Oasis to southwest Egypt and northwest Sudan passes diagonally southeast across the area through the police station at Ain Dua, adjacent to Jabal AL Uwaynat area, which is the only permanently occupied place in Jabal AL Uwaynat area. The distance from Ain Dua to Kufrah Oasis is about 325 km. Jabal AL Uwaynat is roughly circular with a diameter of about 22.5 km; it rises to about 1000 m. above the plain. The massif is composed of outcrops of alkaline rocks which are deeply weathered and form very large well - rounded blocks. (El– Mehdi *et al*, 2004).

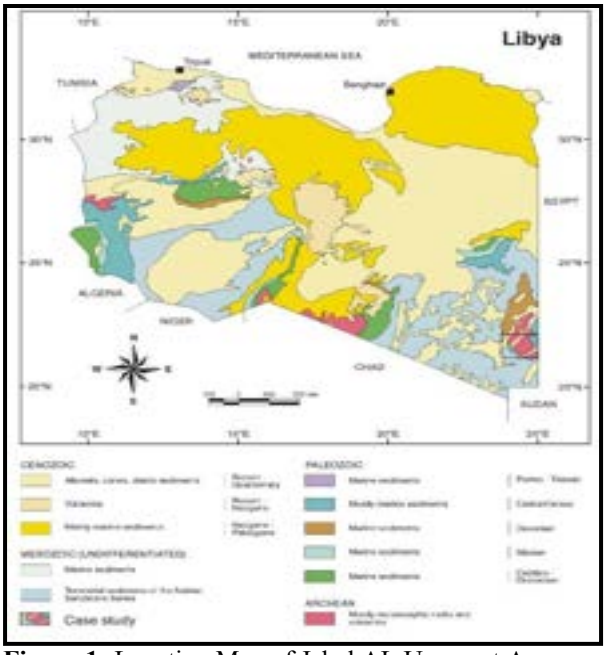


Figure 1: Location Map of Jabal AL Uwaynat Area, geological overview of Libya (modified after Conant and Gondarzi, 1979)

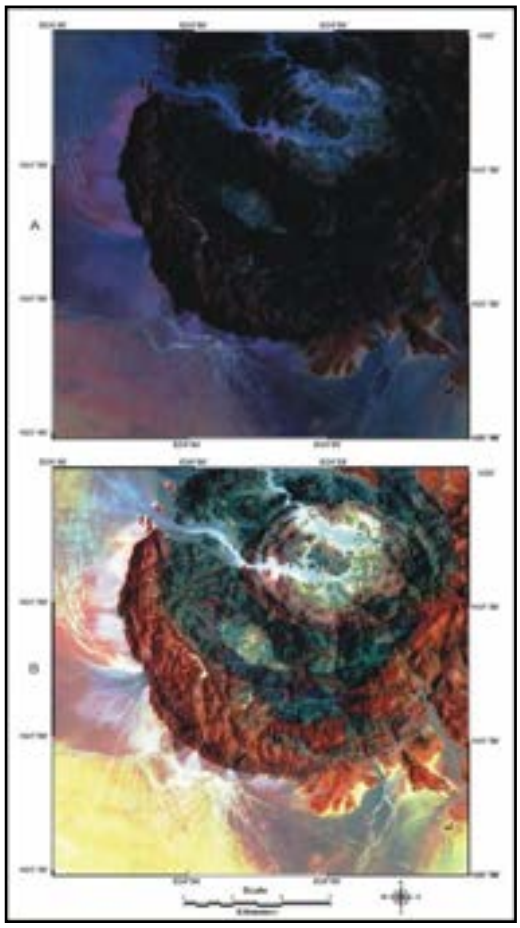


Figure 2: A – Raw Data of Jabal AL Uwaynat
B – Landsat Enhanced Area
Thematic Mapper Bands Combination (ETM 7 = Red, ETM 4 = Green and ETM 2 = Blue)

2. Research Objectives

This study has two major objectives:

1- To test the potential and utility of using Remote Sensing enhancement techniques.
2- To produce update mapping in geologic and geomorphologic study derived from analysis of Landsat Enhanced Thematic Mapper imagery by using techniques that requires less time and less expenses than more conventional field mapping.

3. Justification for Choice of Area

1- Jabal AL Uwaynat area is a classical region of geological study, and the geology is known in considerable detail. However, geomorphologic mapping has lagged behind studies of the geology of the province; in particular, remote sensing data have not been used for geological and geomorphologic analysis.
2- The region has sufficient complexity, both of terrain and surface cover, to permit an evaluation of the applicability of Landsat Enhanced Thematic Mapper data to study of the geomorphology, structure and lithological units in areas of rugged terrain area which is difficult to access.
3-The region possesses a broad range of surface conditions of alkaline complexes so that results in this area should have and has economic problems typical of those which occur throughout Al Kufrah Basin, so that results in this area should have a wider
applicability.
4- Therefore, it is desirable to sum the knowledge of visual satellite image interpretation to produce a series of update maps: geological, tectonic and geomorphologic maps that provides information on the mappable units and highlight the signature and their appearance on satellite images.

4. Jabal AL Uwaynat Area

Jabal AL Uwyanat area is one of a linearly arranged series of five ring complexes straddling the Libyan – Egyptian - Sudanese borders in SE Libya, (Fig.3). The five complexes vary in diameter up to 24 km and are arranged along a 130 km line with a NNE trend (Fig.4). The largest and best exposed is the Jabal AL Uwaynat intrusive complex (Fig.5). This is clearly shown by (Fig.4) which is a simplified version of the map provided by Hunting, (1974). It shows each of Jabal AL Uwaynat and Jabal Archenu complexes as a series of zones composed of complete and incomplete ring dykes, here labeled zone UZ1, UZ2, UZ3, UZ4 and UZ5 for Jabal AL Uwaynat. According to the interpretation presented is (Fig.5), the Jabal AL Uwaynat complex is composed of the following zones:



Figure 3: Location map of the alkaline complexes of SE Libya and nearby Sudan, (Derek. F., et.al., 1987)

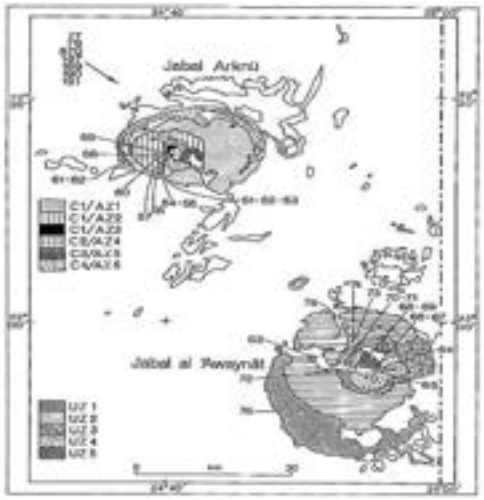


Figure 4: Geological map of the Jabal AL Uwaynat inlier (1= phanerozoic cover; 2= ring complexes; 3= basement rocks) showing the location of the 5major Ring complex: A= Jabal Kissu; B= Jabal AL Uwaynat; C= Jabal Archnu; D= Jabal al Bahri; E= Jabal Babein, (Andre. L., et. al., 1987)

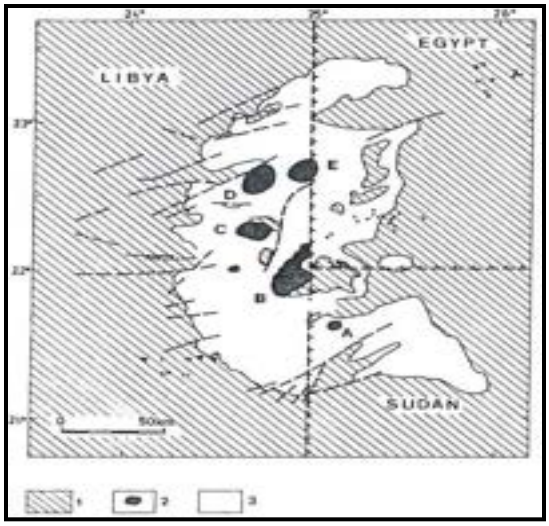


Figure 5: The Jabal Archnu and Jabal AL Uwaynat ring complexes and locality map for the rock specimens used in this paper. Map based on Hunting geology and Geophysics Ltd (1974). C1 - C4: Centres 1-4 in Jabal Arknu. AZ1-AZ6; zones in Jabal Archnu. UZ1-UZ5: zones in Jabal AL Uwaynat.

5. Geologic History

To a certain extent, the stratigraphic framework of Jabal Al Uwayant area developed during the current field programmed is based upon extrapolation from the findings of earlier petroleum – related work in Southern Libya. Few fossils were observed in this area and none were well preserved.

Consequently, the paleontological approach has yielded inconclusive results and the ages adopted for the various parts of the Palaeozoic and Mesozoic succession have not been modified in the absence of clear evidence for making changes. Thus, there is sedimentological evidence for the stratigraphic breaks separating so- called Devonian, Carboniferous and Cretaceous sediments, the absolute ages assigned to the units themselves are, to a certain extent, assumed.

In the case of igneous rocks, the two age dating obtained for rocks from the major ring complexes assign the Jabal Baboir granite to the Ordovician period and the central Jabal AL Uwaynat syenite to the Devonian, (Hunting, 1974). In view of lithologic differences between the complexes and the obvious composite rigin of the complexes themselves, it would be premature to attempt to derive a detailed history of igneous activity based on so little evidence. What can be said is that at least two major episodes of post Precambrian igneous activity are represented in the area.

The large-scale ring complexes in the east area of middle Palaeozoic age whilst the widespread minor intrusions in the west, inasmuch as they intrude sediments believed to be Cretaceous are of late Cretaceous and Tertiary age, (Hunting, 1974).

On the geological map accompanying this report, definite age has been assigned only to those intrusions cutting cretaceous sediments, and due to their proximity, the same age has been applied to those minor intrusions which cut Carboniferous strata in the same area. Likewise, widespread

Trachytic dykes cutting basement adjoining the Jabal Archenu and Jabal AL Uwaynat ring complexes could be related to the Palaeozoic igneous phase. In the interest of separating fact from interpretation on the maps, no age has been assigned to them.

6. The Evaluation of Enhancement Techniques

The major goal of this study is to develop available methodology for producing remote sensing data flow chart for update mapping geologic and geomorphologic study using remote sensing enhancement techniques. The approach adopted in this study has therefore the following steps as illustrated in this flowchart and (Fig. 6),

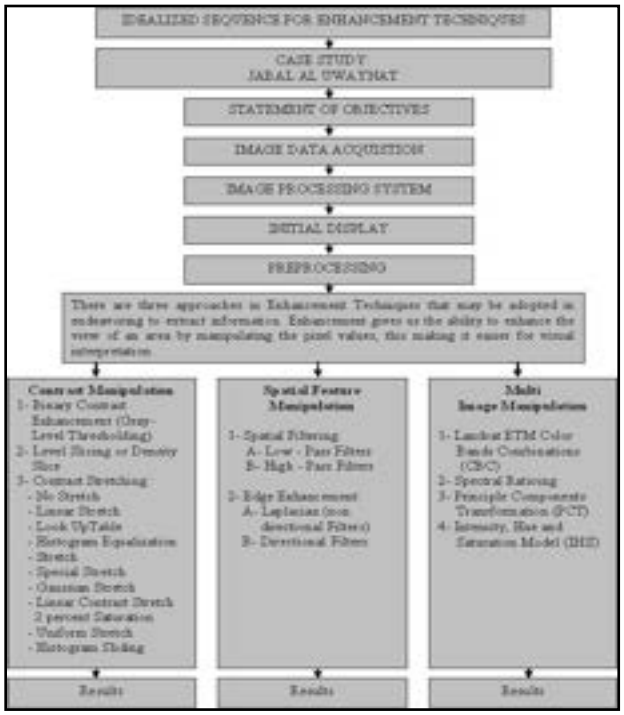


Figure 6: Flowchart illustrating the methodology adopted in the present study, (Lillesand & Kiefer, 1999 and Sabins, 1997)

7. The principal findings of this research are:

1. Landsat ETM 7,4,2 and ETM 5,4,3 band imagery synoptic view of the Jabal AL Uwaynat provided the basis for update geologic interpretation (Fig.7). Published map (Industrial Research Centre (IRC), 2007) on the lithological mappable units were updated (Fig. 8), therefore some discrepancies were found, as follow:

a. IRC(2007)misinterpreted the PLIESTOCENE - HOLOCENE mappable units. Compare between (Figs 7 and 8), the author mapped six mappable units instead of three mappable units.

b. IRC (2007) misinterpreted the PALEOZOIC RING COMPLEX mappable units. Compare between (Figs 7 and 8), the author mapped ten mappable units instead of eight mappable units.

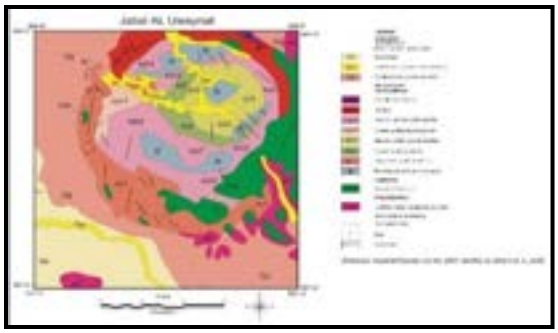


Figure 7: Geologic Map of Jabal AL Uwaynat

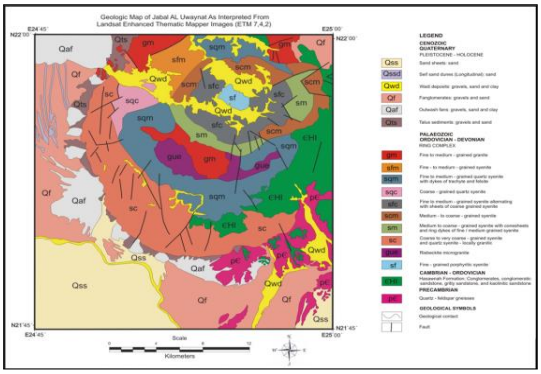


Figure 8: Geologic Map of Jabal AL Uwaynat (IRFigure 8: Geologic Map of Jabal AL Uwaynat (IRC, 2007)

2. To the author's knowledge, no geomorphogic interpretation previously was available (Fig.9), and therefore the present work should greatly highlight the landforms analysis of the district

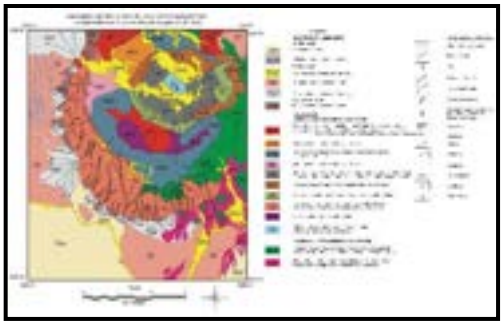


Figure 9: Geomorphologic Map of Jabal AL Uwaynat

3. Published information on the location of major faults and lineaments generally was accurate, although some discrepancies were found, compare the (Figs 10 and 8), and therefore the present work should greatly highlight the structural grain of the district (Fig. 10).

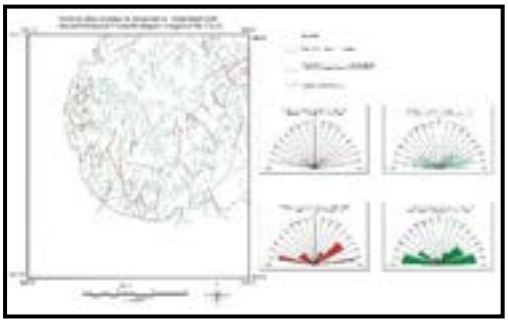


Figure 10: Tectonic Map of Jabal AL Uwaynat

4. The optimum Landsat ETM channels for lithological and structural discrimination was ETM3, ETM5 and ETM7 (Fig.11). Histogram Equalization Contrast Stretch was used to improve image contrast and was effective in highlighting and enhancement of terrain features in rugged terrain as in Jabal AL Uwaynat.

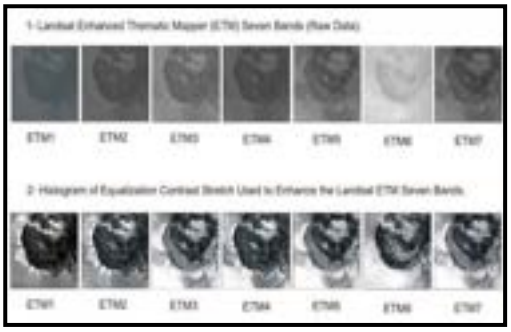


Figure 11: Original Landsat (ETM) images and the dynamic enhancement contrast Stretch Equalization applied in Jabal AL Uwaynat

5. Color composites of different bands (Figs12and 13) have been selected. Each of the three (ETM) color composites has been assigned to a particular color gun of RGB composite. These ten color composites of different band allow for the discrimination of terrain features and material classes .



Figure 12: Landsat (ETM) images resulting from applied of histogram Equalization contrast stretch and color – composite combinations applied in Jabal ALUwaynat

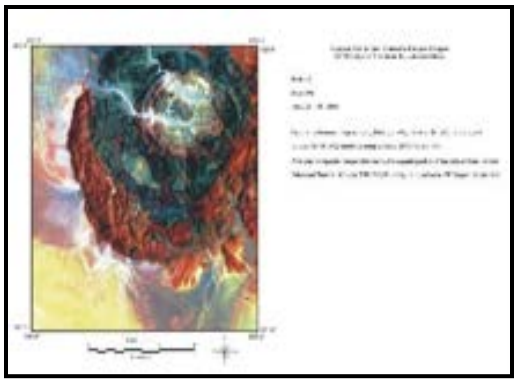


Figure 13: Landsat Enhanced Thematic Mapper Images (ETM 7,4,2) of the Jabal AL Uwaynat

6. Terrain features can be fairly detected and mapped using color combination of three ratioed images. In this study, twelve band ratios were created. Each radioed image enhanced at least three or more terrain features(Fig. 14), but it could not enhance the entire feature. Four colors composite combinations of three band ratios were classified all terrain features (Fig.15 and Table.1)

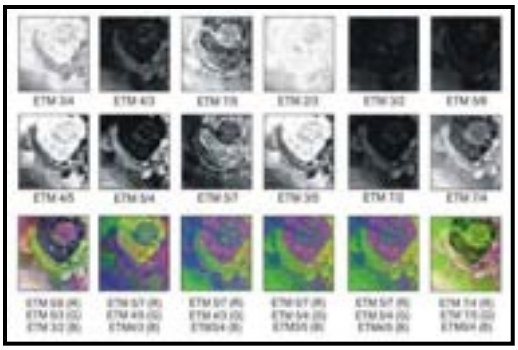


Figure 14. Twelve ratio combinations for Landsat (ETM) applied in Jabal AL Uwaynat and six color – composite combinations of band ratios, applied in Jabal AL Uwaynat



Figure 15: Single color composit combinations, of three Band Ratios ETM 7/4, ETM 7/5 and ETM 5/4

Table 1: Three band ratios applied in Jabal AL Uwaynat

ETM 7/4	(R)
ETM 7/5	(G)
ETM 5/4	(B)
ETM 5/7	(R)
ETM 4/5	(G)
ETM 4/3	(B)
ETM 5/6	(R)
ETM 5/3	(G)
ETM 3/2	(B)

7.

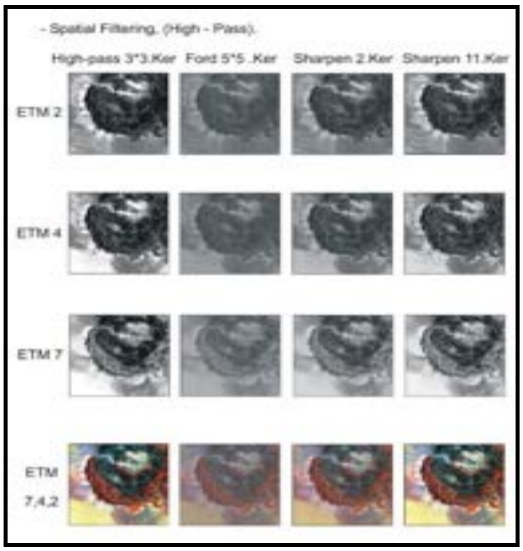


Figure 16: Landsat (ETM 7,4,2) images resulting from application of algorithm spatial filtering High – Pass applied in Jabal AL Uwaynat

7-Another technique was carried out here with Landsat ETM prepared in the form of High - Pass and Low - Pass, and the results were suitable and efficient technique for Jabal AL Uwaynat. (Figs. 16 and 17)

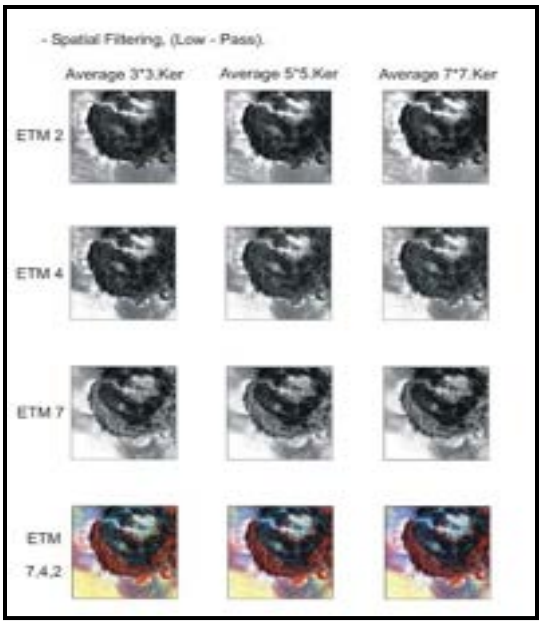


Figure 17: Landsat (ETM 7,4,2) images Resulting from application of algorithm spatial filtering Low – Pass applied in Jabal AL Uwaynat

8. Principle Component Transformation and Intensity – Hue – Saturation Color Space Transformation has Been identified terrain features, but they are not the best and suitable techniques for discrimination terrain features of the study area. (Fig. 18)

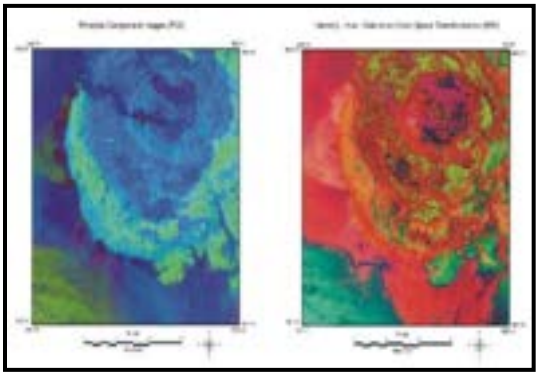


Figure 18: PCI and IHS applied in Jabal AL Uwaynat

Conclusions

Significant results have been obtained for the Jabal AL Uwaynat region of southeastern Libyan.

A study was carried out here with Landsat ETM prepared in the form of different processed images through an interactive program, using a reference image and a color composite of Histogram Equalization Contrast Stretch bands.

In particular, the color composite of the three-color combinations (ETM 7,4,2, and ETM 5,4,3) and three color ratio combinations (Fig.14) revealed interesting details, concerning the update structural (Fig.10) lithological

information (Fig.7) and geomorphic landforms analysis (Fig.9) of the terrain features of Jabal AL Uwaynat.

Acknowledgments

My appreciated to Petroleum Research Centre for give us the chance to do many research studies and my thanks also extended to all colleagues in Geophysics Section at petroleum Research Centre for help us and providing necessary data.

References

Derek, F., Salem, L., Michael. P., an R.A. Cliff., 1987: The Rock - Forming Minerals of the Jabal Arkun and Jabal Al Uwaynat Alkaline Ring Complexes of SE Libya In: The Geology of Libya (eds.) M.J. Salem an M.T. Busrewil Fac. Sci., Univ. Al-Fateh, Tripoli, VII, 2540-2544.

EL-Mehdi, B; Turki, S. M. and Suwesi K. S. (2004).Short Note and Guidebook on the Geology of Al Kufrah Basin AL Uwaynat Area. *IRC*, Tripoli, 67p.
Hunting Geology and Geophysics Ltd.
(1974). Geology of Jabal Al Uwaynat area.
Libyan Arab Republic. Unpublished rep. *Ind. Res. Cent*., Tripoli, Libya, 86p.

Industrial Research Centre (2007). Joint Geological Mapping Project Sheet, Jabal AL Uwaynat
(NF 35-9) Scale 1:250.000, Tripoli, Libya, 99p.

Lillesand T. and Kiefer, R. W. (1999).
Remote Sensing and Image Interpretation. 4th Edition, John Willey and Sons, Inc. New York, 607p.

Sabins F. E. (1997). Principles and Interpretation. 3rd. Edition. W. H. Freeman and Company, New York, 449p.

Impact of Confining Pressure on Reservoir Permeability

[1]H. Sbiga, [2]N. Mousa

[1]Petroleum Research Center, Tripoli-Libya, h.sbiga@prclibya.com
[2]Petroleum Research Center, Tripoli-Libya, n.Issa@prclibya.com
ORCID No. (Author) :0000-0003-4344-0703 scopus Author ID: 55351723700

Abstract

For conventional analysis of plug samples (porosity and permeability), the absolute and relative permeability that are measured on rock samples at ambient conditions (no overburden pressure), can lead to serious errors of estimating reserve, since a11 reservoirs are produced under confining formation pressure. Laboratory measurements were conducted on samples for two fields representing Libyan sandstone reservoirs to investigate absolute and relative permeabilities at ambient and at different confining stresses. In this study the permeability in the lower cretaceous of Nubian sandstone formation is braided fluvial reservoir and the measurement of permeability in this reservoir are variable from high to good and sometimes is very poor during the hole of reservoir based in laboratory routine measurement of permeability.

Experimental data were collected from samples which were selected based on petrotyping technique named (GHE, s) to investigate the effect of confining stress to absolute (Klingenberg) and relative permeabilities. These experiments were conducted on sandstone rock samples (17 plugs) under net overburden pressures reach to (5000 psi).

Our results show a decrease in permeability with increase in overburden pressure. Both correlations for the two fields are found to be polynomial. The relative permeability to water is a little reduced compared with oil relative permeability by applying confining stress. If the measurements are conducted at ambient conditions this may result in over or under estimation of fluid distribution in many situations in reservoir and the error in the estimation can subsequently lead to inaccurate estimates of the hydrocarbon in place.

Key words: Absolute**,** Relative Permeability, Confining, Nubian, Coefficient

تأثير ضغط الحصر على نفاذية المكمن

حســـن .سبيقـــة، نورالدين موسى
المؤلف: د. حســـن مسعـــود سبيقة- مستشار بمركز بحوث النفط ، طرابلس-ليبيا
مساعد المؤلف: نورالدين موسى - مستشار بمركز بحوث النفط
رقم الأوركيد للمؤلف *(Author) :0000-0003-4344-0703* *scopus Author ID: 55351723700*

الملخص

في التحليل التقليدي لعينات السد (المسامية والنفاذية)، قد تؤدي النفاذية المطلقة والنسبية المقاسة على عينات الصخور في الظروف المحيطة (بدون ضغط علوي) إلى أخطاء جسيمة في تقدير الاحتياطي، نظرًا لأن المكامن تتكون تحت ضغط تكويني محصور. أُجريت قياسات مخبرية على عينات من حقلين يمثلان مكامن الحجر الرملي الليبي لدراسة النفاذية المطلقة والنسبية في الظروف المحيطة وتحت ضغوط محصورة مختلفة. في هذه الدراسة، تُصنف النفاذية في العصر الطباشيري السفلي لتكوين الحجر الرملي النوبي كمكمن نهري متشعب، وتتفاوت قياسات النفاذية في هذا المكمن من عالية إلى جيدة، وأحيانًا تكون ضعيفة جدًا، وذلك بناءً على القياسات المخبرية الروتينية للنفاذية.

جُمعت البيانات التجريبية من عينات مختارة بناءً على تقنية تصنيف الصخور (GHE) لدراسة تأثير الضغط المحصور على النفاذية المطلقة (Klingenberg) والنسبية. أُجريت هذه التجارب على عينات من صخور الحجر الرملي (17 عينة) تحت ضغوط صخور علوية صافية تصل إلى 5000 رطل لكل بوصة مربعة.

تُظهر نتائجنا انخفاضًا في النفاذية مع ازدياد ضغط الصخور العلوية. وقد وُجد أن كلا الارتباطين للحقلين متعدد الحدود. تنخفض النفاذية النسبية للماء قليلًا مقارنةً بالنفاذية النسبية للنفط عند تطبيق ضغط الحصر. إذا أُجريت القياسات في الظروف المحيطة، فقد يؤدي ذلك إلى تقدير مفرط أو ناقص لتوزيع السوائل في العديد من حالات المكمن، وقد يؤدي الخطأ في التقدير لاحقًا إلى تقديرات غير دقيقة للهيدروكربون الموجود.

الكلمات المفتاحية: النفاذية المطلقة، النفاذية النسبية، الحصر، النوبي، المعامل

1. Introduction

For any reservoir rock there are two key petrophysical parameters. The first is the capacity of the rock to store fluid, namely porosity. The second is connectivity of the pore space, which allows fluid to flow through the rock, namely permeability. Routine core analysis defines the porosity and permeability magnitude and distribution. SCAL complements this routine data and furnishes information that allows calculation of static fluid distribution as well as dynamic flow performance of a well or reservoir. Moreover, a special core analysis program can assist in defining the most favorable recovery technique to maximize oil recovery and profitability. Downhole log interpretation is considerably enhanced by a SCAL program through the measurement of electrical and acoustic properties of reservoir rocks and fluid saturations from displacement experiments (capillary pressure and relative permeability data). The objectives of performing a SCAL program are to achieve an accurate representation of the reservoir rock characteristics, information that is necessary for reliable reservoir engineering calculations and modelling. In routine core analysis, porosity, absolute and relative permeabilities are measured on rock samples which are not under net overburden pressure. However, under actual reservoir conditions, the rocks experience a net overburden pressure which is equal to the weight per unit area of the vertical overburden column from the reservoir depth to the surface of the earth less the pressure of the liquid in the pores of the rock. Sometimes only the initial net overburden pressure is considered while subsequent increase in this pressure caused by reduction in pore pressure upon reservoir depletion is ignored.

1.1 Objectives

In this paper, the data obtained from permeability, and relative permeability measurements at ambient and at overburden pressure were analyzed and interpreted. The aim was to develop methodologies for reliable prediction using more representative data. The methodologies were desired to possess the following characteristics:

1. Rapidity
2. Cost–effectiveness
3. Deriving correlations for Predicting permeability at any given pressure.

2.Literature Review

The GHE template can be potentially applied to core data for identification of other significant trends in a wide range of crossplots for different parameters (Corbett and Potter, 2004).

Some researchers studied the effect of confining stress on permeability and are similar in their conclusions such as Dobrynin (1962) and Fatt and Davis (1952); they note that the permeability reduce as the overburden pressure applied on the sample due to compressibility. Gray et al. (1963) found that final reduction in permeability happens when the pressure is stabilized. Wilhelmi et al. (1967) on the other hand, developed a method for simultaneous measurement of pore and elastic properties of rock under non-uniform stress. Marek (1979) observed decrease in absolute permeability accompanied by a little decrease in porosity

under overburden pressure. The decrease in permeability was attributed to pore collapse. Owens (1971), Weinbrandt, R. (1972), Sufi, A.H., Ramey H.J, and Brigham (1982) and Amaefule, et al. (1982), have studied the effect of different parameters on permeability. Although, H.S. Ali; et al. (1987) attempt to investigate the effect of overburden pressure on relative permeability, we tried in our study to explore a relationship between confining stress and some rock properties especially relative permeability for samples related to Libyan sandstone reservoirs.

3. Methods

The permeability was measured by using Nitrogen Gas Permeameter instrument (Corex Services). The clean, dry sample is placed in the Hassler-type core holder, and an overburden pressure of 200 psig is applied to the cell, compressing the rubber sleeve around the sample. Nitrogen gas pressure is applied to one end face of the sample, whilst the other end face is open to atmospheric pressure, causing the gas to flow through the sample. The flow of gas is measured at the low pressure (downstream) end face of the sample. The flow rate is measured by passing the gas through one of three laminar flow orifices and measuring the differential pressure developed across the orifice. The transducers and flow orifices are calibrated using a dead weight tester and soap film meter at least once every three months, or when any component is altered or replaced. The air permeability calculated as follows: -

$$Kg = \frac{2000 \times P_b \times Q_g \times \mu_g \times L}{(P_1^2 - P_2^2) \times A} \qquad (1)$$

where:

Kg	=	Gas permeability, mD
Pb	=	Barometric pressure, atm
P_1	=	Upstream pressure, atm
P_2	=	Downstream pressure, atm
Qg	=	Gas flow rate, cc/sec
μ_g	=	Gas viscosity, cp
L	=	Sample length, cm, A= cross sectional area, cm^2

The clean dry samples were placed in CMS-300 instrument which is fully automated permeameter used to determine permeability at overburden pressure. The permeability was measured at five pressure values of (1000-5000) psig. The base permeability was measured at 200 psig overburden pressure. The measurements and the calculations of these parameters are based on the techniques described by API recommended practice 40. Two samples from two oil fields (H, and M) were selected to perform relative permeability test. After the test of gas-oil relative permeability was completed, samples were placed in an oil-filled desiccator and evacuated until no gas bubbles came out of the samples, and then samples were gravimetrically checked to ensure removal of gas from sample pore spaces. The prepared sample was individually placed in a hydrostatic core holder, and an overburden pressure was applied. Simulated formation brine was injected at the top end face of the sample at constant flow rate using HPLC pump. The produced volumes, differential

pressure, time and confining pressure were all monitored and recorded. The brine flood was only terminated when the water cut reached 99.98%. When oil production was ceased, permeability to water was measured and the test was terminated.

The time, oil volume and the total volume were used to calculate relative permeability excel sheets. In these years, the analysis, interpretation and calculation of relative permeability are used by software named "Sendra".

4. Data Collection

To compare the experimental results, the samples were having been chosen sixteen (16) samples with different porosity and permeability from two oil fields (sandstone). The selection was based on Global Hydraulic Elements (GHE, s) technique. Initially, core samples were selected to study the effect of confining stress on flow behavior in the reservoirs. One and a half inch diameter core plugs were cut from full diameter core in the horizontal direction using a diamond core bit with water as the bit coolant and lubricant. The samples were extracted of hydrocarbons using toluene, leached of salt using methanol, and oven dried at 80 ^{o}C for a period of 48 to 72 hours, and then left to cool to room temperature before conventional core analysis commenced. Routine core analysis porosity and permeability measurements were first conducted on the plugs in core Laboratory at Libyan Petroleum Institute (LPI) and the results will be explained in this study. Ten plug samples were selected based on Global Hydraulic Elements technique (GHE, s), Corbet et al. (2004), from wells H1, and H2, (H-field) and six samples from wells M1, M2 which related to M-field (Figures 1, and 2) to investigate the effect of overburden pressure on absolute permeability. In this study we select two samples from both fields as case study.

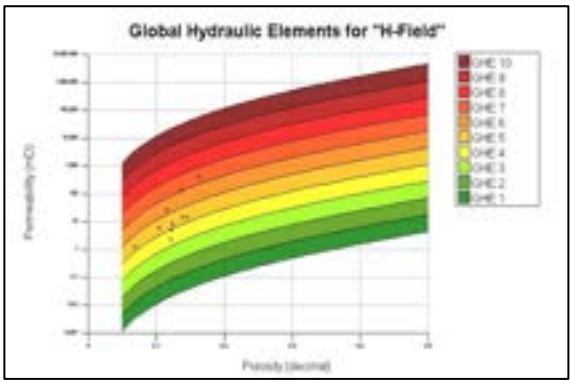


Figure1. Global hydraulic element porosity-permeability crossplot for the ten selected representative samples from "**H**" field.

5. Results and Discussion

5.1 Confining stress on absolute permeability

Core data of porosity and permeability for Nubian Sandstone Formation which belongs to "H" field (two wells, H1, and H2,) are presented in Table 1, while the values of "M" field (two wells M1, and M2) are presented in the same table. The results of averaging horizontal permeability measurements for ten samples selected from sandstone core

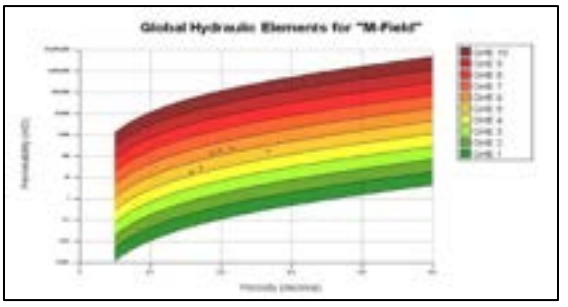


Figure2. Global hydraulic element porosity-permeability crossplot for the six selected representative samples from

samples of "H" field as a function of overburden pressure are presented in Table 2 and in Figures 3. The six core samples from "M" field were selected and the results are presented in the same table and in Figure 4. The data for both cores exhibits a reduction in absolute permeability with increasing overburden pressure. The reduction in permeability values at 5000 psi for samples selected from "H" field, is 7.94%, while in M-field is 15.72% respectively. These reductions in absolute permeabilities with increasing overburden pressure can be attributed to the decrease in pore diameter and rock compaction.

Table 1. Porosity and permeability values of the selected representative samples for studied area.

Sample No.	Depth (ft-in)	Ø (%)	K (mD)	FZI	GHE
H-Field					
7	1385	10.3	6.250	2.1	5
12	1385	14.5	14.34	1.8	5
13	1385	12.2	5.260	1.4	4
18	1386	12.3	8.400	1.8	5
20	1386	12.1	2.430	1.0	4
3	1394	13.7	14.90	2.0	5
5	1394	16.1	424.0	8.3	7
14	1396	6.90	1.280	1.8	5
15	1396	13.6	132.0	6.1	7
21	1397	11.5	26.60	3.6	6
M-Field					
2	7612.	19.7	189.0	3.9	6
4	7614.	15.8	17.80	1.7	5
6	7616.	17.1	29.50	1.9	5
8	7618.	18.6	144.0	3.8	6
9	8608.	26.7	172.0	2.1	5
10	8609.	21.5	237.0	3.8	6

Table 2. Results of averaging absolute permeability at O.B.P for the studied area

Pressure, Psi	Averaging K, mD (H-Field)	Averaging K, mD (M-Field)
200	129.01	95.61
500	127.81	93.69
1000	126.08	90.98
2000	123.38	86.88
3000	121.40	84.05
4000	119.92	81.99
5000	118.77	80.58
Reduction (%)	**7.94**	**15.72**

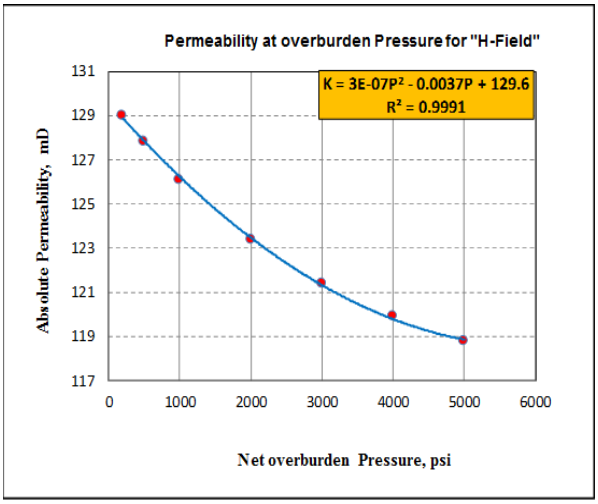


Figure 3. Crossplot of Permeability at O.B.P for H-Field

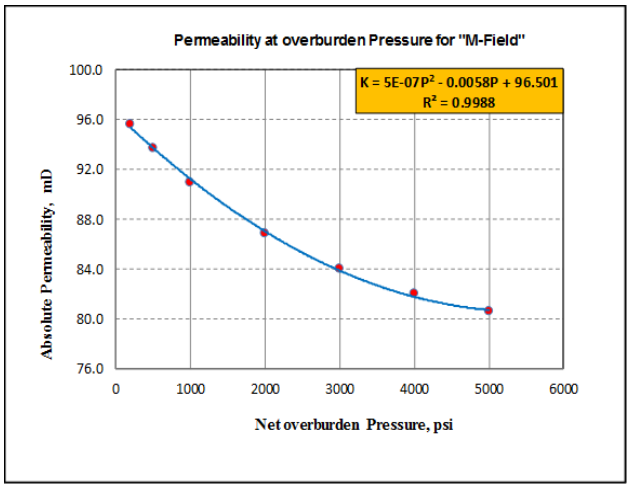


Figure 4. Crossplot of Permeability at O.B.P for M-Field

A polynomial correlation was obtained for study area between permeability and overburden pressure as following:

$$K = a \times P^2 - b \times P + c \qquad (2)$$

Where K and P denote permeability and overburden pressure, respectively. a, b, and c are constants for a given rock sample. These constants are based on individual samples to yield the correlations which represent the samples studied. Statistical error analysis is applied to evaluate the accuracy of the developed relations.

$$K = 3.0E-07 \times P^2 - 0.0037 \times P + 129.6$$
$$K = 5.0E-07 \times P^2 - 0.006 \times P + 96.5$$

According to above correlations, it is easy to find sample's permeability by knowing the pressure.

5.2 Relation Between Confining Stress and Effective Permeability

The recorded data of pressure drop, and flow rate are utilized to calculate the oil effective permeability at irreducible water saturation using Darcy 's law. Table 3 below show the reduction values between 1000 and 5000 psi for two sample for two oil fields, while tables 4, and 5 summarise the calculated results of effective permeabilities at each overburden pressure for two oil fields. Figures 5 and 6 show the effect of overburden pressure on Effective permeabilities for sample # 36 from "H" field, and sample # 18 from "M" field respectively. Our results showed reduction in effective oil permeability and water oil relative permeability, the decrease in effective permeabilities of the fluids may be attributed to the increase in pressure; at early stages (i.e. at low stress) of compression, fissures start to close with small compression in mineral grains (Goodman, 1980). As the stress increases, the rock undergoes bulk compression resulted from pore and grain deformation.

Table 3. Summaries of the reduction in Effective permeability between 1000 and 5000 psig

Pressure (psig)	Ko	Kw
Sample # **36** (H- field)		
1000	69.30	31.60
5000	49.00	24.00
Sample # **18** (M -field)		
1000	203.0	60.0
5000	135.0	45.0

Table 4. Calculated values of effective permeability of oil and water for sample # **36** (**H**-field).

Absolute Permeability(mD) :87 sample #36		
Pressure, Psig	**Ko (mD)**	**Kw (mD)**
1000	69.30	31.60
2000	64.00	29.00
3000	58.30	27.00
4000	54.00	25.50
5000	49.00	24.00

Table 5. Calculated values of effective permeability of oil and water for sample # **18** (**M**-field).

Absolute Permeability(mD) :321 sample #18		
Pressure, Psig	**Ko (mD)**	**Kw (mD)**
1000	203.0	60.0
2000	181.0	57.0
3000	161.0	49.0
4000	149.0	47.0
5000	135.0	45.0

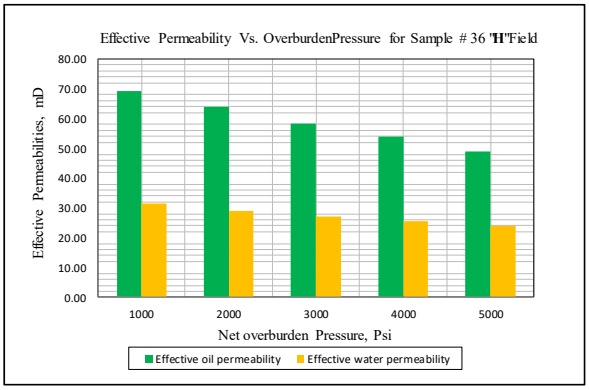


Figure 5. Crossplot of effective permeability for oil and water at different effective stress (Sample # **36**); **H**-Field.

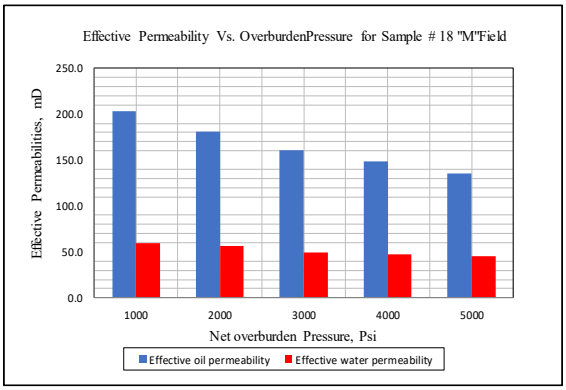


Figure 6. Crossplot of effective permeability for oil and water at different effective stress (Sample # **18**); **M**-Field.

5.3. Effect of Confining Stress on Endpoints

The maximum oil permeability is calculated from the oil effective permeability and absolute permeability measured at the same value of overburden pressure. Maximum oil relative permeability versus overburden pressure plots, are shown in figures (7 and 8). In this study, the reduction is clear in maximum oil relative permeability and maximum water oil relative permeability, the reduction values according to each pressure are represented in table 6.

Table 6. summaries the reduction in Endpoints of relative Permeabilities between 1000 and 5000 Psi.

Pressure (psig)	**Kro (Maximum)**	**Krw (Maximum)**
Sample # **36** (**H**- field)		
1000	0.7965	0.3640
5000	0.5632	0.2908
Sample # **18** (**M** -field)		
1000	0.6321	0.18802
5000	0.4215	0.14000

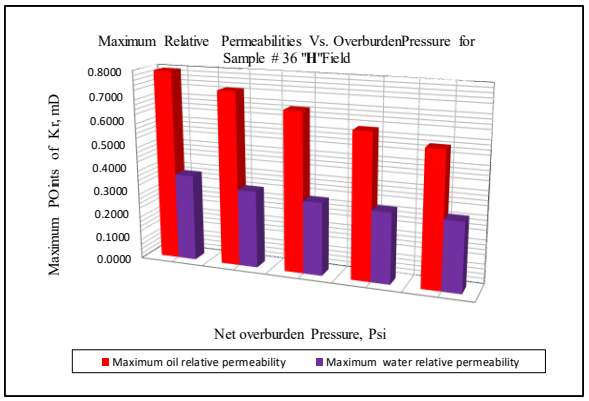


Figure 7. Crossplot of Endpoints for oil and water relative permeabilities at different effective stress (Sample # **36**); **H**-Field.

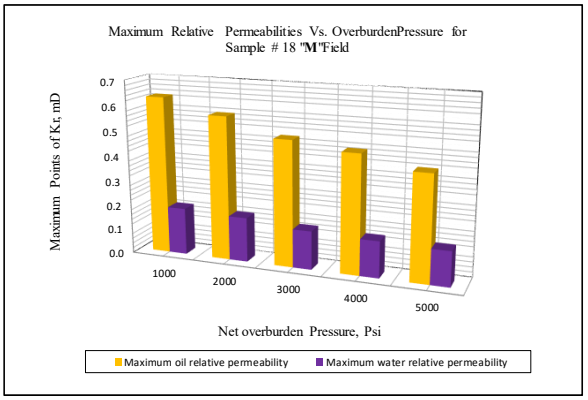


Figure 8. Crossplot of Endpoints for oil and water relative permeabilities at different effective stress (Sample # **18**); **M**-Field.

Using core sample data (sample pore volume, sample length, sample cross-sectional area, effective permeability to oil at irreducible water saturation and irreducible water saturation), fluid data (oil and water/gas viscosities), flood data (time cumulative oil and water volumes, pressure and the flowrate) are used to determine relative permeability to oil and water/gas as a function of water/gas saturation using JBN (Jonson-Bossler-Neuman, 1959), JR (Jones Roszelle, 1978). Figures (9, 10) show the behaviour of relative permeability measurements at ambient and at overburden pressure of two samples selected for studied area (sample # 36 from "H" field, and sample # 18 from "M" field). Our results showed reduction in kr_o with increase in overburden pressure compared to the ignore the effect on kr_w. This may be attributed to; As the overburden pressure start to up, the grain matrix starting to close each other causing a narrow in channels of the pores. For a certain value of S_w, this leads to redistribution of the wetting phase to occupy more pore throat, while this give hint no significant change in kr_w, it leads to more blockage of oil flow and then lead to reduces kr_o.

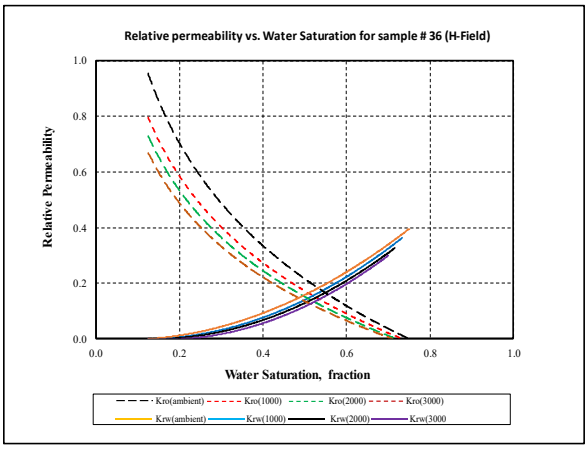


Figure 9. Crossplot of relative permeability test at different effective stresses (Sample # 36); **H**-Field

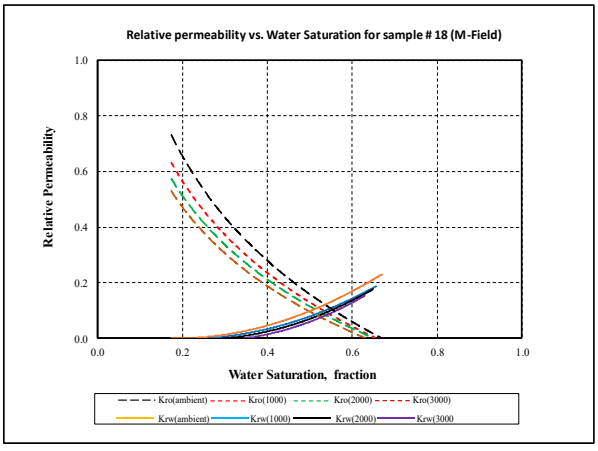


Figure 10. Crossplot of relative permeability test at different effective stresses (Sample # 18); **M**-Field

6. Conclusion

- In this study, the Global Hydraulic Elements (GHE, s) has been used for the first time for Nubian sandstone Libyan reservoirs.
- As the overburden pressure was applied on the samples, the reduction in absolute permeability was observed due to rock compressibility.
- Good relationship between permeability and overburden pressure was obtained using regression analysis.
- A significant Changes have been observed in values of oil relative permeability when the overburden pressure was applied, these values start decreasing while little decrease in values of water relative permeability

Acknowledgments

The author thanks the Petroleum Research Center (PRC) for giving us the chance to do many research studies and to all my colleagues in Reservoir Rock Section for helping us and providing necessary data.

References

Ali, H.S M.; A1-Marhoun M.A.; Abu Khamsin, A.S. and M.S. Celik, U. of Petroleum & Minerals" Effect of overburden pressure on Relative Permeability", March 7 10 1987

Amaefule, J.O., and Handy, L.L.: "The Effect of NOMENCLATURE Interracial Tensions on Relative Oil-Water Permeabilities of Consolidated Porous Media", Soc. Pet. Eng. J. (1982) pp. 371-381.

API recommended practicing 40, February 1998, section 5, 6".

Dobrynin, V. "Effect of Overburden Pressure on Some Properties of Sandstone", Soc. Pet. Eng. J. (Oct.1962) pp. 360-366.

Fatt, and Davis, D.H.: "Reduction in Permeability, with Overburden Pressure", Trans., AIME University of Petroleum and Minerals, December (1952) 195, 329.

Gray, D., Fat'c, I., and Bergamini, G.: "The Effect of Stress on Permeability of Sandstone Cores", Sot. Pet. Eng..J.(June 1963) pp. 95-100, 13718 Trans. AIME, 228. Trans., at the SPE Oil Exhibition and

Jones, S.C., and Roszelle, W.O., "Graphical Techniques for Determining Relative Permeability from Displacement Experiments". J.P.T, May 1978, PP. 807-817

Marek, B.F.: "Permeability Loss in Depletion of Reservoirs", paper SPE 8433 presented at the 54th Annual Meeting, Las Vegas, Sept. 1979, pp. 23-36.

Owens, W., et al: "The Effect of Rock Wettability on Oil-Water Relative

Permeability Relationships", J. Pet. Tech. (July 1971) pp. 873-878.

Sendra Software User Guide version 2013.1, Weatherford Petroleum Consultants AS.

Sufi, A.H., Ramey, H.], and Brigham, W.E.: "Temperature Effects on Relative Permeabilities of Oil-Water", paper SPE 11071 presented at 57th Annual Meeting, New Orleans, Sept. 1982, pp. 26-29.

Weinbrandt, R.:" The Effect of Temperature. On Relative Permeability", Ph.D. Dissertation, Stanford University (1972).

Wilhelmi, B., and Somerton, W.H.: "Simultaneous Measurement of Pore and Elastic Properties of Rock Under Triaxial Stress Conditions", Soc. Pet. Eng. J. (Sept. 1967) pp. 238-294; Trans AIME 240

.

Corrosion Rate Prediction for Underground Gas Pipelines Using Artificial Neural Network (ANN)

[1]*A. Ahmaid*[1]*, and [2]*F. Khoshnaw*

[1]*Sirte Oil company, Brega, Libya, AShwigi@sirteoil.com.ly*
[2] *School of Engineering and Sustainable Development, De Montfort University, UK*
ORCID No. (Author) :0000-0003-4344-0703 scopus Author ID: 55351723700

Abstract

This study addresses the challenge of accurately predicting corrosion rates and estimating the remaining life of underground gas pipelines, which is complicated by the complex interaction of physical factors and environmental conditions. Traditional models are inadequate in capturing these variables, leading to less reliable predictions, which this study aims to address by developing a more accurate and optimized artificial neural network (ANN) model. This study focuses on predicting corrosion rates and estimating the remaining life of underground gas pipelines using ANNs implemented in MATLAB. It incorporates both physical factors, such as maximum corrosion depth and pipe thickness, and environmental variables such as moisture, soil resistivity, and chloride concentration. The analysis identified corrosion depth and wall thickness as significant contributors, influencing material integrity by 20% and 16%, respectively. The optimal ANN model, with a Levenberg-Marquardt structure and one hidden layer of 10 neurons, achieved superior accuracy, with an MSE of 0.038 and R^2 of 0.9999. The study addresses the challenge of accurately predicting corrosion rates and remaining life in underground gas pipelines by developing an optimized ANN model. Its contribution lies in creating a highly accurate prediction tool that outperforms traditional models and enables more informed decisions for pipeline maintenance and safety.

Keywords – pipeline integrity; corrosion rate, ANN

التنبؤ بمعدلات التآكل لخطوط أنابيب الغاز المدفونة تحت الأرض باستخدام الشبكات العصبية الاصطناعية (ANN)

اشرف احميد – فؤاد خوشناو
المؤلف: اشرف احميد – شركة سرت لانتاج النفط والغاز
مساعد المؤلف : فؤاد خوشناو- جامعة دي منتفورت بريطانيا

الملخص

تتناول هذه الدراسة تحدي التنبؤ الدقيق بمعدلات التآكل وتقدير العمر المتبقي لخطوط أنابيب الغاز المدفونة تحت الأرض، حيث تتأثر هذه العملية بالتفاعل المعقد بين العوامل الفيزيائية والظروف البيئية. وتُعد النماذج التقليدية غير كافية لتمثيل هذه المتغيرات بصورة دقيقة، مما يؤدي إلى انخفاض موثوقية التنبؤات. وللتغلب على هذه المشكلة، تهدف الدراسة إلى تطوير نموذج أكثر دقة ومحسّناً باستخدام الشبكات العصبية الاصطناعية (ANN)
تركز الدراسة على التنبؤ بمعدل التآكل وتقدير العمر المتبقي لخطوط أنابيب الغاز المدفونة تحت الأرض باستخدام شبكات عصبية اصطناعية تم تنفيذها باستخدام برنامج MATLAB وقد أُخذت في الاعتبار كل من العوامل الفيزيائية، مثل أقصى عمق للتآكل وسُمك الأنبوب، والمتغيرات البيئية، مثل الرطوبة والمقاومية النوعية للتربة وتركيز الكلوريد. وأظهر التحليل أن عمق التآكل وسُمك جدار الأنبوب يمثلان من أهم العوامل المؤثرة، حيث بلغت مساهمتهما في التأثير على سلامة المادة 20%و16%، على التوالي.

تحقق النموذج الآمثل للشبكة العصبية الاصطناعية، باستخدام خوارزمية Levenberg–Marquardt وطبقة مخفية واحدة تضم 10خلايا عصبية، دقة تنبؤية عالية، حيث بلغ متوسط مربع الخطأ (MSE) = 0.038، ومعامل التحديد $R^2 = 0.9999$. وتتمثل مساهمة هذه الدراسة في تطوير أداة تنبؤية عالية الدقة للتنبؤ بمعدل التآكل والعمر المتبقي لخطوط أنابيب الغاز المدفونة تحت الأرض، بما يتفوق على النماذج التقليدية، ويدعم اتخاذ قرارات أكثر فاعلية فيما يتعلق بصيانة خطوط الأنابيب وسلامتها.

الكلمات المفتاحية :سلامة خطوط الأنابيب؛ معدل التآكل؛ الشبكات العصبية الاصطناعية (ANN)

1. Introduction

Pipelines are essential for the safe and efficient transport of petrochemical products, connecting production sites with industrial and consumer centers while supporting economic growth and reducing dependence on higher-emission transportation methods M. E. A. B. Seghier; etal (2021). Underground gas pipelines provide additional safety and environmental benefits through continuous monitoring and early fault detection. However, external corrosion resulting from soil–pipe interactions remain a major threat to pipeline integrity, causing safety hazards, environmental damage, costly maintenance, and potential loss of public confidence M. S. Liew; etal (2012).

Corrosion rate, commonly measured in millimeters or inches per year, indicates the speed of metal deterioration caused by environmental chemical reactions. It is influenced by factors such as material properties, chemical composition, temperature, and corrosive agents. Remaining life estimates the safe operational period of a structure based on corrosion rate and material loss, enabling effective maintenance planning and safe operation (Derbo Steel Pipe Co., Ltd. [Online],(2023).

Maintaining pipeline integrity requires understanding corrosion mechanisms and implementing effective prevention and control strategies. This study aims to enhance the predictive capability of Artificial Neural Networks (ANNs) for corrosion forecasting. A reliable ANN-based approach can improve asset management, reduce failure risks, and support safer pipeline operations. ANN models offer advantages including high prediction accuracy, adaptability, and integration with inspection systems, helping reduce maintenance costs, extend pipeline lifespan, improve operational reliability, and optimize investment returns R. M. Mahmoodian and C. Q. Li, (2020).

Biezma et al. (2018), developed a fuzzy logic model to predict external pipeline corrosion rates and support inspection planning. Shaik etal. (2020), used Support Vector Machines (SVM) to predict metal loss defects in Sudanese oil pipelines, achieving 93% accuracy. In another study, Shaik etal, (2021), proposed an ANN-based model for predicting pipeline lifespan and classifying metal loss defects.

1.1 Research gap: Although previous studies advanced corrosion prediction, most focused on limited corrosion types and input variables, restricting practical applicability. This study addresses these limitations by developing an optimized ANN model using the Levenberg–Marquardt algorithm to analyze seven corrosion types, integrate physical and environmental factors, and predict corrosion rate, remaining life, and corrosion type.

2. Methodology

Study Area: This study analyzes a 34-inch underground gas pipeline operated by Sirte Oil Company in Libya using 200 samples from intelligent pigging data collected in

2009 and soil properties including resistivity, moisture, and chloride content.

2.1 Data Calculations: Two key ANN outputs, corrosion rate and remaining life, were calculated from the input data. Corrosion rate was determined using the Point-to-Point analysis method in accordance with API 570 standards, while remaining life was estimated based on corrosion progression and wall thickness loss E.S. Menon (2005), and S. R. Pedapati,etal (2022).

2.2 Meteorological Data: The ANN model uses corrosion distance, maximum depth, current thickness, pipe age, moisture, soil resistivity, and chloride content as inputs, while predicting corrosion rate, remaining life, and corrosion type (see Figure 1).

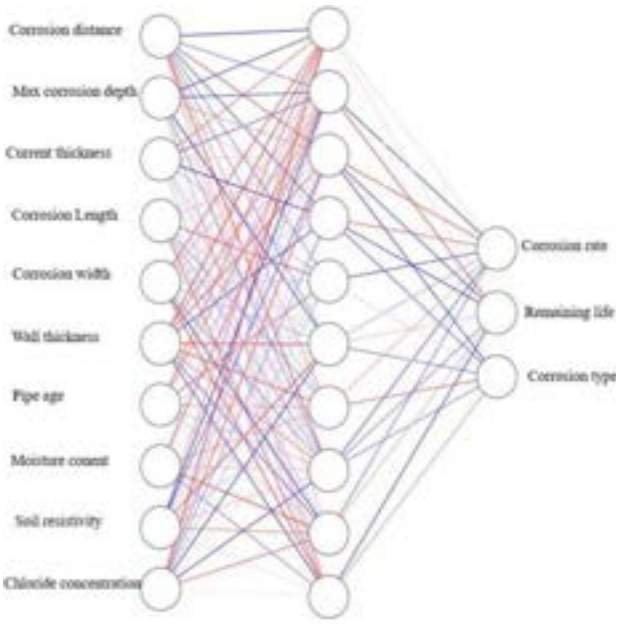


Figure 1. The ANN architecture

2.3 Data processing: Data preprocessing involved removing duplicates, handling missing values, and normalizing variables to improve ANN performance. Corrosion types were encoded numerically from 1 to 7, as shown in table 1, facilitating ANN training and subsequent decoding into interpretable classifications B. Akhlaghi, etal; (2023).

Table 1. Encoding of corrosion types

Corrosion Type	Encoding
Pinhole corrosion	1
Pitting corrosion	2
General corrosion	3
Circumferential grooving	4
Axial grooving	5
Circumferential slotting	6
Axial slotting	7

2.4 Classification of corrosion types: Metal loss anomalies were classified using intelligent pigging and nondestructive testing data figure 2. The parameter A was derived from pipe thickness (t), where A = 10 mm when t < 10 mm, and A = t when t ≥ 10 mm, H. Zhang etal; (2021).

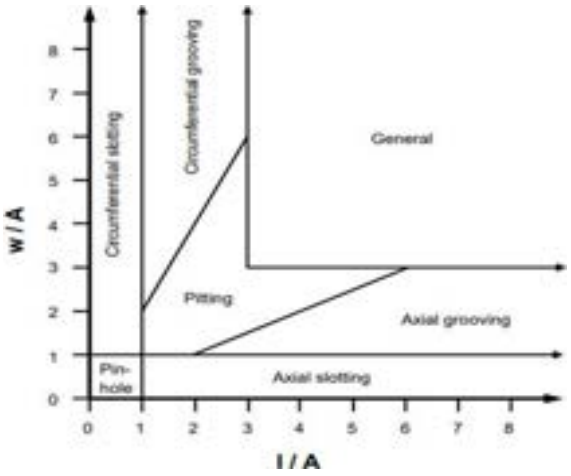


Figure 2. Classification of metal loss anomalies per dimension class

2.5 ANN model development: A The study used a feedforward neural network with 10 input variables, 3 output variables, and 1–3 hidden layers containing 5–15 neurons. Different network architectures, layer sizes, and data divisions were evaluated iteratively to identify the optimal configuration. The MATLAB Data Division function was used to randomly divide the data into training, validation, and testing sets using a 70:15:15 ratio. Sigmoid, tanh, and ReLU activation functions were considered to capture nonlinear relationships. The model was trained through data preprocessing, forward propagation, backpropagation, and optimization, and its performance was evaluated using MSE and R^2.

3. Results

3.1 Meteorological Analysis: Statistical analysis was conducted on variables used in the ANN model, including corrosion distance, corrosion depth, wall thickness, pipe age, moisture content, soil resistivity, and chloride concentration. Results showed an average corrosion rate of 0.11 mm/year and remaining life ranging from 0.01 to 59.14 years. These findings support failure prediction and maintenance planning while evaluating optimal ANN configurations.

Table 2 shows significant correlations with corrosion rate. Maximum corrosion depth has a near-perfect positive correlation (0.9963). Thickness is weak (0.2334). Corrosion width (0.574) and wall thickness (0.8178) are strong. Soil resistivity shows a moderate negative correlation (-0.495).

Table 2. Correlation coefficient and P-values

Variable	Correlation Coefficient	P-value
Corrosion distance	0.4964	$7.707*10^{-14}$
Max corrosion depth	0.9963	0
Current thickness	0.2334	$0.00087*10^{-14}$
Corrosion length	0.3809	$2.623*10^{-8}$
Corrosion width	0.574	0
Wall thickness	0.8178	0
Moisture content	0.509	$1.421*10^{-14}$
Soil resistivity	-0.495	$9.311*10^{-14}$
Chloride concentration	0.5065	$1.976*10^{-14}$

Figure 3 highlights the multifaceted factors influencing corrosion. The depth of corrosion depth (20%) and wall thickness (16%) are crucial factors in susceptibility.

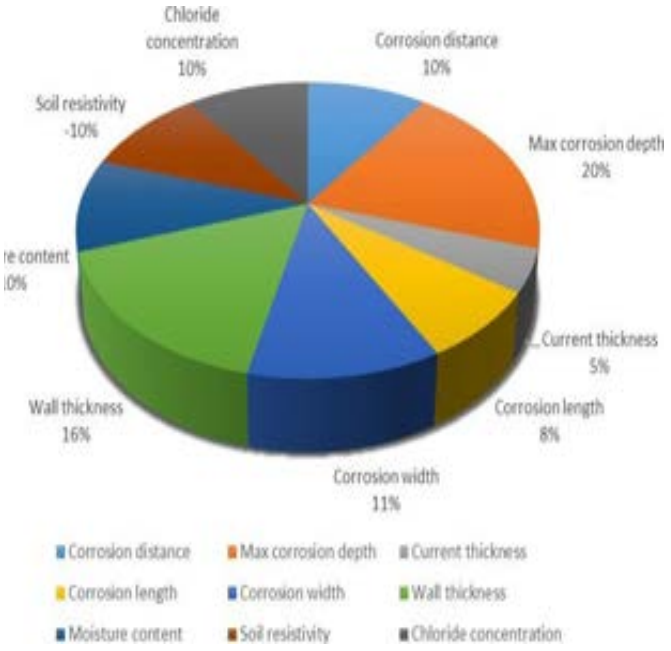


Figure 3. Contribution factor

3.2 Comparative Analysis of ANN Model Experiments: The ANN experiments compared training algorithms using MSE

and R^2 as performance metrics. The Levenberg–Marquardt algorithm achieved the best results, particularly with a single hidden layer, reaching an MSE of 0.03890 and an R^2 of 0.9999 using 10 neurons. Results indicate that moderate network complexity yields optimal performance, whereas additional layers do not necessarily improve accuracy. Figure 4 illustrates a feedforward ANN's structure with input-to-output data flow.

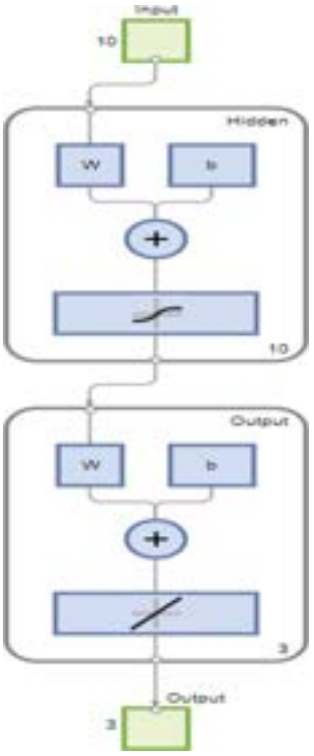


Figure 4. Architecture of optimal model

Figure 5 in MATLAB shows the ANN training state, including gradient, learning rate, and validation performance across epochs. At epoch 92, the gradient (0.16419) indicates ongoing learning. A low learning rate (0.0001) improves stability but slows convergence. A validation check value of 6 suggests the model may be nearing optimal performance or potential overfitting, guiding training adjustments.

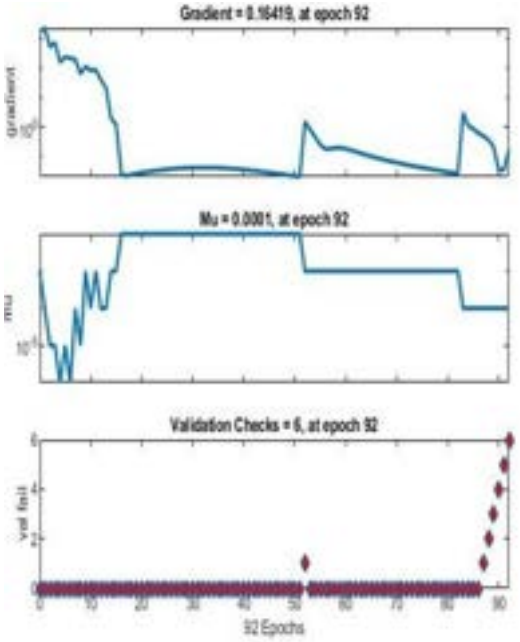


Figure 5. Training state plot

Figure 6 shows that epoch 86 records the highest validation performance at 0.03891, indicating successful handling of unseen data.

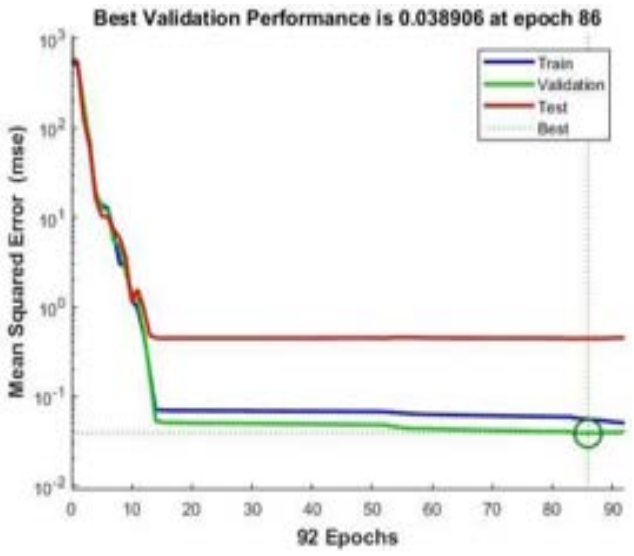


Figure 6. Performance plot

Figure 7 shows ANN regression performance comparing actual and predicted corrosion rates.

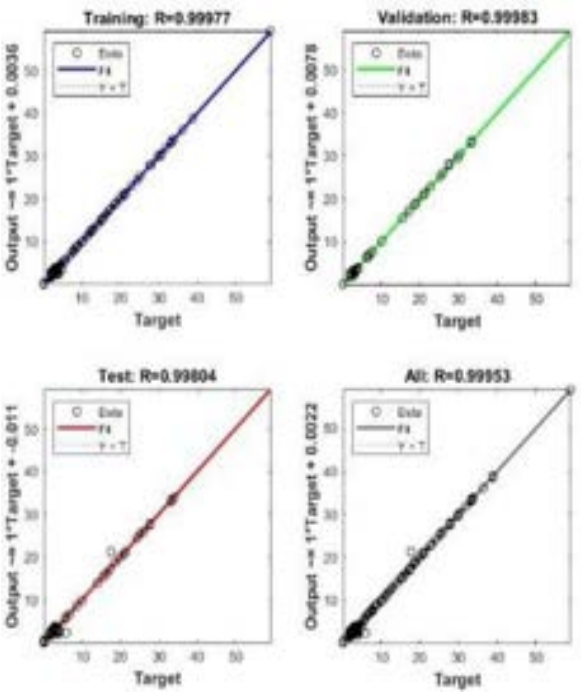


Figure 7. ANN model regression plots

Table 3 compares actual and predicted corrosion rate, remaining life, and corrosion type for 24 unseen samples. Most errors are below 10%, indicating good accuracy. Remaining life predictions are highly accurate (0.02%–1.70%).

Table 3. Comparison between the actual values and predicted values of corrosion rate

No	Actual values			Predicted values			Error percentage %		
	Corrosion rate	Remaining life	Corrosion type	Corrosion rate	Remaining life	Corrosion type	Corrosion rate	Remaining life	Corrosion type
1	0.1	51.13	3	0.1	51.32	3	0	0.37	0
2	0.13	29.76	3	0.14	29.64	3	7.69	0.4	0
3	0.12	36.29	3	0.13	36.25	3	8.33	0.11	0
4	0.11	38.8	2	0.11	38.78	2	0	0.05	0
5	0.21	6.98	3	0.19	7.07	3	9.52	1.29	0
6	0.13	29.76	3	0.14	29.74	3	7.69	0.07	0
7	0.11	41.51	2	0.1	41.35	3	9.09	0.39	0.5
8	0.2	10.17	2	0.17	10.16	3	15	0.09	0.5
9	0.11	44.45	3	0.11	44.39	3	0	0.13	0
10	0.12	36.29	2	0.11	36.22	2	8.33	0.19	0
11	0.12	33.96	3	0.13	33.84	3	8.33	0.35	0
12	0.11	38.8	2	0.11	38.78	2	0	0.05	0
13	0.12	33.96	3	0.12	33.85	3	0	0.32	0
14	0.13	31.79	3	0.14	31.8	3	7.69	0.03	0
15	0.12	36.29	3	0.13	36.16	3	8.33	0.36	0
16	0.11	38.8	3	0.12	38.77	3	9.09	0.08	0
17	0.09	59.14	4	0.09	59.13	4	0	0.02	0
18	0.14	24.42	3	0.15	24.4	3	7.14	0.08	0
19	0.1	9.99	3	0.11	9.82	3	10	1.7	0
20	0.08	15.56	2	0.1	15.44	2	25	0.77	0
21	0.06	33.38	2	0.07	32.94	3	16.67	1.32	0.5
22	0.08	18.98	2	0.09	19.02	2	12.5	0.21	0
23	0.1	9.99	3	0.12	9.83	3	20	1.6	0
24	0.07	25.24	2	0.08	25.48	2	14.29	0.95	0

Figures 8, 9 and 10 compare actual and predicted corrosion rates, remaining life, and corrosion types across 24 samples.

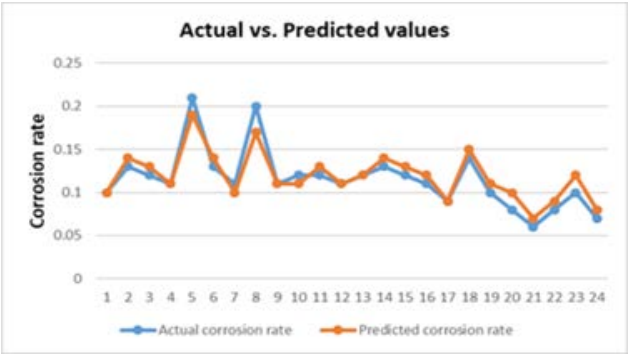


Figure 8. actual vs. predicted values for corrosion rate

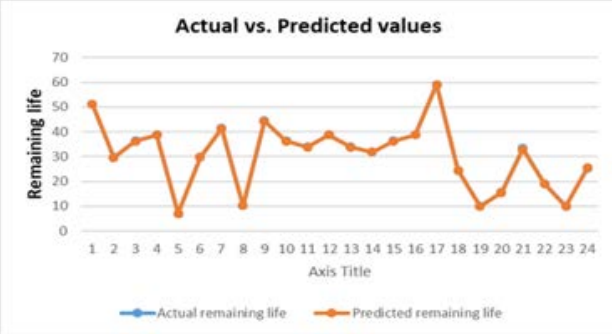


Figure 9. actual vs. predicted values for remaining life

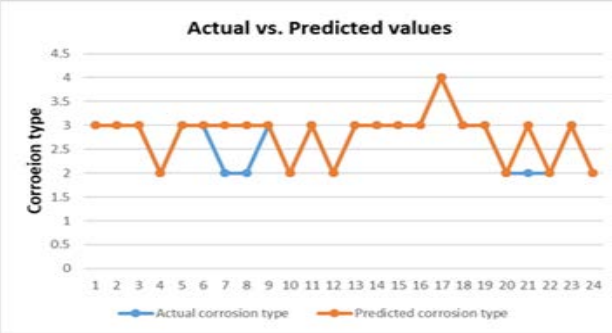


Figure 10. actual vs. predicted values for corrosion types

4. Results and Discussion

The results demonstrate that physical factors, particularly maximum corrosion depth and wall thickness, have the greatest influence on pipeline corrosion progression. Maximum corrosion depth exhibits an exceptionally high correlation (0.9963) with corrosion rate. Environmental factors show weaker correlations.

The ANN model optimized using the Levenberg–Marquardt algorithm and a single hidden layer with 10 neurons achieved the best performance, with an R^2 of 0.9999 and an MSE of 0.03890. Increasing network complexity by adding hidden layers did not improve accuracy, highlighting the importance of selecting a balanced architecture. High R^2 values across training, validation, and testing datasets indicate strong generalization and reliable remaining-life predictions.

Evaluation on unseen data showed that most predictions were within a 10% error range. Remaining life predictions were particularly accurate, with errors ranging from 0.02% to 1.70%. Although minor discrepancies occurred in corrosion-type classification, the model consistently provided reliable predictions of corrosion rate, remaining life, and corrosion type, supporting its application in pipeline integrity management.

The feedforward ANN architecture, employing a hyperbolic tangent sigmoid activation function in the hidden layer and a linear transfer function in the output layer, enabled stable and effective learning. Model performance was further enhanced through proper data preprocessing and careful hyperparameter tuning, including learning rate and layer configuration.

ANNs offer significant advantages for corrosion prediction, including high accuracy, adaptability to new data, and compatibility with inspection technologies such as in-line inspection systems.

4.1 Limitations: The study did not incorporate additional factors such as soil pH and microbial activity due to time constraints. Furthermore, optimizing ANN architecture and hyperparameters requires extensive experimentation and validation.

4.2 Implications: The proposed ANN model accurately predicts corrosion rate and remaining life, enabling targeted maintenance, reducing failure risks and costs, and extending pipeline lifespan. Future improvements may be achieved by incorporating additional environmental factors and integrating the model with existing inspection technologies.

5. Conclusion

- The contribution factor emphasizes that while the depth of corrosion (20%) and wall thickness (16%) are key determinants, the cumulative influence of factors like corrosion area width, moisture content, and soil resistivity crucially shapes material integrity.
- Through a systematic exploration of various ANN architectures, an optimal feedforward Levenberg-Marquardt configuration was determined that balances model complexity with computational efficiency.
- The developed ANN model demonstrated a high level of accuracy in predicting the corrosion rate of underground gas pipelines. The results indicated that the ANN model outperformed traditional statistical models and other machine-learning techniques in terms of prediction accuracy.
- By accurately predicting corrosion rates, ANN models can significantly reduce maintenance costs for energy companies, enable targeted repairs, and extend pipeline lifetimes, ensuring consistent production and maximizing return on investment.

6. Recommendations:

- Include additional environmental factors like soil pH and microbes for better accuracy.
- Continue tuning ANN architecture to improve performance.
- Combine ANN with inspection tools for comprehensive monitoring.
- Collect more varied data to enhance model generalization.
- Develop user-friendly tools for maintenance planning.
- Regularly validate and update the model with new data.
- Evaluate cost benefits to support ANN adoption

Acknowledgements

The authors gratefully acknowledge Sirte Oil Company, Libya, for providing pipeline inspection data and operational support essential to this study.

I also would like to sincerely thank Dr. Fuad Khoshnaw of the School of Engineering and Sustainable Development, De Montfort University, UK, for his invaluable guidance, supervision, and support throughout this research.

Finally, I appreciate the constructive feedback from colleagues and reviewers, which improved the quality of this research.

References

M. E. A. B. Seghier, B. Keshtegar, M. Taleb-Berrouane, R. Abbassi, and N. T. Trung, “Advanced intelligence frameworks for predicting pitting corrosion depth in oil and gas pipelines,” *Process Safety and Environmental Protection*, vol. 147, pp. 818–833, 2021.

M. S. Liew, E. S. Lim, K. L. Na, and N. F. Mohd Sidek, “Parametric study on the factors of external corrosion of offshore pipelines in Malaysia,” 2012.

API 5L X52 PSL1 LSAW Pipe, 34 Inch, SCH 40," Derbo Steel Pipe Co., Ltd. [Online]. Available: https://www.derbosteelpipe.com/api-5l-x52-psl1-lsaw-pipe-34-inch-sch-40.html. Accessed on: Jul. 2, 2023.

R. M. Mahmoodian and C. Q. Li, "Failure assessment and safe life prediction of corroded oil and gas pipelines," J.S.E, vol. 151, pp. 434-438, 2017. Abubakirov, M. Yang, and N. Khakzad, “A risk-based approach to determination of optimal inspection intervals for buried oil pipelines,” *Process Safety and Environmental Protection*, vol. 134, pp. 95–107, 2020.

M. V. Biezma, D. Agudo, and G. Barron, “A fuzzy logic method: Predicting pipeline external corrosion rate,” *International Journal of Pressure Vessels and Piping*, vol. 163, pp. 55–62, 2018.

N. B. Shaik, S. R. Pedapati, S. A. A. Taqvi, S. Ahsan, and F. A. Abd Dzubir, “Classification of faults in oil and gas pipelines using support vector machines,” *Pertanika Journal of Science and Technology*, vol. 28, no. S1, pp. 173–184, 2020.

N. B. Shaik, S. R. Pedapati, A. R. Othman, K. Bingi, and F. A. A. Dzubir, “An intelligent model to predict the life condition of crude oil pipelines using artificial neural networks,” *Neural Computing and Applications*, vol. 33, no. 21, pp. 14771–14792, 2021.

E.S. Menon, Gas Pipeline Hydraulics, CRC Press, 2005.S. R. Pedapati, N. B. Shaik, and F. A. B. Dzubir, “Remaining useful life prediction of a piping system using artificial neural networks: A case study,” *Ain Shams Engineering Journal*, vol. 13, no. 2, p. 101535, 2022.

B. Akhlaghi, H. Mesghali, M. Ehteshami, J. Mohammadpour, F. Salehi, and R. Abbassi, "Predictive deep learning for pitting corrosion modeling in buried transmission pipelines," Process Safety, vol. 174, pp. 320-327, 2023.

H. Zhang, S. Sha, C. Willis, and P. Chen, "Feasibility Study of Pinhole Inspection via Magnetic Flux Leakage and Hydrostatic Testing in Oil & Gas Pipelines," in IOP Conference Series: Materials Science and Engineering, vol. 1043, no. 2, p. 022053, 2021.

National Oil Corporation
Petroleum Research Center

Volume.26 (2026)

Desulfurization of Libyan Fuel Oil by Solvent Extraction

Abdulathim. S. Juroud
Petroleum Reseach Center, Tripoli-Libya, *a.juroud@prclibya.com*
ORCID No. : 0009-0001-6937-7194

Abstract:

New strict environmental regulations to reduce sulfur content in liquid fuel have been established. Thiophene derivatives can be considered as the key substances to be separated from liquid fuels. This research reports the ability of the solvent extraction, in liquid-liquid single and multistage extraction steps, to remove thiophene derivatives. Four liquid solvents have been used in the extraction. These are N-methyl-2-pyrolidone (NMP), acetonitrile (MeCN), methanol (CH_3OH) and water (H_2O). This work main contribution is to provide a comprehensive and systematic equilibrium data for the extraction of dibenzothiophene (DBT), diebenzothiophene sulfone (DBTs) and their mixture respectively. An attempt to predict equilibrium extraction data was also carried out using the estimated binary interaction parameters for two liquid non-ideal phase behaviour models. These are UNIQUAC and NRTL. Such data and predictions are to the best of the author knowledge are lacking from the open literature. Predictability of NRTL and UNIQUAC temperature independent models has been evaluated and was found to be very satisfactory. Binary interaction parameters for these two models for diesel fuel constituents and solvents were estimated based on the UNIFAC whereas that for DBT–Solvent pair was estimated based on comparison of DBT compositions measured and calculated in the fuel layer.

Key words: Desulfurization, extraction, solvents, sulfur compounds and Hysys.

نزع مركبات الكبريت من النفط الخام الليبي عن طريق عملية الاستخلاص

عبدالعظيم سالم جرود
المؤلف: م. عبدالعظيم سالم جرود اخصائى اول بمركز بحوث النفط ، طرابلس-ليبيا

الملخص

في السنوات الأخيرة ثم وضع قوانين بيئية صارمة لخفض نسبة الكبريت في الوقود. مشتقات الثيوفين (Thiophene derivatives)تعتبر المفتاح لفصل هذه المواد من الوقود. هذا البحث يتناول قابلية المذيبات فى الفصل للمرحلة الواحدة (Single stage) ولعدة مراحل (Multistages) لإزالة مشتقات الثيوفين واكسدة هذه المشتقات من الهيروكربونات الاروماتية بواسطة المذيبات القطبية. (Polar solvent) أربع أنواع من المذيبات استعملت في الاستخلاص. وهى الميثانول (CH_3OH)، اسيتونيتريل (MeCN) ، NMP و الماء(H_2O) المساهمة الرئيسية في هذا البحث هي تزويد بيانات اتزان شاملة ومنظمة لاستخلاص داى بينزوثيوفين (DBT) و داى بينزوثيوفين سلفون (DBTS) وخليط منهما على التوالى. وكذلك محاولة التنبؤ بمتغيرات التداخل (Binary interaction parameter) لسائلين(Liquid-liquid) سلوكهما غير مثالى(Non ideal) ومقارنتها بالمتغيرات العملية من حيث معرفة مكونات DBT وباستخدام معادلتين هما: Uniquac, وNRTL
تجارب الاستخلاص لمركبات الكبريت كانت عند 25°م عندما ثم استخدام MeCN ، NMP ، H_2O اما عند استخدام الميثانول فكانت عند 25° م ، 40° م.
اداء وفعالية الاستخلاص عند ظروف التشغيل المختلفة ثم حسابها، حيث وجد ان تاثير درجة الحرارة على استخلاص الميثانول ضئيل جدا بين 25° م ، 40° م ومعدل نزع الكبريت واطىء. وكذلك وجد ان (NMP) له افضل تاثير فى نزع (DBT) من وقود الديزل عند درجة حرارة الغرفة حيث كانت كفاءة الاستخلاص 90%.
المذيبات المستخدمة نستطيع بسهولة تدويرها او اعادة استعمالها بالتبخير او التقطير(Evaporation or distillation)
الاستخلاص دو الست مراحل كان فعالا جدا فى استخلاص (DBT) باستعمال الميثانول.
الهيروكربونات المفقودة ومعدل نزع الكبريت كلاهما يؤثر على(Solvent effectiveness factor K) وهو متغير يعتمد على عدد المراحل ونسبة المذيب الى الوقود ونوع المذيب المستخدم.
معامل الفاعلية (K) لاستخلاص الميثانول يكون فى المرحلة الواحدة أفضل من متعدد المراحل. معامل الفاعلية(K) لاستخلاص الاسيتونيتريل (MeCN) لمرحلتين(Two stages) هو 11.4 عندما كانت نسبة المذيب الى الوقود هى 3.

الكلمات المفتاحية: استخلاص النفط، نزع الكبريت، الضغط، الخصائص البتروفيزيائية

1.Introduction

Crude oil is the largest and most widely used source of energy in the world. Major portions of the crude oils are used as transportation fuels such as gasoline, diesel and jet fuel. However, (Howard F. Rase,2000, and Houalla, M., etal 1978,) contains sulfur, typically in the form of organic sulfur compounds. The sulfur content and the API gravity are two properties which have a great influence on the value of the crude oil. The sulfur content is expressed as a percentage of sulfur by weight and varies from around 0.04% in light crude oil to 5% in heavy crude oil depending on the type and source of crude oil. Sulfur compounds exist in various forms and can be classified into four main groups: mercaptans, sulfides, disulfides and thiophenes, (Walid A. Al-Naeem,2004, and (Katzer, J. R etal,1979)

Petroleum-derived middle or heavy feed stocks, such as light oil, usually contain high proportion of sulfur and nitrogen impurities (Dong, D.; etal ,1997) However, the catalysts are not active in removing refractory sulfur compounds that are satirically hindered. This is particularly true in the case of sulfur compounds like thiophenes and multi ring aromatic sulfur compounds, such as dibenzothiophene (DBT) and its derivatives, 4,6- dimethyldibenzothiophene (4,6-DMDBT), (Kabe, T.; etal,1992, and Girgis, M. J.; Gates, B. C, 1991).

In order to meet future fuel specifications, such sulfur compounds must be removed or reduced to target limits within a regulatory period. Much effort has been devoted to developing techniques that can reduce or remove such refractory sulfur compounds by oxidation/extraction and biodesulfurization, (Gutberlet, L. C.; Bertolacini, R. J.1983). In general, diesel fuel and gasoline contain 20 to 30 percent aromatics but less than 1 percent sulfur, so removing the sulfur without removing the aromatics is difficult, particularly in the HDS process which also potentially hydrogenates (saturates) aromatics. It is preferable, however, to include certain aromatic compounds such as toluene and naphthalene in the fuel as they contribute significantly to fuel quality. (A. Konig, G.;etal, 2002 and C. Song, Catal.,2003)

2. Methodology

Model compounds: Two types of sulfur model compounds are selected to evaluate the extraction of sulfur compounds. The chosen of sulfur model compounds are as follows:
Dibenzothiophene (DBT) and dibenzothiophene sulfone (DBTS).
These were supplied by Aldrich, and their characteristics and physical properties are given in Table (1).
Solvents: Methanol (CH_3OH), N-methyl-2-pyrolidone (NMP), acetonitrile (MeCN) and water (H_2O), first three were supplied by BDH Laboratory, Their specific gravity and boiling point are given in Table (1).

Table 1. physical properties of chemical materials:

Chemical materials	Physical properties					Purity by Wt%
	Formula	M.wt(g/gmol)	B. P (°C)	M. P (°C)	ρ (g/ml) @20° C	
Methanol	CH_3OH	99.8	64.65	-97.68	0.811	99.8
NMP	C5H9NO	99	205	-24	1.03	99
Acetonitrile	C_2H_3N	99.9	82	-48	0.786	99.9
DBT	$C_{12}H_8S$	98	331.45	98.67	1.125	98
DBTS	$C_{12}H_8O_2S$	97	-	231-233	-	97

M.wt=Molecular weight (g/gmol), M. P=Melting point (°C), B.P=Boiling Point (°C), ρ=Density (g/ml)

Reference diesel fuel: This diesel fuel has been used as a model for diesel fuel and it has negligible sulfur content.
A known sulfur compound such as DBT and/or DBTS is dissolved in this reference fuel. The concentration of dissolved sulfur is adjusted to be in the range of expected sulfur content in straight run gas oils or hydrotreated gas oil**.** The characteristics of the reference diesel fuel are shown in Table (2).

Table 2. Characteristics of diesel fuel

Physical property	Diesel fuel	Method
Density@15°C,Kg/L	0.7906	ASTM D 4252
Specific gravity@60/60F	0.7910	ASTM D 1298
^{0}API	47.39	ASTM D 1298
Kinematic viscosity@50^{0}C,cst	2.12	ASTM D 445
Distillation initial boiling point,°C	187	ASTM D 86
10% by volume distilled, °C	214	
20% by volume distilled, °C	225	
30% by volume distilled, °C	235	
40% by volume distilled, °C	249	
50% by volume distilled, °C	250	
60% by volume distilled, °C	255	
70% by volume distilled, °C	259	
80% by volume distilled, °C	263	
90% by volume distilled, °C	265	
Final boiling point,°C	280	
Cetane Number	76.4	ASTM D 613
Cetane Index	72.5	
Poly nuclear aromatics (PNA)	2.1%	
Total Aromatics	6.7	ASTM D2549

Sulfur measurement:
Equipment: The HORIBA Model SLFA-2100Sulfur-in-oil analyzer uses the energy-dispersive X-ray fluorescence spectroscopy method for the accurate and rapid analysis of the sulfur content of petroleum products, including fuel oil and diesel fuel. It measures a range from 0 wt % to 5 wt %, amounts of sample from 4-10cm^3, amount of sample. Figure. (1) shows the HORIBA Model SLFA-2100 used in the current research.



Figure 1. Horiba Model Slfa-2100H Sulfur-in-oil analyzer Sample cell**:**

The sample cell used for the SLFA analyzer has been specially developed for the accurate measurement of the sulfur content in fuel oil by the energy dispersive X-ray fluorescence spectroscopy method. A major part of the sample cell is made of plastic. It consists of the following parts; disposable cell, inner and outer frame of cell and cell window.
The procedure of preparing the sample cells is followed from the manual operation. The SLFA series are manufactured so that the error will be 0.03 wt % S maximum when a sample of 1 wt% S is measured.
Calibration of equipment:
The calibration of the setup is necessary to measure the sulfur of oil fractions. The calibration requires more than one sample of which sulfur concentration is known; this is called a standard sample.
In general, to measure the sulfur content in fuel oil, the following two types of standard samples are to be used.

I. Standard samples prepared by mixing tetralin, decaline and dibutyldisulfide (DBDS).
II. Standard sample for sulfur content in oil, verified by the Japanese petroleum society.

Report the results as the total sulfur content, mass % and state that the results were obtained according to test method ASTM D 4294.
Setup of extraction experiments:
A 250 cm^3 two jacketed flask fitted with a mechanical stirrer and a thermocouple were used to carry out the extraction process. The

temperature is controlled by passing water through the shell surrounding the flask. The experimental equipment used in this study was erected in the laboratories of the Petroleum Research Center (PRC). Figure (2) is a photograph of assembled apparatus used for extraction experiments**.**

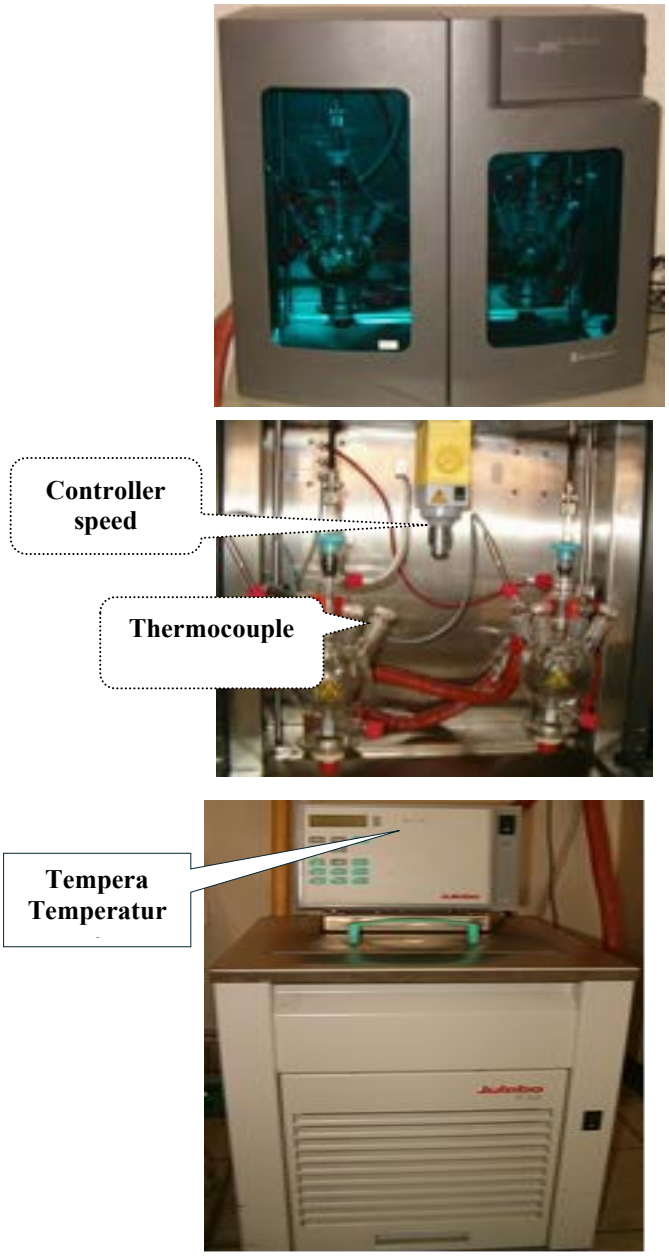


Figure.2. Extraction, setup experiment

Procedure of extraction experiments:
The extraction of sulfur compounds from diesel fuel by different solvents: methanol, acetonitrile, NMP and water at different operating conditions such as concentrations of sulfur in oil, solvent to oil ratio, temperature**,** time and mixing speed. The extraction of sulfur from compound diesel sample has been carried out in the extraction setup described above. The extraction experiment was performed at 25 ^{0}C with all solvents and in addition at 40^{0}C when methanol is used.
Multistage extraction operation was examined with successive six stages using methanol as a solvent.
The phases are then allowed to separate in a separation funnel as in Figure (3) and their volumes are measured, the hydrocarbon phases were washed with distilled water and then analyzed for their sulfur content.

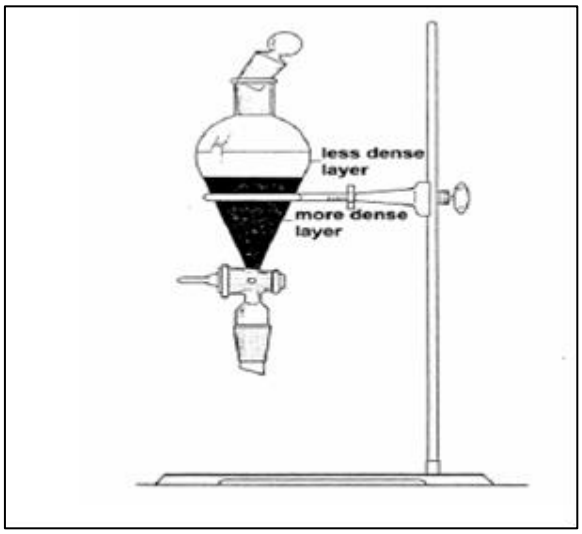


Figure. 3. Separation funnel

Reproducibility:
Reproducibility of extraction:
The reproducibility of the extraction experiments was performed at 25 ^{0}C. In these experiments the solvent to oil ratio were three The results are summarized in Table (3) and Figure. (4).

Table 3. Reproducibility of extraction Initial concentration of 0.17wt%, mixing speed of 300rpm, time=3 hrs

	Yield Vol %	SWt %	Yield Vol%	SWt%	Yield Vol%	Swt%
1	97	0.076	98	0.0570	90	0.03310
2	98	0.076	99	0.0571	90.5	0.03321
3	98	0.075	99	0.0569	90.5	0.03281
4	98	0.077	99	0.0571	90	0.03347

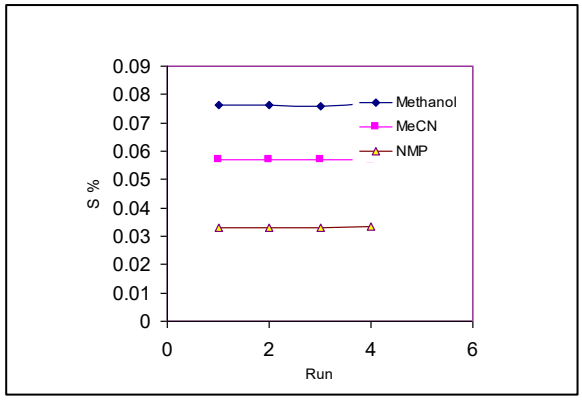


Figure. 4 Extraction experiment reproducibility

3. Results and Discussions

Extraction of DBT with different solvents:

One equilibrium stage and multistage solvent extraction procedure were applied to diesel fuel using three different solvents, namely methanol, acetonitrile and n-methyl-2-Pyrolidone (NMP). Sulfur model compounds dibenzothiophene (DBT) and dibenzothiophene sulfone (DBTS), were added to the sulfur free reference diesel fuel. The later was used in order to simulate oxidized diesel fuel as it is considered the oxidation product. A mixture of DBT and DBTS was tested since DBT in the oxidation procedure not completely removed.

Different parameters were studied in this research. These parameters are solvent to oil ratio, mixing speed, temperature and time. The partition coefficient KP was calculated based on extraction results obtained in this work as follow:

$$KP = \frac{Concentration\ of\ sulfur\ in\ raffinate\ layer}{Concentration\ of\ sulfur\ in\ extract\ layer}$$

The constant KP is termed the distribution or partition coefficient

Extraction of DBT with methanol at 25°C and 40^0C:

Measurements of the sulfur extraction compound DBT from the reference diesel fuel was conducted at temperatures of 25°C and 40°C, mixing speed of 300 rpm and for sulfur initial concentration of 0.17 wt %.

Tests were carried out at two extraction times 3 and 6 hours.

Desulfurization achieved was 60 %, as given in the sulfur content of the raffinate layer, at 25°C and 70 % at 40°C respectively and with oil yield of 90% by volume.

Table 4. Extraction of DBT with methanol at 25°C, mixing speed of 300rpm, initial sulfur concentration of 0.17 wt % for time of 3 hrs

Methanol/ oil ratio	Oil layer		Partition Coefficient (KP)	Methanol layer Sulfur wt %
	Yield vol. %	Sulfur wt %		
1	100	0.1410	1.95	0.072
2	99	0.098	1.5	0.062
3	97	0.076	1.61	0.047
5	90	0.064	1.52	0.042

Table 5. Extraction of DBT with methanol at 25°C, mixing speed of 300rpm, initial sulfur concentration of 0.17 wt % for time of 6 hrs

Methanol /oil ratio	Oil layer		Partition Coefficient (KP)	Methanol layer Sulfur wt %
	Yield Vol. %	Sulfur wt %		
1	99.5	0.135	2.07	0.065
2	99	0.0953	1	0.084
3	93.3	0.070	1	0.07
5	90	0.060	0.96	0.064

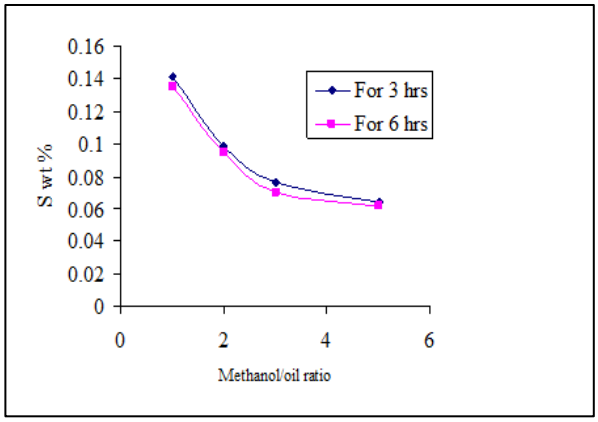


Figure. 5. Effect of extraction time of DBT with methanol at 25°c, mixing speed of 300rpm, initial sulfur concentration of 0.17 wt %

Table 6. Extraction of DBT with methanol at 40°C, mixing speed of 300rpm, initial sulfur concentration of 0.17 wt % for time of 3 hrs

Methanol/ oil ratio	Oil layer		Partition Coefficient (KP)	Methanol layer sulfur wt %
	Yield Vol. %	Sulfur wt %		
1	99.5	0.137	1.87	0.073
2	99	0.092	1.76	0.052
3	93.3	0.067	1.48	0.045
5	90	0.055	1.375	0.040

Table 7. Extraction of DBT with methanol at 40°C, mixing speed of 300rpm, initial sulfur concentration of 0.17 wt % for time of 6 hrs

Methanol/oil ratio	Oil layer		Partition Coefficient (KP)	Methanol layer Sulfur wt %
	Yield Vol. %	Sulfur wt %		
1	99.5	0.133	1.84	0.072
2	99	0.09	1.221	0.061
3	93	0.062	1.55	0.040
5	90	0.051	1.45	0.035

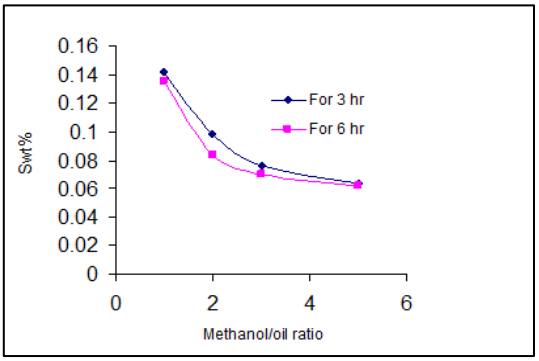


Figure. 6. Effect of extraction time of DBT with methanol at 40°c, mixing speed of 300rpm, initial sulfur concentration of 0.17 wt %

Extraction of DBT with acetonitrile at 25°C: Extraction of DBT with acetonitrile as a solvent at 25°C for extraction times of 3 and 6 hours are given in Tables (8) and (9) respectively.

Table 8. Extraction of DBT with acetonitrile at 25°C, mixing speed of 300rpm, initial sulfur concentration of 0.17 wt % for time of 3 hrs

MeCN/oil ratio	Oil layer		Partition Coefficient (KP)	MeCN Layer Sulfur wt %
	Yield Vol. %	Sulfur Wt %		
1	99.5	0.097	0.97	0.099
2	99	0.068	0.94	0.072
3	98	0.057	0.95	0.06
5	95	0.042	0.85	0.0490

Table 9. Extraction of DBT with acetonitrile at 25°C, mixing speed of 300rpm, initial sulfur concentration of 0.17 wt % for time of 6 hrs

MeCN/ oil ratio	Oil layer		Partition Coefficient (KP)	MeCN Layer Sulfur wt %
	Yield Vol. %	Sulfur Wt %		
1	99.5	0.090	0.93	0.096
2	99	0.066	0.92	0.071
3	98	0.056	0.91	0.061
5	92	0.041	0.87	0.047

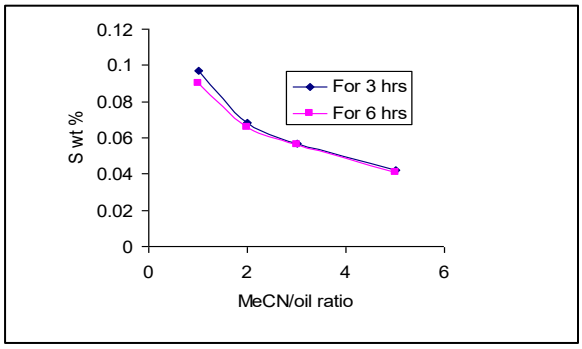


Figure. 7. Effect of extraction time of DBT with acetonitrile at 25°c, mixing speed of 300rpm, initial sulfur concentration of 0.17 wt %

Extraction of DBT with NMP at 25°C:

Extraction of DBT from the reference diesel fuel for times of 3 and 6 hours are shown in Tables (10) and (11) respectively. Deviation of extraction of DBT with NMP at 25°C and 3 hours from that at 25°C and 6 hours are less than 6%

Table 10. Extraction of DBT with NMP at 25°C, mixing speed of 300rpm, initial sulfur concentration of 0.17 wt % for time of 3 hrs

NMP/oil ratio	Oil layer		Partition Coefficient (KP)	NMP layer Sulfur wt %
	Yield Vol. %	Sulfur Wt %		
1	98	0.044	0.66	0.132
2	95	0.037	0.57	0.091
3	90	0.033	0.55	0.058
5	80	0.032	0.69	0.042

Table 11. Extraction of DBT with NMP at 25°C, mixing speed of 300rpm, initial sulfur concentration of 0.17 wt % for time 6 hrs

NMP/oil ratio	Oil layer		Partition Coefficient (KP)	NMP layer Sulfur wt %
	Yield Vol. %	Sulfur Wt %		
1	97	0.043	0.32	0.066
2	95	0.035	0.38	0.064
3	90	0.032	0.4	0.06
5	80	0.030	0.71	0.046

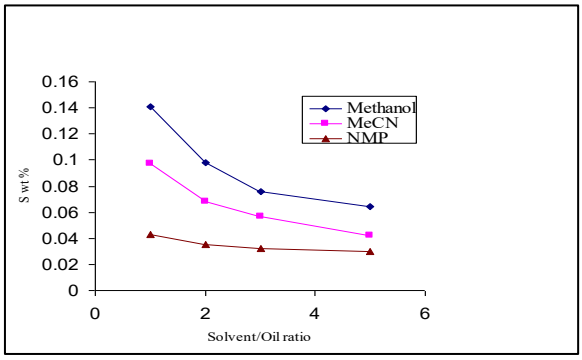


Figure. 8. Effect of extraction time of DBT with NMP at 25°c, mixing speed of 300rpm, initial sulfur concentration of 0.17 wt %

Comparison of various solvents efficiencies in extracting DBT from reference diesel fuel:

Extraction of DBT with the three solvents; namely methanol, acetonitrile and NMP for 3 and 6 hours at 25°C are given in Figures (9) and (10).

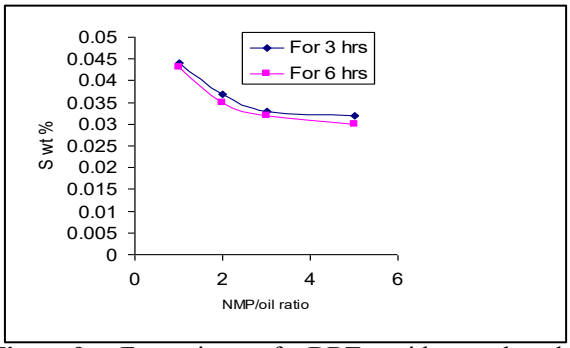


Figure.9. Extraction of DBT with methanol, acetonitrile and NMP at 25°c, mixing speed of 300rpm, initial sulfur concentration of 0.17 wt %, for time of 3 hrs

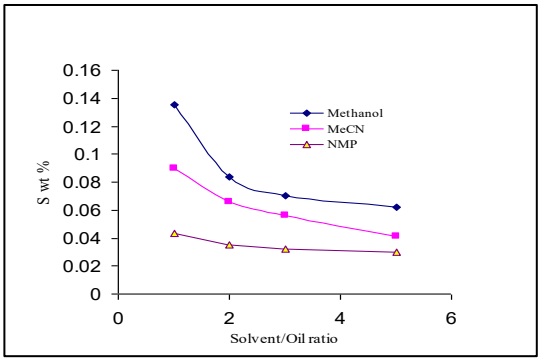


Figure.10. Extraction of DBT with methanol, acetonitrile and NMP at 25°c, mixing speed of 300rpm, initial sulfur concentration of 0.17 wt %, for time of 6 hrs

It can be seen from Figures (9) and (10) that the sulfur content of the raffinate oil layer is substantially reduced. Sulfur removal efficiencies up to 64.7 %, 76 % and 82.2 % when methanol, acetonitrile and NMP are used respectively.

4.Conclusions:

As given in the sulfur (DBT) content of the raffinate layer, desulfurization achieved when methanol is used as a solvent was 60 % at 25 °C and 70 % at 40°C respectively. Oil yield was 90 % by volume for both temperatures.

Comparison of extraction of DBT from the reference diesel fuel using acetonitrile at 3 and 6 hours gave practically similar results with absolute error less than 3 % except for the case of acetonitrile to oil ratio of one it was 7 %.

N- methyl -2- pyrolidone (NMP) is very effective solvent with a removal efficiency approaching 90 % (DBT) compared with the other solvents.

Sulfur removal efficiencies were up to 64.7 %, 76 % and 82.2 % when methanol, acetonitrile and NMP are used respectively. NMP has also been shown as the solvent that give the highest removal efficiency when DBTs and a mixture of DBT and DBTs are extracted with efficiencies of 76 % and 90 % respectively.

Solvent effectiveness factors were 6.5, 9.5 and 4.1 when methanol, acetonitrile and NMP are used respectively with solvent to oil ratio of five for extracting DBT. Based on this, it can be concluded that acetonitrile is the best solvent for extracting DBT from diesel fuels. For extracting DBTs methanol was the most effective, however, when a mixture of DBT and DBTs is extracted from the diesel fuel, acetonitrile was found as the most effective solvent with an effectiveness factor of 12.54 at a solvent to oil ratio of five.

5. Recommendations:

The use of innovative extraction agents such as ionic liquids is suggested.

Measurements of multistage extraction for a mixture of DBT and DBTs with acetonitrile is highly suggested as this solvent was shown to be the most effective and for this mixture which represent a real oxidative desulfurization process.

Extension of the prediction procedure to dibenzothiophene sulfone (DBTS) is recommended and this will require insertion of DBTS characterization data, currently not existing, into simulation packages such HYSYS.

Acknowledgments

My appreciated to Petroleum Research Centre for give us the chance to do many research studies and my thanks also extended to all laboratories at petroleum Research Centre for help us and providing nice sphere.

References

A. Konig, G. Herding, B. Hupfeld, T. Richter and K. Weidmann, Top. Catal., 2002, 16/17, 23.

C. Song, Catal. Today, 2003, 86, 211.
Dong, D.; Jeong, S.; Massoth, F. E. Catal. Today 1997, 37, 267-275.

Girgis, M. J.; Gates, B. C. Ind. Eng. Chem. Res. 1991, 30, 2021-2058.

Gutberlet, L. C.; Bertolacini, R. J. Ind. Eng. Chem. Process Des. Dev. 1983, 22, 246-250.

Howard F. Rase, Hand Book of commercial catalysts, Heterogeneous catalysts, 2000.

Houalla, M., Nag, N. K., Sapre, A. V., Broderick, D. H., and Gates, B. C., AIChE Journal 24, 1015 (1978).

Katzer, J. R.; Sivasubramanian, R. Catal. Rev.-Sci. Eng. 1979, 20, 155-208.

Kabe, T.; Ishihara, A.; Tajima, H. Ind. Eng. Chem. Res. 1992, 31, 1577-1580.

Walid A. Al-Naeem, M. Sc. Thesis, King Fahd University of Petroleum and Minerals, January, 2004.

Comparative Radiological Assessment of a Former Thorium Mine and Oilfield Produced Water Lakes

[1]Ezeddine Hamida , [2]Omar Al-Qadaa and [3]Khalifa Shaklof
[1*]*Petroleum Reseach Center, Tripoli-Libya, e.hamida@prclibya.com*
ORCID No. (Author) : 0009-0008-7333-979X
[2*]Jordan Atomic Energy Commission
[3*]Radiation Measurement and Training Center – Libya

Abstract

The mining and mineral extraction industries release numerous pollutants, including naturally occurring radioactive materials (NORM). In this research, a comparison was made between data from a study published by researchers affiliated with the Ministry of Higher Education of Kazakhstan on the radiation hazards of a former thorium and rare earth elements mining site in northeastern Kazakhstan, and other data on radiation hazards recorded in produced water lakes from oil fields. The Kazakh study analyzed 14 samples, taken from a depth not exceeding 20 cm, while the dried-up oil pits used 7 samples taken from a similar depth, the specific activity concentrations for the Kazakh mining site ranged from 445 to 616 Bq/kg for ^{40}K, 23 to 75 Bq/kg for ^{226}Ra, and 55 to 450 Bq/kg for ^{232}Th, respectively. Whereas the values of these measurements of the oil dry pits ranged between 143 to 7441 for ^{40}K, $1.24x10^3$ to $3.2x10^5$ for ^{226}Ra, and 197 to $1.46x10^5$ for ^{232}Th, Bq/kg respectively. Calculated hazard indicators (radium equivalent activity - Raeq, absorbed dose rate - D, and annual effective dose equivalent - AEDE for the mining site ranged from 141 to 766 Bq/kg, 165 to 332 nGy/h, and 0.08 to 0.41 mSv/y, respectively. For the oil-produced water lakes, these values were significantly higher, ranging from 1.74×10^3 to 5.37×10^5 Bq/kg (Raeq), 783 to 2.37×10^5 nGy/h (D), and 0.96 to 290 mSv/y (AEDE). These data demonstrate that the radiological hazard potential (based on activity concentrations) is significantly higher in the oil-produced water lakes. However, in reality, oil and gas workers typically receive very low occupational doses. In contrast, workers at mining sites, despite the lower activity concentration in the bulk material, often receive considerably higher radiation doses. The reasons for this apparent contradiction—the difference between hazard and actual exposure are explored in detail in this paper.

Keywords: NORM, mining, oil and gas, radiation hazard indicators

مقارنة المخاطر الإشعاعية بين موقع تعدين ثوريوم وبحيرات مياه منتجة نفطية

عزالدين أحميدة ، عمر القضا ، خليفة شقلوف
المؤلف: م. عزالدين -أحميدة مركز بحوث النفط – ليبيا
مساعد مؤلف: م. عمر القضا - مؤسسة الطاقة الذرية الأردنية
مساعد مؤلف : م. خليفة شقلوف - مركز القياسات الإشعاعية و التدريب- ليبيا

الملخص

كل مجالات التعدين و إستخراج المعادن تؤدي إلى استخراج ملوثات عديدة، من بين هذه الملوثات ما يعرف بالمواد المشعة طبيعية المنشأ المعروفة بالنورم، في هذا البحث تمت المقارنة بين بيانات بحث تم نشره من قبل باحثين تابعين لوزارة التعليم العالي لدولة كازاخستان حول المخاطر الإشعاعية لموقع سابق لتعدين الثوريوم والعناصر الأرضية النادرة في شمال شرق كازاخستان و بيانات أخرى لمخاطر إشعاعية مسجلة لبعض بحيرات المياه المنتجة الجافة في حقول نفطية.
كان عدد العينات في البحث الكازاخي 14 عينة أخذت من عمق سطحي لا يتجاوز 20 cm، فيما كان عدد عينات البحيرات النفطية جافة السطح 7 عينات أخذت من عمق مماثل. حيث سجل النشاط الإشعاعي النوعي لكل من البوتاسيوم40 (^{40}K) و الراديوم226 (^{226}Ra)و الثوريوم232 (^{232}Th) لموقع التعدين الكازاخي قيم تراوحت بين 616-445 ، 75-23 ، 450-55 Bq/kg على التوالي ، فيما تراوحت قيم هذه القراءات في البحيرات النفطية بين 7441-143 ،- 1051.24 3.2x 10^{3} x ، 10^{5} 1.46x 197- Bq/kgعلى التوالي. بالنسبة لمؤشرات الخطر و هي النشاط المكافئ للراديوم (Raeq) و الجرعة الممتصة (D) و الجرعة المكافئة السنوية الفعالة (AEDE) فقد تراوحت لموقع التعدين كالأتي: 766-141 Bq/kg، 332-165 nGy/h، 041- nGy/h 783،x10^{5} -1.74x10^{3}Bq/kg 5.37 mSv/y 0.08على التوالي ، فيما تراوحت قراءات البحيرات النفطية كالتالي 2.37x105 - ، 290-0.96 mSv/yعلى التوالي.
تظهر هذه البيانات أن المخاطر الإشعاعية الناتجة عن البحيرات النفطية أكبر بشكل واضح منها لموقع التعدين ، لكن فعليا و واقعيا يتلقى العاملين في قطاع النفط و الغاز في العموم جرعات إشعاعية ضئيلة جدا، في المقابل يتلقى العاملين في التعدين بشكل عام جرعات إشعاعية معتبرة ، هذا التناقض الظاهر يرجع لأسباب عديدة يفصل فيها هذا البحث.

الكلمات المفتاحية: النورم ، التعدين ، النفط والغاز, مؤشرات الخطر الإشعاعي

1. Introduction

The International Atomic Energy Agency's (IAEA) Basic Safety Standards (BSS) categorize "mining and processing of raw materials involving exposure to NORM," including the oil and gas industry, as practices subject to planned exposure situations. Meanwhile, European Union regulations encompass a "list of 16 industrial sectors involving NORM, featuring the oil and gas industry alongside other mining operations chiefly uranium and thorium mining, and rare earth elements which require radiological evaluation" [IOGP, 2016]. Radiological assessments play a pivotal role in understanding and managing environmental and health impacts associated with radioactive materials.

Environmental radioecology pays special attention to the short, medium, and particularly long-term behaviour, distribution, and effects of radioactive contamination across various ecosystems. NORM has become a growing concern, especially within oil and gas operations and the exploration and processing of rare earth elements, which naturally contain significant quantities of radioactive elements like uranium and thorium, necessitating detailed safety and environmental compliance evaluations.

This research contributes to such evaluations by comparing two major economic sectors: the oil and gas industry and thorium/rare-earth mining. Given that the oil and gas sector serves as the backbone of the economy and daily life in many countries, including Libya, evaluating its collateral health and environmental impacts is vital for a comprehensive assessment of its overall economic and social utility. Such comparisons help leverage international experiences regarding NORM side effects across diverse mining industries, despite variations in mining types, methodologies, and byproducts.

Given the relative scarcity of this research topic both locally and internationally, this study serves as a foundation for a broader series of investigations comparing NORM from the oil and gas sector across different oil-producing countries, as well as contrasting it with other extractive industries like uranium, coal, and phosphate mining.

1.1 The Relationship Between the Oil and Gas Industry and NORM:

Like other mineral elements, NORM exists at varying concentrations within oil and gas hydrocarbon reservoirs, making the petroleum sector prone to occupational NORM enrichment. Natural radioactive materials accompany extracted crude oil, eventually depositing onto the internal walls of pipelines, separation vessels, and storage tanks. These accumulations typically manifest as hard mineral scales, while produced water carries suspended sludges containing unprecipitated radioactive isotopes [IOGP, 2016].

1.2 Scale NORM: Sulfate deposits such as barium sulfate ($BaSO_4$) and strontium sulfate ($SrSO_4$) and carbonate deposits (such as calcium carbonate ($CaCO_3$) represent the primary scales encountered in petroleum facilities. Because radium shares chemical similarities with barium, strontium, and calcium, it co-precipitates with them to form radium sulfate, radium carbonate, or

occasionally radium silicates. The mixing of sulfate-rich seawater with brine-heavy formation water heightens precipitation tendencies. Abrupt pressure, temperature, or pH shifts during fluid ascent further drive scale deposition, severely restricting pipeline conveyance capacity [IOGP, 2008].

1.3 Sludge and Residue NORM: Radioactive particles containing radium that fail to integrate into hard scales settle within sludges, sediments, and produced waters. Other radionuclides, such as lead-210 (^{210}Pb) and polonium-210 (^{210}Po), are found in pipeline debris, bottom sludge of storage tanks, oil-gas separators, dehydration vessels, liquefied natural gas (LNG) storage tanks, and waste pits (IOGP, 2008).

1.4 Gas Processing Facility NORM: Radon is a radioactive gas present in varying proportions within natural gas reservoirs. In the absence of natural gas, radon dissolves into light hydrocarbons and aqueous phases. Upon extraction, it predominantly follows the gas stream. During natural gas fractionation, high concentrations of radon may concentrate within propane streams and, to a lesser extent, ethane streams. Radon-222 (^{222}Ra) decays naturally into multiple radioactive progeny (short-lived radon daughters), alongside longer-lived lead-210 (half-life of 22.6 years) and polonium-210 (half-life of 138 days). Most radon decay products (90–99%) attach to ambient aerosols, airborne dust, or interior equipment surfaces such as scrubbers, compressors, reflux pumps, control valves, and production lines, forming thin radioactive films (IOGP, 2008).

1.5 Seawater Injection Systems NORM: Seawater contains uranium at concentrations reaching parts per billion (µg/L). Utilizing seawater for reservoir pressure maintenance can elevate NORM concentrations. In anaerobic environments like geological formations, sulfate-reducing bacteria promote the absorption of precipitated uranium into bio-fouling sediments. While negligible in many injection setups, systems handling massive volumes of seawater can develop bio-fouling uranium concentrations high enough to pose worker hazards and waste disposal challenges, with uranium concentrations reaching up to ~2% by weight (IOGP, 2008).

1.6 Uranium and Thorium Mining:
Thorium and uranium are naturally occurring radioactive elements distributed within the Earth's crust, frequently co-existing in overlapping geological formations. Although structurally similar, they differ significantly in isotopic composition, radioactivity, environmental behaviour, and nuclear applications. Thorium occurs almost exclusively as Thorium-232 (^{232}Th), whereas uranium consists of a mixture of Uranium-238 (^{238}U) and Uranium-235 (^{235}U) [Lide, 2005]. Both elements undergo alpha decay and serve as parents to long radioactive decay chains [Eisenbud & Gesell, 1997], as illustrated in Figures 1.a & 1.b.
The toxicity of thorium stems primarily from radiological hazards via inhalation, whereas uranium presents both radiological and chemical toxicity particularly nephrotoxicity owing to its heavy metal properties. Radionuclides contributing to gross alpha activity include Radium-226 (^{226}Ra),

Uranium-238 (^{238}U), and Radon-222 (^{222}Ra) along with its progeny like Polonium-210 (^{210}Po), which are linked to severe adverse health outcomes. Chronic exposure to radium isotopes increases risks of anemia, cataracts, bone tumors, and dental necrosis. Gastrointestinal absorption of uranium isotopes induces kidney damage. Furthermore, consuming water with elevated radon levels elevates stomach cancer risks. Beta-emitting radionuclides include Potassium-40 (^{40}K) and isotopes belonging to the uranium and thorium decay series, notably Radium-228 (^{228}Ra) and Lead-210 [Kang & von Hippel, 2001]. Alpha and beta decay are frequently accompanied by gamma radiation.

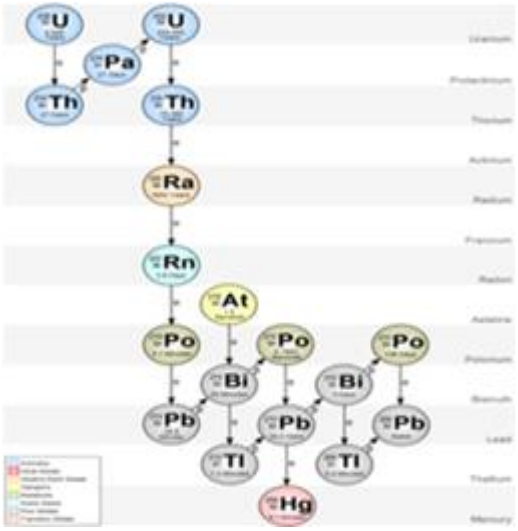


Figure 1.a: Simplified schematic representation of Uranium-238 radioactive decay chain

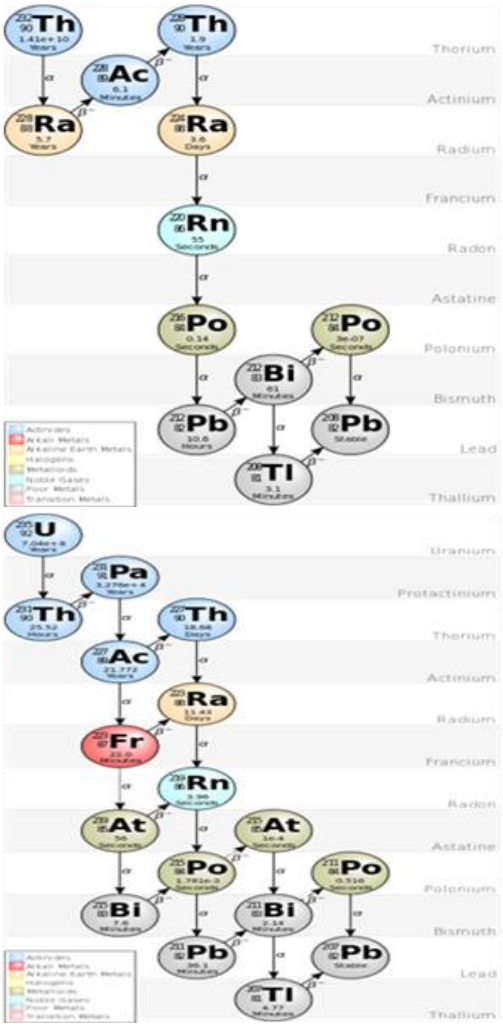


Figure 1.b Simplified schematic representation of Uranium-235, and Thorium-232 radioactive decay chains.

While the radiological inventory across uranium/thorium mining and oil/gas production shares common origins rooted in the natural decay chains of uranium and thorium (with secondary contributions from potassium-40), major differences emerge in:

1. Which isotopes partition into waste streams;
2. Which physical phases (aqueous, solid, or gaseous) dominate;
3. The concentration mechanisms and waste formation pathways; and

4. Hazard patterns and required containment timeframes [IAEA GSR Part 3, 2014].

1.7 Resulting Hazards

From a hazard standpoint, uranium and thorium mining wastes tend to exhibit long-term environmental risk footprints associated with radon release, groundwater and surface water isotope migration, and the persistence of radium and thorium for thousands to tens of thousands of years, mandating extended engineering closures, barriers, and monitoring regimes. Conversely, oil and gas risks are usually localized around specific operational touchpoints (maintenance, scale removal, equipment cleaning, sludge handling) and aqueous release pathways during produced water discharge, with particular emphasis on Radium-226 (^{226}Ra), Radium-228 (^{228}Ra), and radon progeny in gas systems such as Lead-210 (^{210}Pb) and Polonium-210 (^{210}Po) [IAEA, 2021].

1.7.1 Radiological Hazards and Exposure Pathways for Workers, the Public, and the Environment:

Hazards depend on physical state (gas, liquid, solid), radiation type (alpha, beta, gamma), dose pathway (external, internal), and exposure duration. NORM exposure pathways are typically site-specific, depending on proximity to fluid sinks or disposal sites, with external exposure, radon inhalation, and ingestion via water, crops, and animal products playing key roles [UNSCEAR, 2024].

1.7.2 In Uranium Mining and Processing:

1.7.2.a Workers: Critical occupational hazards involve inhaling radon and its progeny in mine environments (especially underground) and dust containing long-lived alpha emitters such as Thorium-230 (^{230}Th), Radium-226 (^{226}Ra), and Polonium-210 (^{210}Po), alongside external gamma radiation originating from radium daughters in mill tailings. The BSS occupational dose limit sets an average effective dose threshold of 20 mSv per year averaged over 5 years, with additional operational constraints [UNSCEAR, 2024].

1.7.1.b Public and Environment: Primary risks relate to radon exhalation from tailings impoundments, potential contaminant migration via ground and surface waters, and the persistence of radium and thorium, rendering engineering containment and hydrological control critical safety elements [UNSCEAR, 2024].

1.7.3 In Oil and Gas Operations:

1.7.3.a Workers: Hazards concentrate during maintenance and cleaning tasks such as scale and sludge removal (external gamma exposure near scales, internal exposure via inhalation of contaminated dust, and potential radon inhalation in gas processing plants). Scales and mineral deposits are documented as the most radiologically significant, while radon decay in gas streams can deposit high concentrations of Polonium-210 (^{210}Po) and Lead-210 (^{210}Pb) inside piping [UNSCEAR, 2024].

1.7.3.b Public and Environment: Aqueous pathways are often paramount near oil and gas installations (particularly during

discharge). Although comprehensive public exposure data are scarce, external gamma dose pathways, particulate/radon inhalation, and ingestion represent the highest potential public exposure routes, with disposal options varying according to contamination levels [UNSCEAR, 2024].

2. Methodology

2.1 Oilfield Samples:

Eight samples were collected from produced water lakes across three adjacent oil fields. These samples were prepared to measure the specific activity concentrations of radionuclides ^{226}Ra, ^{232}Th, and ^{40}K in the laboratory. The samples were sun-dried outdoors for two days to eliminate moisture, then placed in an electric oven at 110 ºC for 24 hours to ensure complete residual moisture removal. Dried samples were ground individually using a blender and sieved through a 2 mm mesh screen. One-kilogram samples were stored in Marinelli beakers and tightly sealed with plastic tape.

The beakers were stored for 30 days to allow Bismuth-214 (^{214}Bi) and Thallium-208 (^{208}Tl) to reach secular equilibrium with Radium-226 (^{226}Ra), Thorium-232 (^{232}Th), and their respective progeny. Plastic containers were further secured with secondary plastic wraps to guarantee containment of Radon-220 (^{220}Rn) and Radon-222 (^{222}Rn). Radiological measurements were performed at the Radiation Measurement and Training Center of the Atomic Energy Commission using a High-Purity Germanium HPGe gamma-ray spectrometer with a 40% relative efficiency connected to a multichannel analyzer (MCA). Background radiation interference was mitigated by housing the HPGe detector inside a passive lead shielding enclosure.

Table 1 presents the basic information for the oil samples.

Table 1- The basic information of the oil samples

Sample ID	Collection Date	Detection Date	Counting Duration(h)
Z1	May 2023	Jul 2023	18
Z2	May 2023	Jul 2023	18
Z3	Jun 2023	Aug 2023	18
Z4	Jun 2023	Aug 2023	18
S1	Aug 2023	Sep 2023	18
H1	Sep 2023	Oct2023	18
H2	Sep 2023	Oct 2023	18

2.2 Kazakh Study Samples

Samples were collected from a residential area in Ust-Kamenogorsk (Kazakhstan), also known as Oskemen, the capital of the East Kazakhstan Region situated at the foothills of the Rudny Altai mountains near the confluence of the Ulba and Irtysh rivers. Today, Oskemen serves as a major center for non-ferrous metal mining (lead, zinc, titanium, magnesium). The Kazakh study aimed to evaluate soil radioactive contamination at a former processing facility for monazite, tin, and radioactive ores. The sampling grid covered 480m^2 across 28 total boreholes, collecting 5 depth-incremental samples per borehole 20cm, 40cm, 60cm, 80cm, and 100cm, totaling 140 samples.

Materials were cleared of debris (plant roots, insects, stones, glass, etc.), sieved through a 5mm mesh, and homogenized. Representative samples of at least 1kg were sealed in labeled polyethylene bags. Samples were dried at a maximum temperature of 40ºC spread on polyethylene film, crushed

with a spatula or pestle to break up large aggregates, sieved through a 1mm mesh, and homogenized. A 300g sub-sample was transferred to a 2dcm^3 beaker, mixed with 5:1 of distilled water (1:5 solid-to-liquid ratio), shaken for 2 hours, incubated for 22 hours at room temperature, and filtered through a 0.45µm membrane filter. One liter of filtrate was evaporated to dryness, ashed in an electric furnace at 350^{o}C for 1 hour (in the presence of ethanol), transferred to a pre-weighed counting cell, dried into a uniform layer, weighed, and subjected to gamma-ray spectrometry.

Gamma-emitting radionuclide activity (^{226}Ra, ^{232}Th, ^{40}K) was quantified using an InSpector 1000 gamma spectrometer Canberra, Smyrna, GA, USA [[Kazakh Study , Idrisheva, Z & others].

It should be noted that the comparison was conducted between the seven oil-contaminated samples and only 14 of the 28 surface soil samples (collected at a depth of 20 cm) from the Kazakh site; this is because the oil-contaminated samples were obtained from the surface layer of oil pools. While results from samples collected at greater depths in the Kazakh study will be mentioned, they are excluded from the comparison due to the difference in sampling depth. Furthermore, the Kazakh study assessed alpha, beta, and gamma radiation doses for all samples, whereas the radiological analysis of the oil-contaminated samples focused solely on gamma radiation doses.

2.3 Radiological Risk Assessment:

2.3.1 Activity Concentration (A): Specific activity concentration A was calculated using Equation 1 [Dovlete & Povinec, 2004]:

$$A = \frac{net\ CPS\ samples}{Eff\ I_\gamma W} \rightarrow (1)$$

Where net CPS samples is the net count rate per second, Eff is the detector efficiency at a given energy, Iγ is the ratio of gamma emission intensity to this energy, and W is the sample weight in kg.

2.3.2 The radium equivalent activity (Raeq): The radium equivalent activity (Raeq) in Bq/kg is a widely used radiological hazard index used to assess the risks associated with materials containing ^{226}Ra, ^{232}Th, and 40K. It is determined based on the assumption that 370 Bq/kg of ^{226}Ra, 260 Bq/kg of ^{232}Th, and 4810 Bq/kg of 40K produce the same dose rate. It is calculated as shown in Equation 2 [UNSCEAR 2000]:

$$Raeq = A_u + (A_{Th} \times 1.43) + (A_K \times 0.077) \rightarrow (2).$$

A_u, A_{Th}, and A_k are the radioactivity values for ^{238}U, ^{232}Th, and ^{40}K, respectively, in Bq/kg.

2.3.3 Absorbed Dose Rate (D): Determining the absorbed dose rates (D) of samples in nGy/hr of specific radioactivity concentrations, where 1 Bq/kg of 40K, 238U, and 232Th, respectively, gives an absorbed dose rate of 0.0417 nGy/hr, 0.462 nGy/hr, and 0.604 nGy/hr, respectively, at 1 meter above the ground surface, as shown in Equation 3 [UNSCEAR 2000]:

$$D = (0.462 \times A_U) + (0.604 \times A_{Th}) + (0.0417 \times A_K) \rightarrow (3)$$

2.3.4 Annual Effective Dose Equivalent (AEDE): The concentration of radionuclides in the environment due to terrestrial gamma radiation from 238U, 232Th, and 40K can be measured using the annual effective dose equivalent (AEDE) [UNSCEAR 2000], where:

$$AEDE = D \times 1.23 \times 10^{-3}\ mSv/y \rightarrow (4),$$

where D is the absorbed dose rate (nGy/h), 1.23×10^{-3} = 8760 hr/yr x 0.2 x 0.7 Sv/Gr
8760 is the number of hours in a year, 0.2 is the percentage of time spent outdoors (or occupancy factor) for an average person, and 0.7 is the percentage of the absorbed dose affecting vital organs in the human body, which depends on several factors such as the type of radiation and the type and sensitivity of the human organ [UNSCEAR 2000].

2.3.5 The gamma radiation level index (Iγ) is used to monitor the average annual dose received from exposure to external gamma radiation emitted from the topsoil. It is calculated using the following formula:

$$I_\gamma = \frac{A_{Ra-226}}{300} + \frac{A_{Th-232}}{200} + \frac{A_{k-40}}{3000} \rightarrow (5)$$

where A_{Ra-226}, A_{Th-232}, and A_{K-40} represent the radioactivity [becquerels/kg] of radium-226, thorium-232, and potassium-40, respectively. If the calculated values are greater than or equal to 1, the soil may be considered contaminated [UNSCEAR 2000].

2.3.6 Increased Lifetime Cancer Risk (ELCR): Based on the expected annual exposure (AEDE), the increased lifetime cancer risk (ELCR) can be calculated. This unitless coefficient is used to estimate the probability of developing cancer in humans during the lifetime of an individual exposed to naturally occurring radioactive materials [Bulubasa, G.; Costinel 2021].

$$ELCR = AEDE \cdot DL \cdot RF \rightarrow (6)$$

DL: Life expectancy (70 years as defined by the World Health Organization in 2014). RF: Risk factor for cancer lethality, 0.057 per sievert for random effects of ionizing radiation, as proposed by the International Commission on Radiological Protection (ICRP). The global average is 0.29×10^{-3} [UNSCEAR 2000].

2.3.7 The Annual Gonadal Dose Equivalent (AGDE): is defined as a measure of the genetic significance of the annual dose received by the reproductive organs of a population or those exposed to radiation in general.

$$AGDE = 3.09\ A_{Ra-226} + 4.18\ A_{Th-232} + 0.314\ A_{K-40} \rightarrow (7),$$

where A_{Ra-226}, A_{Th-232}, and A_{K-40} represent the radioactivity [Bq/kg] of radium-226, thorium-232, and potassium-40, respectively. The global average is 300 μSv/y [UNSCEAR2000].

3. Results and Discussion

3.1 The Comparison: As noted, 14 surface soil samples with peak activity values from the Kazakh study were selected for comparison, representing the highest values among 28 readings. Table 2 contrasts radionuclide activities between oilfield samples and Kazakh samples, while Figures 2,3,4 and 5 illustrate hazard indicator comparisons. A striking disparity appears between specific activity concentrations and hazard indicators, which skew significantly higher for oilfield samples. While unexpected

at first glance, NORM in oilfields concentrates intensely within specific operational touchpoints, prominent among them being oilfield evaporation/produced water lakes. In uranium mining, conversely, massive quantities of mill tailings are produced that retain most original ore radioactivity post-extraction, sustaining long-lived isotopes like ^{230}Th and ^{226}Ra, heavy metals, and acid drainage risks. IAEA guidelines indicate mill tailings retain approximately 75% of original uranium ore radioactivity at concentrations approaching raw ore [Nelson, 2015].

Table 2: Comparison of radioactivity concentrations between oilfield samples and Kazakh samples

Radioactivity of oil samples (Bq/kg)			
Sample Code	^{226}Ra	K^{40}	^{232}Th
Z1	$1.33x10^5$	484.7	512.51
Z2	$7.53x10^4$	-	-
Z3	$9.88x10^3$	532.02	197.09
Z4	$8.71x10^3$	143.4	$9.48x10^3$
S1	$1.24x10^3$	240.5	330.056
H1	$3.21x10^5$	$7.44x10^3$	$1.46x10^5$
H2	$7.64x10^5$	329.3	$6.52X10^3$
Radioactivity of Kazakh samples (Bq/kg)			
Sample Code	^{226}Ra	K^{40}	^{232}Th
1	766	450	332
2	376	430	166
3	471	366	206
4	394	352	173
5	290	383	128
6	470	339	205
7	449	395	197
8	616	381	268
9	468	415	205
10	376	444	166
11	509	440	223
12	482	410	211
13	410	405	180
14	398	415	133

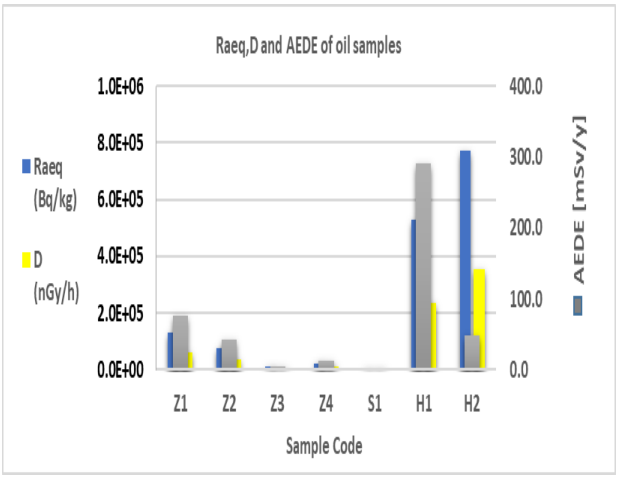


Figure 2 - Radium equivalent activity (Raeq), Absorbed dose rate (D), and Annual effective dose equivalent (AEDE): of oil samples.

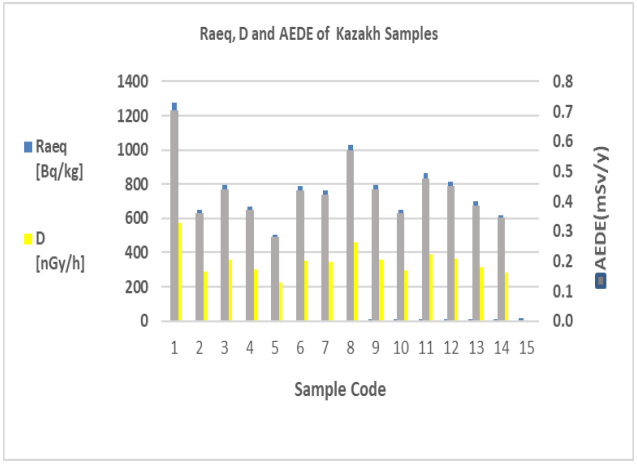


Figure 3- Radium equivalent activity (Raeq), Absorbed dose rate (D), and Annual effective dose equivalent (AEDE): of Kazakh samples

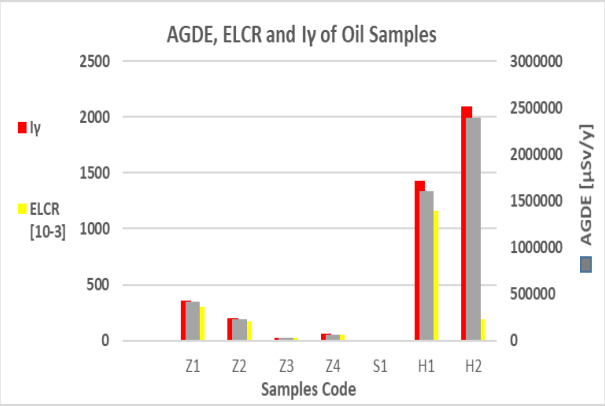


Figure 4- The gamma radiation level index (Iγ), Increased Lifetime Cancer Risk (ELCR) and the Annual Gonadal Dose Equivalent (AGDE) of oil samples

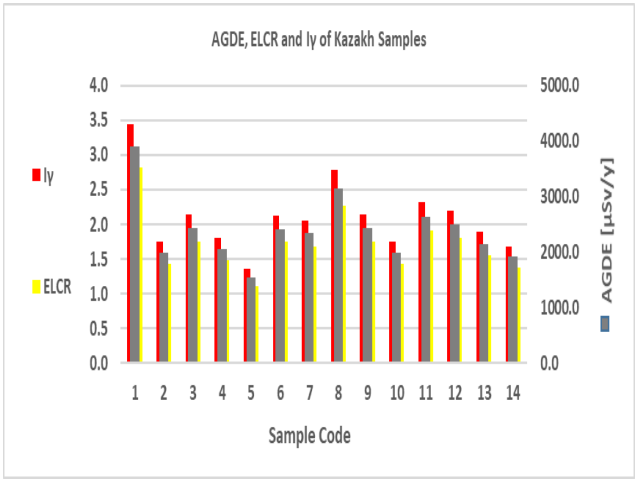


Figure 5- The gamma radiation level index (Iγ), Increased Lifetime Cancer Risk (ELCR) and the Annual Gonadal Dose Equivalent (AGDE) of Kazakh samples

In the oil and gas sector, radioactive waste generally features large volumes of low- to medium-activity produced water juxtaposed against small volumes of scales and sludge exhibiting extremely high activity due to radium co-precipitation with barium and strontium sulfates inside piping and equipment. Scale activities reach 10-100 Bq/g, with sludge potentially reaching hundreds of Bq/g or more [Rowan et al., 2011].

Produced water radioactivity typically ranges around 4Bq/L for ^{226}Ra and 2Bq/L for ^{228}Ra, with potential surges up to 50-fold 200Bq/L depending on fields, salinity, and reservoir geology [Rowan et al., 2011]. Scientific literature reports wide measurement ranges for ^{226}Ra: 0.04-1480Bq/L in produced waters, 1.1-2,015,000Bq/kg in scales, and 10-100Bq/kg in sludge, reflecting basin, operational, and methodological variations [OECD, 1999].



Figure (6) – Instantaneous dose recorded at sampling sites H1 and Z1

3.1.1 Uranium mining: IAEA guidelines confirm that milling residues retain approximately 75% of the original

radioactivity present in the ore, with most chain isotopes remaining at concentrations close to those in the ore—with the exception of the uranium isotopes that are extracted [IAEA 2014 GSR Part 3].
waters influenced by mining activity exhibit dissolved radium levels reaching 8-15Bq/L at specific points, alongside tailings dams and underground drainage [OECD, 1999].

Sample **H1** (Figure 2) recorded a peak instantaneous reading of 33.26 µSv/h, equivalent to 291mSv/y, meaning an individual remaining at that exact spot for a full year would absorb 291mSv. While physically impossible, this is mathematically conceivable. Consequently, oil worker exposure risks are minimal under normal conditions due to the restricted spatial distribution of NORM, low probabilities of encountering such extreme values, and the physical impossibility of prolonged human presence at such spots. Exceptions occur during separator and vessel cleaning, which follow rigorous protocols that decisively minimize exposure; even then, radiation doses rarely reach such extremes. Sample **Z1** registered an instantaneous dose rate of 8.43µSv/h 76mSv/y.

3.2.1Methodological Note: Annual effective dose equivalent values were derived by computing specific activity via Equation 1, determining absorbed dose rate D via Equation 3, and applying Equation 4 to yield AEDE, rather than performing direct conversions from portable instrument instantaneous readings (Figure 2), though both approaches yield consistent trends. This consistency and its underlying nuances are explored in our prior publication [*Atom and Development Bulletin*, Issue 2, 2025, Arab Atomic Energy Commission].

3.2- Knowledge Gaps and Uncertainties:
A shortage of standardized databases tracking radium, lead, and polonium activity by waste stream persists outside the United States, where regular national regulatory reports are available. Many global publications originate from disparate sources utilizing varying measurement methods and detection limits.
Assessments relying solely on Radium-226 measurements may underestimate total activity a phenomenon documented in unconventional gas-derived produced fluids with direct implications for sampling, storage, and analytical protocols.
Comparisons between "radiological risk" and "chemical risk" within identical wastes remain imbalanced: uranium mill tailings contain heavy metals and acid drainage hazards, whereas produced waters feature elevated salinity, heavy metals, and organic compounds that can surpass radiological impacts in certain environmental scenarios. This is highlighted in waste management guidelines addressing radiological and non-radiological facets jointly.
Variations in regulatory frameworks for TENORM in the oil and gas sector across different countries lead to disparities in key management parameters such as designated disposal sites, cleanup thresholds, and measurement requirements [EPA2020]. Based on this information from the US EPA and the data presented in Table 3, it is evident that comparing data from various mining sites worldwide is challenging. For instance, a

granite production site in Shijiazhuang, China, reported an absorbed dose (D) ranging from 57.6 to 280nGy/h and an annual

Table 3 – Comparison of radiation risk indicators with other locations worldwide

Location, Region, Country	Raeq (Bq/kg)	D (nGy/h)	AEDE (mSv/y)
Granite area Xiazhuang, China	121–624	57.6–280	70.7–344
Gold mine. Gauteng, Province, South Africa	76–104 (control soil area) 1668–2812 (tailing)	37.5–49.1 (control) 203.9–1297.3 (tailing)	0.1–1.6
Uranium-rich, Area, Siwalik region, India	ns	52.7–1722	ns
Lomonosovov, diamond deposit, Arkhangelsk, Russia	17–198	9–94	0.01–0.12
Abandoned U Mine, Salamanca, Spain	160–1746 (for soil, for rhizosphere up to 9494)	78–856 (for soil, for rhizosphere up to 4 811)	0.095–1.05 (27.0 for Rhizosphere sample)
Rare earth element mine, Lao Cai, Vietnam	ns	1597–25,057	1.96–30.7
Tin tailing, Perak, Malaysia	0.6–20.9 (soil) 3.2–17.0 (tailing)	1.7–8.9 × 103 (soil) 1.2–7.2 × 103 (tailing)	ns
Pb–Zn deposit, Yunnan, China	78.9–225	36.8–108	0.045–0.133
Former REE processing site, Kazakhstan	141–766 (at 0–20 cm) 127–4064 (at 40–60 cm)	65–332 (at 0–20 cm) 59–1737 (at 40–60 cm)	0.08–0.41 (at 0–20 cm) 0.07–2.13 (at 40–60 cm)
This study	$1.73x10^3$ - $5.37.x10^5$	783.6-$2.37x10^5$	0.96-291
World recommended value	<370	59.0	0.07

Table 4 – Comparison of Annual Gonadal Dose Equivalent with Increased Lifetime Cancer Risk

Location, Region, Country	AGDE (μSv/y)	ELCR × 10^{-3}
Granite area Xiazhuang, China	ns	ns
Gold mine. Gauteng, Province, South Africa	ns	ns
Uranium-rich, Area, Siwalik region, India	0.06–2.14	0.21–7.49
Lomonosovov, diamond deposit, Arkhangelsk, Russia	65–675	0.15–1.62
Abandoned U Mine, Salamanca, Spain	ns	0.38–4.19 (10.6 for rhizosphere sample)
Rare earth element mine, Lao Cai, Vietnam	ns	0.008–0.124
Tin tailing, Perak, Malaysia	ns	1.2–42.0 (soil) 5.9–34.0 (tailing)
Pb–Zn deposit, Yunnan, China	256–770	0.158–0.463
Former REE processing site, Kazakhstan	459–2306 (at 0–20 cm) 421–11,994 (at 40–60 cm)	0.32–1.63 (at 0–20 cm) 0.29–7.39 (at 40–60 cm)
[[Kazakh Study , Idrisheva, Z & others]		
This study	$1.59x10^4$-2.33x106	3.83-1164.8
World recommended value	300	0.290

equivalent dose ranging from 70.7 to 344mSv/y; however, applying the standard calculation method (Equation 4) as used in this study yields results that do not align. This discrepancy does not necessarily imply the data is erroneous; rather, several possibilities exist. For example, the reported absorbed dose could represent either a long-term average or a direct, instantaneous reading. In contrast, Equation 4 was applied consistently in the cases of the diamond mine in the Russian Federation and the Spanish uranium mine. Consequently, a significant degree of uncertainty is inherent in such comparisons.

4- Conclusion

The principal conclusion of this research is that oil and gas extraction and production can generate high radiation dose rates at exceptional focal points within the broader general radiological landscape of oilfields. However, the practical impact of these doses is strictly limited due to the localized nature and restricted spatial distribution of NORM. Conversely, NORM from uranium or thorium mining presents divergent impacts owing to its wide spatial footprint and the multi-stage extraction and production processes involved.

This study focused on comparing primary data, emphasizing strong methodological and computational similarities across all hazard indices. Although extensive literature—particularly from the IAEA, UNSCEAR, and ICRP details NORM associated with various extractive industries, direct empirical comparisons between original site data from mineral extraction and petroleum production remain scarce internationally and absent locally.

5-Recommendations: As noted in the introduction, this study initiates a series of investigations examining differences and similarities between extractive sectors (such as coal and phosphate) versus oil and gas.

Regarding Libya, the primary focus of these comparisons is to establish a conceptual framework for reviewing occupational radiation doses within the oil sector. While general environmental and occupational impacts appear to be well-documented, rigorous scientific research remains essential to validate existing procedures and policies. At the same time, we acknowledge the complexities of conducting research in this sensitive field; this necessitates a cautious approach to ensure that human health and environmental protection remain top priorities, without compromising production prospects and economic operations which must advance in tandem with health, safety, and sound environmental management.

References

IOGP (2016). *Managing Naturally Occurring Radioactive Material (NORM) in the oil and gas industry*. Produced by the NORM Task Force.

IOGP (2008). *Managing Naturally Occurring Radioactive Material (NORM) in the oil and gas industry*.

Lide, D. R. (Ed.) (2005). *CRC Handbook of Chemistry and Physics*, 86th ed. CRC Press, Boca Raton, FL, USA.

Eisenbud, M., & Gesell, T. (1997). *Environmental Radioactivity: From Natural, Industrial, and Military Sources*, 4th ed. Academic Press, Cambridge, MA, USA.

Kang, J., & von Hippel, F. N. (2001). U-232 and the proliferation-resistance of U-233 in spent fuel. *Sci. Glob. Secur.*, 9, 1–32.

IAEA (2014). *Radiation Protection and Safety of Radiation Sources: International Basic Safety Standards (GSR Part 3)*. Vienna.

IAEA (2021). *Management of Residues Containing Naturally Occurring Radioactive Material from Uranium Production and Other Activities*. Specific Safety Guide No. SSG-60.

Norwegian Radiation Protection Authority (2004). *Natural Radioactivity in Produced Water from the Norwegian Oil and Gas Industry in 2003*.

Rowan, E. L., Engle, M. A., Kirby, C. S., & Kraemer, T. F. (2011). *Radium Content of Oil- and Gas-Field Produced Waters in the Northern Appalachian Basin (USA): Summary and Discussion of Data*.

Nelson, A. W. (2015). Understanding the Radioactive Ingrowth and Decay of Naturally Occurring Radioactive Materials in the Environment: An Analysis of Produced Fluids from the Marcellus Shale. DOI: 10.1289/ehp.1408855.

UNSCEAR (2024). *Sources, Effects and Risks of Ionizing Radiation*. Report to the General Assembly with Scientific Annexes.

Dovlete, C., & Povinec, P. P. (2004). *Quantification of uncertainty in gamma spectrometric analysis of environmental samples*, IAEA-TECDOC-1401. Int. At. Energy Agency, Austria.

UNSCEAR (2000). *Source and Effects of Ionising Radiation*. Report to the General Assembly with Scientific Annexes. United Nations, New York, NY, USA.

Bulubasa, G., Costinel, D., Miu, A. F., & Ene, M. R. (2021). Activity concentrations of 238U, 232Th, 226Ra, 137Cs and 40K radionuclides in honey samples from Romania. Lifetime cancer risk estimated. *J. Environ. Radioact.*, 234, 106626.

IAEA (2021). *Management of Radioactive Waste from the Mining and Milling of Ores*. Safety Guide No. SSG-60. Vienna, Austria.

OECD (1999). *Environmental Activities in Uranium Mining and Milling*. A Joint Report

by the OECD Nuclear Energy Agency and the IAEA.

EPA (2020). *Health and Environmental Protection Standards for Uranium and Thorium Mill Tailings* (40 CFR Part 192).

[Kazakh Study] Idrisheva, Z., Ostolska, I., Skwarek, E., Daumova, G., Wiśniewska, M., Toktaganov, T., & Kozhakhmetov, Y. (2024). Evaluation of Long-Term Environmental Impact and Radiological Risks at a Former Thorium and Rare Earth Site in North-Eastern Kazakhstan. *School of Geosciences, D. Serikbayev East Kazakhstan Technical University*.

AI-Driven Cybersecurity Framework for Energy Research Infrastructure and Geoscience Data Systems

[1]*M. Abouawn*
[1]*Petroleum Research Centre- Tripoli, Libya,*
email: m.abouawn@prclibya.com
ORCID No.0009-0007-2736-978X

Abstract

This study aims to design, evaluate, and validate an AI-driven cybersecurity framework tailored specifically for energy research infrastructures and geoscience data systems operating mission-critical scientific workloads. Artificial Intelligence (AI) has become essential to strengthening cybersecurity in national energy research environments that host sensitive geoscience workloads. The proposed framework correlates machine-learning–based anomaly detection with identity, endpoint, and network telemetry to surface early-stage attack signals. The evaluation combines operational metrics from production geoscience servers with internal detection benchmarks derived from Microsoft security platforms in the institutional environment. Production telemetry reports 12 restart cycles per year, zero unplanned technical outages, no security-incident downtime, and 168 annual downtime hours—equating to 98.08% availability. Across controlled detection exercises, the AI layer reduced Mean Time to Detect (MTTD) by approximately 30% relative to the historical triage baseline while improving endpoint-compliance visibility. These results highlight the value of integrating AI analytics with existing controls to harden geoscience data systems and mission-critical research services in national energy institutions.

Keywords - Artificial Intelligence, Anomaly Detection, Cybersecurity, Energy Infrastructure, Geoscience Data Protection.

إطار عمل للأمن السيبراني قائم على الذكاء الاصطناعي لحماية البنى التحتية لأبحاث الطاقة وأنظمة بيانات علوم الأرض

مروة أبوعون
مركز بحوث النفط

الملخص

تهدف هذه الدراسة إلى تصميم وتقييم والتحقق من صحة إطار للأمن السيبراني مدعوم بالذكاء الاصطناعي، ومصمم خصيصاً للبنى التحتية لأبحاث الطاقة وأنظمة بيانات علوم الأرض التي تشغّل أحمالاً علمية حرجة .أصبح الذكاء الاصطناعي عنصراً مهماً في تعزيز الأمن السيبراني في بيئات أبحاث الطاقة الوطنية التي تستضيف أحمالاً حساسة لعلوم الأرض .ويعمل الإطار المقترح على ربط اكتشاف الشذوذ القائم على التعلم الآلي مع بيانات الهوية ونقاط النهاية وحركة الشبكة للكشف المبكر عن مؤشرات الهجمات .ويجمع التقييم بين مقاييس تشغيلية لخوادم علوم الأرض المستخدمة في بيئة الإنتاج ومعايير داخلية للكشف مستمدة من منصات Microsoft الأمنية في البيئة المؤسسية .وتُظهر بيانات التشغيل 12 دورة إعادة تشغيل سنوياً، وعدم وجود أعطال تقنية غير مخططة، وعدم وجود توقف ناتج عن حوادث أمنية، و 168ساعة توقف سنوياً، بما يعادل توافراً قدره .98.08%وفي اختبارات كشف مضبوطة، خفّضت طبقة الذكاء الاصطناعي متوسط زمن اكتشاف الحوادث (MTTD)بنحو 30%مقارنة بخط الأساس للفرز التاريخي، مع تحسين وضوح امتثال نقاط النهاية .وتبرز هذه النتائج قيمة دمج تحليلات الذكاء الاصطناعي مع الضوابط القائمة لتعزيز حماية أنظمة بيانات علوم الأرض وخدمات الأبحاث الحرجة في مؤسسات الطاقة الوطنية.

الكلمات المفتاحية: الذكاء الاصطناعي، اكتشاف الشذوذ، الأمن السيبراني، البنية التحتية للطاقة، حماية بيانات علوم الأرض

1. Iintroductions

The rapid digitalization of the energy sector has significantly increased reliance on high-performance computing (HPC), cloud-based identity services, and interconnected research networks that process large and sensitive scientific datasets. Energy research institutions engaged in petroleum exploration, renewable energy modelling, and subsurface analysis operate specialized geoscience servers for seismic processing, reservoir simulation, and geological computations that support scientific research and strategic decision-making.

Energy research infrastructure represents a critical component of modern scientific and industrial development. As these environments increasingly rely on digital platforms and connected systems, cybersecurity has become an essential requirement to ensure the reliability and integrity of research operations. As digital infrastructures expand across research environments, the organizational attack surface grows accordingly, exposing institutions to cybersecurity risks including unauthorized access, malware intrusion, lateral movement, and data exfiltration. At the same time, the growing adoption of Artificial Intelligence (AI) technologies across the energy sector introduces both new operational opportunities and additional security challenges that must be addressed in order to protect critical digital assets and scientific data platforms (Bishop, 2018).

Traditional cybersecurity monitoring systems have historically relied on rule-based and signature-based detection techniques to identify malicious activity. While these approaches remain effective for detecting known indicators of compromise, they often struggle to identify sophisticated attacks, previously unseen threat patterns, or subtle insider behaviors. In modern research infrastructures, the volume and diversity of security telemetry—including identity authentication logs, endpoint security events, and internal network traffic—continue to grow rapidly. This increasing complexity frequently exceeds the capacity of manual analysis and can significantly increase the Mean Time to Detect (MTTD) security incidents in large-scale research environments.

Artificial Intelligence-assisted security monitoring provides a promising approach for addressing these challenges. Machine learning algorithms can analyze heterogeneous security data sources, identify behavioral anomalies, and detect abnormal activity patterns that may indicate emerging cyber threats. By correlating identity events, endpoint telemetry, and network traffic data, AI-driven cybersecurity systems can enhance early threat detection while reducing the workload of security analysts. These capabilities are particularly important in research environments where large scientific datasets and distributed computing resources require continuous monitoring and protection.

Operational observations from institutional network monitoring further illustrate the complexity of traffic behavior within research infrastructures. Firewall telemetry indicates frequent blocked connection attempts, detectable proxy or VPN usage, and high volumes of traffic within categories such as social networking platforms. These traffic patterns may increase the potential risk of unauthorized

access or covert data movement if not properly monitored. Consequently, advanced security analytics including machine learning-based anomaly detection and user behavior analysis become essential tools for strengthening monitoring capabilities in complex research networks (Liu et al., 2008).

The objective of this study is to propose, evaluate, and validate an AI-driven cybersecurity framework tailored specifically for energy research infrastructures by correlating identity, endpoint, and network telemetry to improve anomaly detection capabilities. Furthermore, this study presents an operational reliability snapshot of geoscience computing servers—including system restarts, downtime events, and infrastructure availability metrics—to establish a baseline for secure research operations, while evaluating observed improvements in detection efficiency, including an approximate 30% reduction in Mean Time to Detect (MTTD) achieved within the research environment.

2. Literature Review

Traditional intrusion detection systems (IDS) have long relied on rule-based and signature-based mechanisms, which remain effective for known threats but struggle to detect low-frequency or previously unseen attacks due to the base-rate fallacy (Axelsson, 2000). Early cybersecurity literature established foundational security principles and access-control models for protecting digital environments (Bishop, 2018), while subsequent advances in machine learning expanded detection capabilities to include automated analysis of complex security telemetry (Aggarwal, 2019). Machine-learning-driven anomaly detection has become widely adopted in modern cybersecurity frameworks. Algorithms such as Isolation Forest have shown strong performance in identifying anomalous behavior in high-dimensional datasets (Liu et al., 2008), whereas supervised models including Random Forest and XGBoost have demonstrated high accuracy in classifying attack patterns (Buczak and Guven, 2016; Chen and Guestrin, 2016). Deep-learning-based intrusion detection approaches have also improved detection of sophisticated threats, particularly in network-centric environments (Javaid et al., 2016; Berman et al., 2019).

Industry and research guidelines emphasize multi-layered monitoring across identity, endpoint, and network channels. NIST SP 800-94 highlights the importance of integrating data from multiple security domains to improve detection fidelity (NIST, 2007), while modern enterprise architectures such as Microsoft Defender and XDR platforms promote identity-centric and endpoint-driven threat visibility (Microsoft Security, 2024). Benchmark datasets such as UNSW-NB15 continue to support the evaluation of machine-learning-based intrusion detection systems (Moustafa and Slay, 2015).

Despite these advancements, existing AI-based cybersecurity frameworks rarely address the unique operational and technical requirements of geoscience computing environments, which combine high-value subsurface datasets, high-performance computing (HPC) workloads, and heterogeneous telemetry sources. Current approaches seldom integrate identity, endpoint, and network data into a unified AI-driven model designed specifically for energy research

infrastructures, leaving a critical gap that this work aims to address.

3. Methodology

3.1 Telemetry Acquisition

Security telemetry was collected over a six-month monitoring period from four primary sources within the research environment:

1. Microsoft Entra ID authentication logs — capturing login failures, off-hours access, and location anomalies.
2. Microsoft Defender for Endpoint/XDR — providing process-creation activity and endpoint security signals.
3. Geoscience server audit logs — reflecting HPC workloads, storage I/O, and dataset access operations.
4. FortiGate firewall logs — representing east-west traffic patterns and outbound communication behaviour.

These sources cover the full attack surface typical of energy and geoscience infrastructures.

3.2 Data Processing and Feature Engineering

Telemetry from all sources was normalized into a unified schema and aggregated into short time windows to stabilize behaviour. Preprocessing steps included timestamp alignment, deduplication, and handling of missing values.

A compact feature set was engineered to capture key security-relevant behaviours:

- Identity-level features: login fail ratio, off-hours authentication, new location login.
- Endpoint-level features: process spawn rate, unsigned binary execution.
- Network-level features: east-west fan-out, outbound egress spikes.
- Server-level features: storage I/O spikes, abnormal dataset access frequency.

These features were selected because they directly reflect common early-stage attack patterns observed in operational environments such as credential misuse and lateral movement.

Table 1. Key Security Features Extracted from Telemetry

Feature Category	Example Indicators	Source
Identity	Login fail rate, off-hours login	Entra ID
Endpoint	Process spawn rate, unsigned binaries	Defender XDR
Network	East-west fan-out, egress spikes	Firewall
Geoscience Servers	I/O volume spikes, unusual dataset access	Server logs

3.3 Hybrid AI-Based Detection Framework

The detection component integrates both unsupervised and supervised machine-learning algorithms to identify unknown threats and classify known attack behaviours.

- Unsupervised anomaly detection: Isolation Forest was used to learn baseline behavior across telemetry streams and flag deviations indicative of potential threats.
- Supervised classification: Models such as Random Forest and XGBoost were applied to detect known attack types based on labeled historical patterns. This hybrid approach improves sensitivity to subtle identity anomalies, lateral movement behaviors, endpoint irregularities, and high-volume geoscience-data access. The final detection output is sent to enterprise SIEM/XDR systems for automated alerting and response as shown in Figure 1.

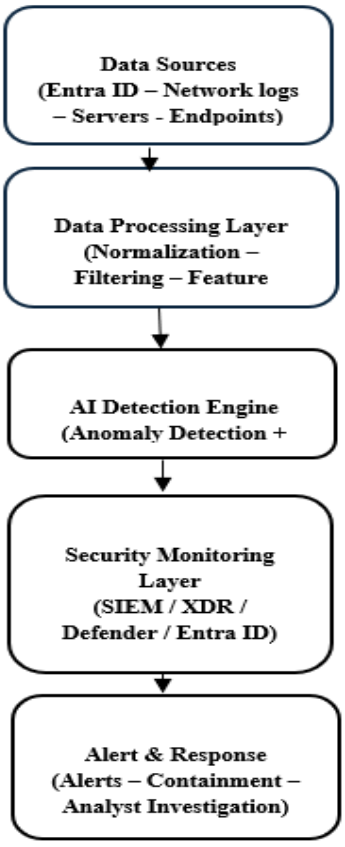


Figure 1 Proposed AI-Driven Cybersecurity Framework Architecture

4. Evaluation Metrics

The effectiveness of the proposed AI-driven cybersecurity framework is evaluated using several standard performance metrics commonly used in intrusion detection and security analytics. These metrics include precision, recall, F1-score, ROC-AUC, alert volume per day, investigation yield, and Mean Time to Detect (MTTD).

To assess system reliability, annual availability is calculated using the following equation:

$$\text{Availability} = \frac{8760 - \text{Downtime(h)}}{8760} \times 100 \quad (1)$$

Availability equation

where 8760 represents the total number of hours in a year and *Downtime(h)* indicates the total system downtime measured in hours.

To evaluate operational improvements introduced by the proposed AI-assisted detection framework, drill-based benchmarking is performed by comparing historical baseline incident triage with the AI-assisted detection pipeline.

The relative improvement in detection time is calculated using:

$$\Delta MTTD = \frac{MTTD_{baseline} - MTTD_{AI}}{MTTD_{baseline}} \times 100\%. \quad (2)$$

ΔMTTD equation

where $MTTD_{baseline}$ represents the average detection time using traditional monitoring methods and $MTTD_{AI}$ represents the detection time achieved by the proposed AI-driven system.

These metrics enable a comprehensive evaluation of both detection accuracy and operational efficiency.

5. Results and Discussion

This section presents the experimental evaluation of the proposed AI-driven cybersecurity framework within an energy research infrastructure environment. The evaluation focuses on detecting security anomalies across three critical layers of the system:

- Identity Security Layer
- Network Security Layer
- Geoscience Data Infrastructure

The results demonstrate how integrating multi-source telemetry and machine-learning models improves threat detection performance across these layers.

5.1 Identity and Access Security Analysis

Identity telemetry from Microsoft Entra ID was evaluated to detect abnormal authentication activity, including excessive login failures, off hours access attempts, and first-time login from unfamiliar locations. These indicators are crucial in detecting credential abuse, compromised accounts, and social engineering-based intrusions.

Table 2. Identity Security Indicators

Feature	Normal Behaviour	Suspicious Behaviour
Login Fail Rate	< 10%	> 20%
Off-Hours Login	Rare	Frequent
New Location Loging	Known location (Tripoli baseline)	Unknown location

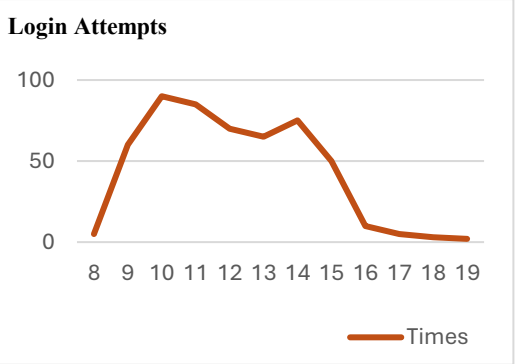


Figure 2: Identity Authentication Anomaly Detection

The results show a clear deviation from normal authentication behaviour, with noticeable spikes in login attempts occurring outside the defined business hours (see Figure 2). These spikes are strongly correlated with failed attempts and unfamiliar IP/location origins, suggesting possible credential-misuse attempts or automated probing. Such deviations, when correlated through the AI detection engine, form high-confidence identity-risk scores.

5.2 Network Traffic Analysis

Network telemetry collected from FortiGate firewalls and endpoint monitoring systems was analysed to detect abnormal network communication patterns.

The analysis focused on:

- internal lateral movement.
- unusual east-west traffic.
- abnormal outbound traffic spikes.

Table 3. Network Traffic Anomaly Indicators

Feature	Description	Source
East-West Fan Out	Number of Internal connections per host	FortiGate
Egress Spike	Abnormal outbound traffic (z-score vs baseline)	FortiGate
Connection Burst	Sudden increase in network sessions	Defender

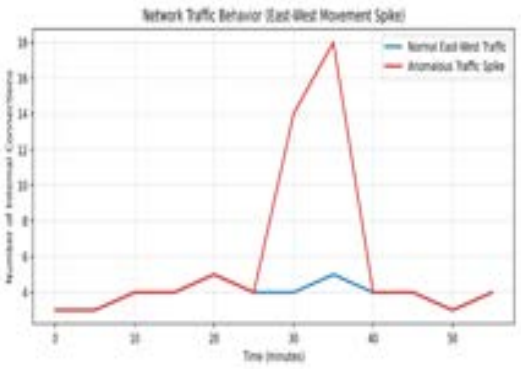


Figure 3 Network traffic behaviour over a 60-minute interval showing normal east-west communication patterns and a pronounced anomalous spike indicative of potential lateral-movement activity.

Figure 3 illustrates a time-series comparison between normal east-west internal communication patterns and an anomalous spike. While normal internal traffic remains stable and low, the anomalous pattern shows a sudden increase in internal destination connections within a short time window. Such behaviour is commonly associated with lateral-movement attempts, where an attacker probes multiple internal hosts to expand access after an initial compromise.

5.3 Geoscience Data Access Monitoring

Geoscience servers host critical and high-value subsurface datasets. Unauthorized access or abnormal query behaviours pose significant risks. The proposed framework monitored access logs and I/O operations to identify suspicious spikes in dataset usage.

Table 4 Geoscience Data Access Indicators

Feature	Description	Detection Purpose
Volume I/O Spike	Sudden increase in storage read/write operations	Detect abnormal extraction
Dataset Access Rate	Number of dataset queries per window	Identify bulk extraction
Off-Hours Data Access	Access attempts outside working hours	Detect malicious or automated access

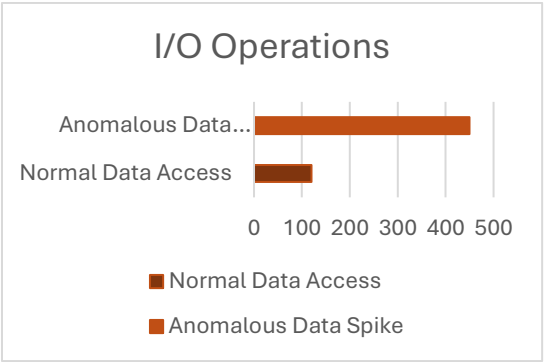


Figure.4 Geoscience storage access behaviour showing normal I/O activity compared with an anomalous high volume spike indicative of potential unauthorized data extraction.

The anomalous bar indicates a significant increase in geoscience data I/O operations compared to typical usage patterns as shown in Figure 4. Such spikes may be associated with unauthorized extraction attempts or automated bulk access to subsurface datasets. When aligned with identity anomalies and off-hours access, these indicators strengthen the likelihood of data-exfiltration behaviour targeting research datasets

5.4 Detection Performance Evaluation

To assess detection efficiency, Mean Time to Detect (MTTD) was compared between traditional signature-based monitoring and

the proposed AI-assisted framework. Controlled drill-based scenarios were executed to measure baseline vs. enhanced detection latency.

Table 5 Mean Time to Detect (MTTD) Comparison

Scenario	Baseline MTTD	AI-Assisted MTTD	Δ Improvement
Credential Abuse	35 min	24 min	31.43% ↓
Lateral Movement	52 min	36 min	30.77% ↓
Data Exfiltration	68 min	47 min	30.88% ↓

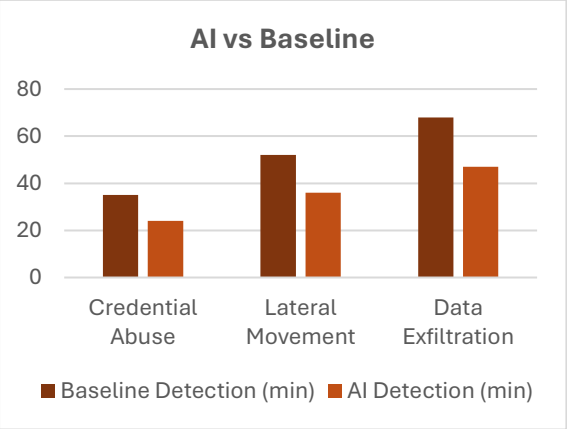


Figure 5. Comparison of baseline detection time and AI-assisted detection time across three simulated threat scenarios, showing ~30% reduction in MTTD

The bar chart illustrates a consistent reduction in detection time across all three simulated threat scenarios when using the AI-assisted framework. The improved MTTD (≈30–31% decrease) demonstrates the effectiveness of correlating identity, endpoint, and network telemetry to surface early-stage attack indicators that traditional monitoring may overlook.

6. Conclusions and Future Work

This paper presented an AI-driven cybersecurity framework tailored for energy research infrastructures and geoscience server environments. The framework integrates multi-source telemetry, feature engineering, hybrid machine-learning detection models, and centralized monitoring and response mechanisms.

6.1 Conclusions

1. The framework improves threat detection accuracy across identity, network, and geoscience layers.
2. Mean Time to Detect (MTTD) incidents is significantly reduced compared to traditional monitoring.
3. Multi-layer correlation reduces false positives and enables faster analyst response.
4. The framework can detect both known attack patterns (via supervised model) and novel anomalies (via unsupervised model).

6.2 Future Work:

- Incorporate deep learning and graph-based threat detection for more complex behaviours.
- Extend real-time monitoring for streaming telemetry analytics.
- Test the framework in larger energy and geoscience datasets, including simulated attack campaigns.
- Integrate with predictive analytics to forecast potential threats before they occur.

References

Aggarwal, C. C. (2019). Machine Learning for Cybersecurity. *Springer*, New York, 495p.

Axelsson, S. (2000). The Base-Rate Fallacy and Its Implications for Intrusion Detection. *ACM Transactions on Information and System Security*, 3: 186–205.

Axelsson, S. (2020). Intrusion Detection Systems: A Survey and Taxonomy. *IEEE Network*, 34: 130–136.

Berman, D.; Buczak, A.; Chavis, J. and Corbett, C. (2019). A Survey of Deep Learning Methods for Cyber Security. *Information*, 10: 122p.

Bishop, M. (2018). Computer Security: Art and Science. *Addison-Wesley*, Boston, 1344p.

Buczak, S. and Guven, E. (2016). A Survey of Data Mining and Machine Learning Methods for Cyber Security Intrusion Detection. *IEEE Communications Surveys & Tutorials*, 18: 1153–1176.

Chen, T. and Guestrin, C. (2016). XGBoost: A Scalable Tree Boosting System. In: *Proceedings of the 22nd ACM SIGKDD International Conference on Knowledge Discovery and Data Mining*, 785–794.

Javaid, A.; Niyaz, Q.; Sun, W. and Alam, M. (2016). A Deep Learning Approach for Network Intrusion Detection System. In: *Proceedings of the 9th EAI International Conference on Bio-inspired Information and Communications Technologies*, 21–26.

Kim, J.; Shim, Y.; Cho, S. and Lee, K. (2020). Machine Learning-Based Cybersecurity Monitoring in Critical Infrastructures. *IEEE Access*, 8: 11234–11245.

Liu, F. T.; Ting, K. M. and Zhou, Z. H. (2008). Isolation Forest. In: *Proceedings of the 8th IEEE International Conference on Data Mining (ICDM)*, 413–422.

Microsoft Security (2024). Microsoft Defender and XDR Architecture. *Microsoft Security Documentation*, Redmond.

Moustafa, N. and Slay, J. (2015). The UNSW-NB15 Dataset for Network Intrusion Detection Systems. In: *Proceedings of the IEEE Military Communications Conference (MILCOM)*, 1523–1528.

NIST (2007). Guide to Intrusion Detection and Prevention Systems (IDPS). *NIST Special Publication*, 800-94, 127p.

Sommer, R. and Paxson, V. (2010). Outside the Closed World: On Using Machine Learning for Network Intrusion Detection. In: *Proceedings of the IEEE Symposium on Security and Privacy*, 305–316.

Wang, L.; Zhang, Y. and Liu, X. (2022). Artificial Intelligence for Cyber Defense in Industrial Control Systems. *IEEE Transactions on Industrial Informatics*, 18: 6200–6211

Integrating AI and Metaverse Technologies for Big Data Optimization in Renewable Energy

[1] *K.abuzaghia, and* [2] *.E. Abuzghaya*

[1] *Khadija Abuzagia, Elmergib University, Khoms , Libya, khadijabuzgia@gmail.com*
[2] *Eman Mansour. Abuzghaya, Elmergib University, Khoms , Libya*
ORCID ID (Author) 0009-0002-9971-227X

Abstract

The integration of Artificial Intelligence (AI), Big Data analytics, and Metaverse technologies particularly Extended Reality (XR)—presents new opportunities to enhance the operation and planning of renewable energy systems. This paper conducts a structured literature review of peer-reviewed studies (2020–2025) to assess current applications, integration challenges, and potential synergies across these domains. Based on the review, a conceptual framework is proposed that combines AI-driven forecasting, anomaly detection, and dispatch optimization with XR-based digital twins for immersive visualization and scenario analysis. The framework comprises three layers: (1) data acquisition for real-time and historical energy data; (2) AI processing using deep learning models such as LSTM; and (3) immersive interaction through XR environments. Performance was evaluated through simulation and semi-field validation using datasets from NREL, NOAA, and OpenEI. Results showed improvements of 63% in forecasting accuracy, 27% in cost reduction, and 25% in battery efficiency compared to a baseline microgrid. This work advances energy informatics by bridging intelligent control with immersive simulation. It underscores the potential of AI–Metaverse integration to build adaptive, efficient, and user-centric energy systems. The proposed model lays the groundwork for future empirical validation and deployment, while highlighting key challenges in integration complexity, data quality, and cybersecurity.

Keywords—Artificial Intelligence (AI), Renewable Energy, Extended Reality (XR), Digital Twins, Smart Grid.

دمج تقنيات الذكاء الاصطناعي والميتافيرس لتحسين البيانات الضخمة في مجال الطاقة المتجددة

خديجة أبوزقية | إيمان منصور أبوزغية
قسم علوم الحاسب، جامعة المرقب – الخمس، ليبيا

الملخص

يوفر التكامل بين الذكاء الاصطناعي**(AI)** ، وتحليلات البيانات الضخمة، وتقنيات الميتافيرس — لا سيما الواقع الممتد **(XR)** —فرصًا جديدة لتعزيز تشغيل أنظمة الطاقة المتجددة والتخطيط لها. تُقدم هذه الورقة البحثية مراجعة منهجية للدراسات المحكّمة (2020–2025) لتقييم التطبيقات الحالية، وتحديات التكامل، وآفاق التعضيد المتبادل بين هذه المجالات. وبناءً على هذه المراجعة، يُقترح إطار عمل مفاهيمي يجمع بين التنبؤ القائم على الذكاء الاصطناعي، واكتشاف الأنماط الشاذة، وتحسين التوزيع التشغيلي، بالتوازي مع التوائم الرقمية القائمة على الواقع الممتد **(XR)** لتحقيق المحاكاة البصرية التفاعلية وتحليل السيناريوهات.

يتكون إطار العمل المقترح من ثلاث طبقات: (1) طبقة جمع البيانات: للبيانات اللحظية والتاريخية الخاصة بالطاقة.؛ (2) طبقة المعالجة بالذكاء الاصطناعي: باستخدام نماذج التعلم العميق مثل شبكات**.(LSTM)** ؛ (3) طبقة التفاعل التفاعلي: من خلال بيئات الواقع الممتد**.(XR)**

تم تقييم الأداء من خلال المحاكاة والتحقق شبه الميداني باستخدام مجموعات بيانات من **(NREL)** و **(NOAA)**و **.(OpenEI)** وأظهرت النتائج تحسنًا بنسبة 63% في دقة التنبؤ، وانخفاضًا بنسبة 27% في التكاليف، وزيادة بنسبة 25% في كفاءة البطاريات مقارنة بالشبكات الصغيرة المرجعية.

يُسهم هذا العمل في تطوير معلوماتية الطاقة من خلال الربط بين التحكم الذكي والمحاكاة التفاعلية، كما يسلط الضوء على إمكانات التكامل بين الذكاء الاصطناعي والميتافيرس لبناء أنظمة طاقة متكيفة، وكفؤة، ومحورية حول المستخدم. يضع النموذج المقترح اللبنة الأساسية للتحقق الميداني والتدشين المستقبلي، مع إبراز التحديات الرئيسية المتعلقة بتعقيد التكامل، وجودة البيانات، والأمن السيبراني.

الكلمات المفتاحية: الذكاء الاصطناعي**(AI)** ، الطاقة المتجددة، الواقع الممتد**(XR)** ، التوائم الرقمية، الشبكة الذكية

1. Introduction

The ongoing digital transformation of the energy sector has accelerated the adoption of advanced technologies such as Artificial Intelligence (AI), Big Data analytics, and immersive platforms. AI has demonstrated robust capabilities in demand forecasting, grid optimization, and predictive maintenance, contributing significantly to renewable energy efficiency, A. K. Mishra and R. Shukla(2024), S. Aslam, Z. Khan, and I. Khan(2021). In parallel, the Metaverse—an immersive virtual environment based on Extended Reality (XR)—offers new avenues for simulation, design, and optimization through digital twins and real-time interaction, P. Bianchi and G. Forte(2024), M. A. Khan and N. Javaid(2020).

However, the joint application of AI and Metaverse technologies in renewable energy is still significantly underexplored. Existing studies often treat these technologies in isolation, overlooking their combined potential. This paper addresses this gap by proposing an integrated framework that leverages AI-driven analytics and immersive simulations to enhance energy system performance, reduce operational costs, and support sustainability goals, Y. Liu, M. Zhang, and Q. Chen(2025), F. García-López, L. A. Hernández, and J. M. Molina(2025).

This study employs a structured literature review (2020–2025) to:

1. Evaluate current AI and Metaverse applications in the energy domain;
2. Identify integration challenges and opportunities;
3. Present a conceptual model for future smart energy systems.

1.1 Literature Review

Recent research has increasingly explored the role of AI in renewable energy systems, applying both machine learning and deep learning for forecasting, load management, and fault detection A. K. Mishra and R. Shukla(2024), S. Aslam, Z. Khan, and I. Khan(2021). AI models have demonstrated notable improvements in solar and wind prediction, thereby enhancing energy dispatch efficiency. Big data analytics plays a pivotal role in smart grids by enabling real-time insights from sensor-generated data. Studies indicate that integrating AI with big data improves system autonomy and performance under variable operating conditions, P. Bianchi and G. Forte(2024), M. A. Khan and N. Javaid(2020).

Meanwhile, Metaverse technologies particularly digital twins and XR are emerging as powerful tools for simulating energy systems within immersive environments. These technologies support pre-deployment testing, rapid scenario evaluation, and operator training Y. Liu, M. Zhang, and Q. Chen(2025), F. García-López, L. A. Hernández, and J. M. Molina(2025).

While some recent studies have begun to examine the integration of AI within XR-based platforms for optimizing microgrid performance D. Martins and H. Lu(2025), N. Zhao, K. Tang, and S. Wu(2025), the majority of existing literature still lacks unified frameworks that combine these technologies to enhance energy system intelligence and long-term sustainability.

2.Methodology

2.1 Scope and Objectives

This research focuses on integrating AI, Metaverse, and Big Data analytics within renewable energy systems specifically in forecasting, smart grid control, and immersive

simulations. A key contribution is the proposal of an original conceptual framework for AI–Metaverse synergy.

2.2. Data Sources and Selection

Relevant literature was sourced from IEEE Xplore, Elsevier, Springer, Scopus, and Web of Science (2020–2025) using keywords such as "AI in energy," "Metaverse simulation," and "digital twin energy systems.

2.3. Thematic Synthesis

Thematic coding was applied to extract recurring challenges, technological innovations, and integration models. Focus was given to synergy strategies between immersive XR platforms and AI-based analytics.

2.4. Conceptual Framework

Based on the reviewed literature, a theoretical model is proposed integrating AI's predictive power with immersive visualization from the Metaverse to enhance energy system intelligence and operational planning.

2.5. Scholarly Contribution

- Originality: Addresses a novel intersection between AI and Metaverse in energy systems.
- Theoretical Impact: Provides a conceptual model to guide empirical and applied studies.
- Academic Value: Bridges research domains of energy informatics, XR systems, and sustainable technologies.

3. Proposed Conceptual Framework and Experimental Validation

3.1. Framework Architecture

The proposed integration model is structured into three functional layers as shown in figure 1:

1. Data Acquisition Layer – Responsible for collecting real-time and historical data from distributed renewable energy assets S. Aslam, Z. Khan, and I. Khan(2021).
2. AI Processing Layer – Utilizes deep learning models (e.g., LSTM) for forecasting, anomaly detection, and generating dispatch recommendations A. K. Mishra and R. Shukla(2024), and P. Bianchi and G. Forte(2024).
3. Immersive Interaction Layer – Employs XR tools such as Unity 3D to render digital twins for visualization and scenario-based simulation F. García-López;etal(2025),and D. Martins and H. Lu(2025).

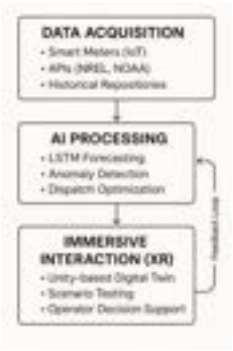


Figure 1: AI–XR framework architecture for renewable energy optimization.

A dynamic feedback loop allows for continuous refinement of AI models and

real-time immersive interaction, enabling adaptive control strategies.

3.2. Experimental Simulation

To evaluate the framework's performance, two system configurations were tested using open-source datasets from NREL (see table 1 and Figure 1:

- Scenario A: A conventional microgrid without integration of AI or XR technologies.
- Scenario B: An enhanced system integrating AI-driven forecasting and immersive XR-based visualization.

Table 1: Simulation Comparison

Metric	Baseline (A)	AI–Metaverse (B)	Improvement
Forecast Accuracy (RMSE)	0.19	0.07	↑ 63%
Operational Cost	$1350	$980	↓ 27%
Battery Efficiency	68%	85%	↑ 25%
Load Response Time	20 mins	5 mins	↑ 75%

3.3. Strategic Implications

- Deployment of AI-powered digital twins in energy system planning.
- Development of immersive XR-based training environments for operators.
- Standardization of data exchange protocols to ensure interoperability across platforms.

4. Pilot Project: Semi-Field Validation

4.1. Configuration

The semi-field testbed was configured with the following components:
Photovoltaic System: 12 kW solar array
Battery Storage: 20 kWh capacity
Smart Inverters: Integrated for dynamic energy management
Load Profiles: Based on actual residential consumption patterns
Data Sources: Real-time and historical data obtained via NREL, OpenEI, and NOAA APIs

4.2. System Architecture

AI Layer: Implemented using LSTM neural networks in Python with TensorFlow for short-term energy forecasting.
Metaverse Layer: Developed in Unity as a digital twin environment incorporating XR and VR capabilities for real-time visualization and user interaction.

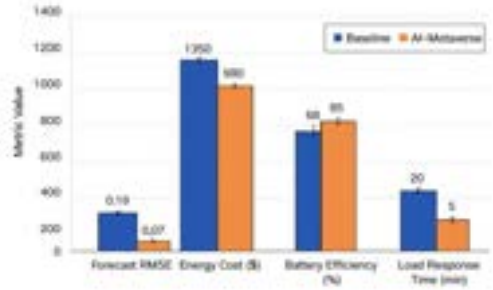


Figure 2: Performance Comparison Between Baseline and AI–Metaverse Systems Across Key Energy Metrics

4.3. Performance Metrics

To evaluate the effectiveness of the proposed AI–Metaverse framework, key performance indicators were measured and compared against a baseline microgrid configuration. These indicators include forecast accuracy (measured by RMSE), energy cost, battery efficiency, load response time, and user experience.
Table 2 presents a comparative summary of both systems. The AI–Metaverse-enhanced system demonstrated substantial

improvements across all technical metrics, including a 62.5% reduction in RMSE and a 27% decrease in energy costs. Additionally, battery efficiency improved by 25.7%, while load response time was reduced by 73%. The user experience score, evaluated qualitatively, reached 8.9 out of 10.

Table 2: Comparative Performance Metrics for Baseline and AI-Metaverse System

Metric	Baseline	AI–Metaverse System	Improvement
RMSE Forecast	0.16	0.06	↑ 62.5%
Energy Cost	$1300	$950	↓ 27%
Battery Efficiency	70%	88%	↑ 25.7%
Load Response Time	15 minutes	4 minutes	↑ 73%
User Experience Score	–	8.9 / 10	–

4.4. Key Findings

The integrated AI–Metaverse framework significantly improved forecasting accuracy and energy cost efficiency.
XR-based tools facilitated enhanced stakeholder engagement and real-time operational decision-making.
The simulation environment supported decentralized control strategies and increased system resilience.

4.5. Limitations

The pilot was conducted in a controlled simulation environment; real-world factors such as network latency, behavioral variability, and device interoperability were not fully modeled.

- Full-scale deployment and real-world validation are recommended for assessing long-term scalability and performance.

5. Economic Analysis

Table 3 presents the monthly financial impact of integrating Artificial Intelligence and Metaverse technologies into renewable energy systems, compared to a traditional baseline configuration.

Table 3: Financial Impact (Per month)

Parameter	Baseline	AI–Metaverse	Impact
Energy Cost	**$1350**	**$980**	**↓ 27%**
Maintenance Cost	**$220**	**$140**	**↓ 36%**
CAPEX Payback	–	**~24 months**	–

The results indicate that the integrated AI–Metaverse approach offers significant long-term financial savings. The return on investment (ROI) is projected to be achieved in under two years, making the proposed solution economically viable for smart grid and microgrid deployments.

6. Discussion and Challenges

The integration of Artificial Intelligence and Metaverse technologies into renewable energy systems present significant opportunities but also introduces several challenges that must be addressed to ensure practical and scalable deployment. The following subsections outline key obstacles identified through the literature review and pilot analysis:

6.1. Integration Complexity

The convergence of AI, Big Data, and XR

platforms demand a robust middleware infrastructure capable of supporting seamless communication across diverse protocols, devices, and data formats. Achieving interoperability remains a technical hurdle, particularly in heterogeneous energy environments.

6.2. Data Availability and Quality

Reliable and high-resolution datasets are essential for accurate AI model training and simulation fidelity. However, many developing regions suffer from fragmented or low-quality data sources, limiting the effectiveness of AI-driven forecasting and control.

6.3. CybersecurityRisks

The increased connectivity and real-time operation of AI Metaverse systems expose critical infrastructure to new cybersecurity threats. Ensuring data integrity, user authentication, and secure communication is vital to safeguard system reliability and stakeholder trust.

6.4. Economic and Infrastructure Barriers

High initial costs associated with XR equipment, AI development, and system integration remain a barrier to widespread adoption. Cost-effective solutions and financial incentives are needed to support implementation, especially for small-scale energy providers.

6.5. Human and Organizational Resistance

Adoption may be hindered by digital illiteracy among users, lack of training, and institutional resistance to emerging technologies. Awareness programs, capacity-building, and policy support can play a role in overcoming these human-centric challenges.

6.6. Validation and Scalability Gaps

Although simulation and semi-field results are promising, real-world deployments remain limited. Further large-scale pilot projects are necessary to validate performance under diverse operational conditions and to inform future standards and best practices.

7. Implementation Tools and Integration Architecture

This section outlines the core technologies and architectural components utilized to implement the proposed AI–Metaverse framework for renewable energy systems.

7.1 Development Tools

The following tools were employed to build and test the system components:

- Unity 3D – Used to develop immersive Extended Reality (XR) environments and digital twins for interactive simulation and visualization.
- Python with TensorFlow/Keras – Applied for developing AI models, specifically deep learning algorithms such as LSTM for forecasting and anomaly detection.
- Jupyter Notebooks and Pandas – Utilized for data preprocessing, exploratory analysis, and performance visualization.

7.2 Integration Architecture

The integration architecture enables real-time communication between AI models and XR-based visual environments through the following components:

- RESTful APIs and WebSockets – Facilitate the transmission of AI-generated outputs to immersive XR interfaces, allowing dynamic interaction and visualization.
- Middleware Layer – Ensures low-latency and synchronized data exchange using lightweight protocols such as JSON and MQTT, supporting responsive system behavior.
- Modular and Scalable Design – The framework is designed to be modular, allowing it to adapt to different microgrid configurations and scale across varied deployment environments.

This architecture supports seamless integration of predictive analytics and immersive simulation, laying the groundwork for adaptive, intelligent, and user-centric energy systems.

8. Ethical and Legal Consideration

The integration of Artificial Intelligence and Metaverse technologies into energy systems raises several critical ethical and legal concerns that must be addressed to ensure responsible deployment:

- Data Privacy: Ensuring compliance with international data protection standards, such as the General Data Protection Regulation (GDPR), is essential to safeguard user information and maintain public trust.
- AI Transparency: The use of non-explainable or "black-box" AI models can hinder user confidence and accountability. Transparent, interpretable AI systems are needed to clarify decision-making processes.
- Digital Inclusion: There is a risk that underserved or digitally marginalized communities may be excluded from benefiting equally from these advanced technologies. Inclusive design and policy measures are necessary to mitigate this gap.
- Liability and Accountability: Legal ambiguity persists regarding who holds responsibility for decisions made by autonomous or semi-autonomous AI systems, especially in critical infrastructure contexts.

To address these challenges, the development of robust governance frameworks is imperative. Such frameworks should promote ethical design, legal clarity, data protection, and equitable access in the deployment of AI–Metaverse-powered energy systems.

9. Benchmarking

To contextualize the proposed framework within existing research, a benchmarking analysis was conducted comparing notable studies that integrate Artificial Intelligence (AI), Extended Reality (XR), or both in the domain of energy systems. The comparison focuses as shown in Table 4 on the inclusion of AI and XR components, the type of validation used, and the application scope.

Table 4: Comparative Benchmarking of Related Studies

Framework	AI	XR	Validation	Scope
Martins & Lu (2025)	✓	✓	Simulation only	Microgrids
Zhao et al. (2025)	✗	✓	Urban model	Urban energy planning
Zhang et al. (2022)	✓	✗	Real testbed	Digital Twin Operations
This Study	✓	✓	Semi-field tested	XR-based Microgrid Operations

This benchmarking highlights the novelty of the current research, which uniquely combines AI and XR in a semi-field validated setup focused on XR-enabled microgrid optimization. It addresses both theoretical and practical gaps by providing empirical evidence of performance improvements in real-world-inspired conditions.

10. Expected Results and Recommendations

10.1 Anticipated Outcomes

- Improved system efficiency, cost reduction, and faster operational responsiveness.
- Enhanced stakeholder engagement through immersive simulations and interactive environments.
- Shortened innovation cycles and fewer design iterations enabled by advanced modeling tools.

10.2. Recommendations

Short-Term (0–1 year):

- Conduct pilot tests to validate feasibility.
- Train technical teams in AI and XR technologies.
- Develop ethical guidelines for responsible use of AI and immersive platforms.
- Initiate stakeholder engagement and awareness campaigns.

Mid-Term (1–3 years):

- Establish standardization protocols for system integration.
- Build immersive XR-based training environments.
- Launch regulatory sandboxes to facilitate testing under controlled legal conditions.

Long-Term (3–5 years):

- Incorporate the proposed framework into national digital and energy strategies.
- Develop comprehensive legal frameworks addressing liability, data protection, and governance.
- Ensure inclusive infrastructure that guarantees equal access across different communities.

11. Conclusions

This research introduced an innovative conceptual and experimental framework that integrates Artificial Intelligence (AI) analytics with immersive Metaverse technologies—particularly Extended Reality (XR)—to optimize renewable energy systems. By combining a structured literature review with simulation and semi-field pilot validation, the study demonstrated measurable improvements in forecasting accuracy, operational efficiency, cost reduction, and stakeholder engagement.

Despite the promising results, real-world implementation still faces several challenges, including technical integration, ethical considerations, and institutional readiness. Nevertheless, the strategic potential of AI–Metaverse convergence to enable adaptive, intelligent, and user-centric energy infrastructures is evident.

To advance this interdisciplinary field, future research should prioritize large-scale empirical validation, establish clear regulatory and ethical frameworks, and develop scalable infrastructure models that support practical deployment in diverse energy environments.

REFERENCES

A. K. Mishra and R. Shukla, "Deep learning-based forecasting models for renewable energy systems," *Renewable Energy*, vol. 221, pp. 154–165, 2024.

A. S. Alsharif et al., "Security frameworks for AI-driven virtual energy environments," IEEE Internet Things J., early access, 2025.

A. Faruqui, D. Key, and E. O'Brien, "Smart grids, AI, and consumer behavior," *The Electricity Journal*, vol. 34, no. 7, p. 106933, 2021.

C. Zhang and B. Wu, "Cloud-edge collaboration for real-time energy analytics," Future Gener. Comput. Syst., vol. 146, pp. 225–239, 2024.

D. Martins and H. Lu, "XR–AI convergence for renewable microgrid control," *Journal of Cleaner Production*, vol. 448, p. 140223, 2025.

D. J. Lee and A. R. Abdelwahed, "Simulated energy markets using metaverse frameworks," Energy Economics, vol. 119, p. 107192, 2025.

E. Aljohani et al., "Metaverse applications for sustainability education," *Journal of Cleaner Production*, vol. 447, p. 139843, 2025.

F. García-López, L. A. Hernández, and J. M. Molina, "Metaverse applications in virtual power system design," *Energy and AI*, vol. 10, p. 100241, 2025.

H. K. Patel and S. Chatterjee, "AI-driven anomaly detection in solar farms," Solar Energy, vol. 240, pp. 301–311, 2022.

J. H. Lee and M. G. Kim, "Ethical implications of AI and XR in energy infrastructure," Technol. Forecast. Soc.

Change, vol. 189, p. 122308, 2023.
J. Zhang et al., "AI-enhanced energy management using digital twins," *Energy Reports*, vol. 8, pp. 399–410, 2022.

K. Ahmed and A. Eisa, "Next-generation smart grid platforms using XR and AI," *Smart Energy*, vol. 6, p. 100048, 2024.

K. N. Kougias and I. V. Antoniadis, "AI-enhanced demand-side management for prosumers," *Energy Strategy Reviews*, vol. 47, p. 101022, 2023.

L. Wang and X. Li, "Towards intelligent digital energy ecosystems," *Nature Energy*, vol. 8, pp. 314–326, 2023.

L. Yu, W. Fan, and H. Liu, "Real-time control in digitalized energy systems," *IEEE Trans. Smart Grid*, vol. 12, no. 4, pp. 3210–3221, 2021.

M. A. Khan and N. Javaid, "Integrating big data and AI for smart grid optimization," *Renew. Sustain. Energy Rev.*, vol. 122, p. 109758, 2020.

M. Bouabdallah and R. Khatoun, "Cybersecurity in AI-integrated smart grids," *IEEE Access*, vol. 9, pp. 118220–118232, 2021.

N. Zhao, K. Tang, and S. Wu, "Urban energy planning in the metaverse: An XR-

based framework," *Sustainable Cities and Society*, vol. 110, p. 105012, 2025.

P. Bianchi and G. Forte, "Big data analytics in hybrid smart grids," *Applied Energy*, vol. 335, p. 121012, 2024.

R. Lin et al., "Hybrid modeling for green energy systems using AI," *Applied Energy*, vol. 331, p. 120285, 2023.
T. Silva and R. Pereira, "Energy simulation in VR/AR environments," *Renew. Sustain. Energy Rev.*, vol. 173, p. 113043, 2024.

Y. Liu, M. Zhang, and Q. Chen, "Digital twins and XR in metaverse-based energy systems," *IEEE Trans. Ind. Inform.*, early access, 2025.

S. Aslam, Z. Khan, and I. Khan, "Applications of AI in renewable energy systems: A systematic review," *Renew. Sustain. Energy Rev.*, vol. 144, p. 111050, 2021.

S. Qasem and Y. Benali, "AI for hydrogen production optimization," *Int. J. Hydrogen Energy*, vol. 50, pp. 19160–19175, 2025.

S. Roy, M. Alam, and A. Mahmud, "Extended reality applications in energy education and management," IEEE Trans. Learn. Technol., early access, 2025.